



energies

Electrified Powertrains for a Sustainable Mobility

Topologies, Design
and Integrated Energy
Management Strategies

Edited by

Laura Tribioli and Manfredi Villani

Printed Edition of the Special Issue Published in *Energies*

**Electrified Powertrains for a
Sustainable Mobility: Topologies,
Design and Integrated Energy
Management Strategies**

Electrified Powertrains for a Sustainable Mobility: Topologies, Design and Integrated Energy Management Strategies

Editors

Laura Tribioli

Manfredi Villani

MDPI • Basel • Beijing • Wuhan • Barcelona • Belgrade • Manchester • Tokyo • Cluj • Tianjin



Editors

Laura Tribioli
Università degli Studi
Niccolo' Cusano
Italy

Manfredi Villani
The Ohio State University
USA

Editorial Office

MDPI
St. Alban-Anlage 66
4052 Basel, Switzerland

This is a reprint of articles from the Special Issue published online in the open access journal *Energies* (ISSN 1996-1073) (available at: https://www.mdpi.com/journal/energies/special_issues/electrified_powertrains_sustainable_mobility).

For citation purposes, cite each article independently as indicated on the article page online and as indicated below:

LastName, A.A.; LastName, B.B.; LastName, C.C. Article Title. *Journal Name* **Year**, *Volume Number*, Page Range.

ISBN 978-3-0365-4125-9 (Hbk)

ISBN 978-3-0365-4126-6 (PDF)

© 2022 by the authors. Articles in this book are Open Access and distributed under the Creative Commons Attribution (CC BY) license, which allows users to download, copy and build upon published articles, as long as the author and publisher are properly credited, which ensures maximum dissemination and a wider impact of our publications.

The book as a whole is distributed by MDPI under the terms and conditions of the Creative Commons license CC BY-NC-ND.

Contents

Laura Tribioli and Manfredi Villani

Electrified Powertrains for a Sustainable Mobility: Topologies, Design and Integrated Energy Management Strategies

Reprinted from: *Energies* **2022**, *15*, 3095, doi:10.3390/en15093095 1

Teresa Donateo and Antonio Ficarella

A Methodology for the Comparative Analysis of Hybrid Electric and All-Electric Power Systems for Urban Air Mobility

Reprinted from: *Energies* **2022**, *15*, 638, doi:10.3390/en15020638 3

Iwona Komorska, Andrzej Puchalski, Andrzej Niewczas, Marcin Ślęzak and Tomasz Szczepański

Adaptive Driving Cycles of EVs for Reducing Energy Consumption

Reprinted from: *Energies* **2021**, *14*, 2592, doi:10.3390/en14092592 27

Simone Lombardi, Manfredi Villani, Daniele Chiappini and Laura Tribioli

Cooling System Energy Consumption Reduction through a Novel All-Electric Powertrain Traction Module and Control Optimization

Reprinted from: *Energies* **2021**, *14*, 33, doi:10.3390/en14010033 45

Qiushi Bi, Guoqiang Wang, Yongpeng Wang, Zongwei Yao and Robert Hall

Digging Trajectory Optimization for Cable Shovel Robotic Excavation Based on a Multi-Objective Genetic Algorithm

Reprinted from: *Energies* **2020**, *13*, 3118, doi:10.3390/en13123118 67

Daniele Beltrami, Paolo Iora, Laura Tribioli and Stefano Uberti

Electrification of Compact Off-Highway Vehicles—Overview of the Current State of the Art and Trends

Reprinted from: *Energies* **2021**, *14*, 5565, doi:10.3390/en14175565 89

Editorial

Electrified Powertrains for a Sustainable Mobility: Topologies, Design and Integrated Energy Management Strategies

Laura Tribioli ^{1,*} and Manfredi Villani ²

¹ Department of Industrial Engineering, University of Rome Niccolò Cusano, Via Don Carlo Gnocchi, 3, 00166 Rome, Italy

² Center for Automotive Research, The Ohio State University, Columbus, OH 43212, USA; villani.5@osu.edu

* Correspondence: laura.tribioli@unicusano.it

The Special Issue “Electrified Powertrains for a Sustainable Mobility: Topologies, Design and Integrated Energy Management Strategies” has been proposed with the main objective of contributing to the sustainable mobility agenda through enhanced scientific and multi-disciplinary topics, aimed at addressing concerns and real possibilities in the achievement of a greener mobility. It was therefore conceived to provide an interesting overview on new needs and investigation topics required for future developments.

In total, five articles, of which four research papers, and one review, have been submitted to the Special Issue covering a wide variety of topics within the proposed subject.

T. Donateo and A. Ficarella [1] have addressed the topic of urban air mobility with particular reference to air-taxi service. They propose a methodology for the design and energy analysis of conventional, hybrid-electric, and full-electric power systems for such application. The novelty of the paper with respect to the state of the art lies in the detailed modeling approach of the powertrains, the evaluation of CO₂ emissions with a well-to-wing approach as a function of the electricity emission intensity factor and the comparison with road vehicles performing the same route in different driving conditions. The results demonstrate the advantages of an all-electric air-taxi with respect to a hybrid electric road taxi.

S. Lombardi et al [2] have tried to tackle the problem of reducing the energy consumption of the cooling circuit for the propulsion system of an all-electric road vehicle through two different approaches: optimization of the control strategy and improvement of the powertrain efficiency. In the first approach, a control strategy to reduce the auxiliary loads of the fan and the pump has been developed and compared with the conventional approach, where the pump and the fan are controlled with a thermostat, while in the second approach a single-motor powertrain has been replaced by smaller traction modules whose powers sum up to the total power of the original powertrain. The study has shown that increasing the powertrain efficiency leads up to a 54% reduction of energy consumption (but only if the cooling circuit is stressed enough and the fan is activated during the vehicle operation). While the optimization of the control strategy can lead up to a 27% energy consumption reduction if normally the cooling circuit is capable of lowering the coolant temperature without the intervention of the fan.

I. Komorska et al. [3] have proposed an algorithm which, by means of the segmentation and iterative synthesis procedures of Markov chains, returns an adaptive energy-efficient driving cycle for a road vehicle under a given route. Moreover, a Gaussian process regression is employed to monitor energy consumption during driving, so as to correct adaptively speed and acceleration in order to maintain the planned energy consumption. An autopilot driving cycle was verified in the study, and results showed that the energy consumption was reduced by approximately 15%, at the cost of increasing travel time by approximately 10%.

Q. Bi et al. [4] worked on a similar topic, but applied to cable shovels for robotic excavation. In particular, a two-phase multi-objective genetic algorithm was established for optimal digging trajectory planning for achieving effective and energy-saving operation.

Citation: Tribioli, L.; Villani, M. Electrified Powertrains for a Sustainable Mobility: Topologies, Design and Integrated Energy Management Strategies. *Energies* **2022**, *15*, 3095. <https://doi.org/10.3390/en15093095>

Received: 13 April 2022

Accepted: 19 April 2022

Published: 23 April 2022

Publisher’s Note: MDPI stays neutral with regard to jurisdictional claims in published maps and institutional affiliations.



Copyright: © 2022 by the authors. Licensee MDPI, Basel, Switzerland. This article is an open access article distributed under the terms and conditions of the Creative Commons Attribution (CC BY) license (<https://creativecommons.org/licenses/by/4.0/>).

The results of the optimization under different digging conditions indicated that the digging time could be decreased from an average of 20 s to 10 s, and the energy consumption per payload could be reduced by 13.28%.

Finally, D. Beltrami et al. [5] have proposed a detailed overview on the state of the art and future trends in the electrification of compact off-highway vehicles, which can be an excellent application for boosting the electrification process, mainly because they are usually more suited for zero-emission tasks, while development costs can be more easily minimized. The paper has allowed for the highlighting of the key differences between on-highway and off-highway vehicles and provides a comprehensive summary of information on the multiple solutions investigated by researchers and currently implemented by manufacturers.

Even if the theme of sustainable mobility is very wide and still entails a lot of work, we believe that this Special Issue can give a small and yet important contribution to stimulate the debate between industry and academic researchers, thanks to the variegated topics of the received articles that cover important aspects related to the full spectrum of sustainable mobility, spanning from air mobility to off-road vehicles.

Funding: This research received no external funding.

Conflicts of Interest: The authors declare no conflict of interest.

References

1. Donato, T.; Ficarella, A. A Methodology for the Comparative Analysis of Hybrid Electric and All-Electric Power Systems for Urban Air Mobility. *Energies* **2022**, *15*, 638. [[CrossRef](#)]
2. Lombardi, S.; Villani, M.; Chiappini, D.; Tribioli, L. Cooling System Energy Consumption Reduction through a Novel All-Electric Powertrain Traction Module and Control Optimization. *Energies* **2021**, *14*, 33. [[CrossRef](#)]
3. Komorska, I.; Puchalski, A.; Niewczas, A.; Ślęzak, M.; Szczepański, T. Adaptive Driving Cycles of EVs for Reducing Energy Consumption. *Energies* **2021**, *14*, 2592. [[CrossRef](#)]
4. Bi, Q.; Wang, G.; Wang, Y.; Yao, Z.; Hall, R. Digging Trajectory Optimization for Cable Shovel Robotic Excavation Based on a Multi-Objective Genetic Algorithm. *Energies* **2020**, *13*, 3118. [[CrossRef](#)]
5. Beltrami, D.; Iora, P.; Tribioli, L.; Uberti, S. Electrification of Compact Off-Highway Vehicles—Overview of the Current State of the Art and Trends. *Energies* **2021**, *14*, 5565. [[CrossRef](#)]

Article

A Methodology for the Comparative Analysis of Hybrid Electric and All-Electric Power Systems for Urban Air Mobility

Teresa Donateo * and Antonio Ficarella

Department of Engineering for Innovation, The University of Salento, via per Monteroni, 73100 Lecce, Italy; antonio.ficarella@unisalento.it

* Correspondence: teresa.donateo@unisalento.it

Abstract: The present investigation addresses the topic of Urban Air Mobility with particular reference to the air-taxi service with electrified power systems. A new and detailed methodology is proposed for the simplified design and energy analysis of conventional, hybrid-electric, and full-electric power systems for this application. The original contributions to the scientific literature on UAM are the detailed modeling approach, the evaluation of CO₂ emissions with a Well-to-Wing approach as a function of the electricity Emission Intensity factor, and the comparison with road vehicles performing the same route in different driving conditions. The comparison demonstrates the advantages of a full electric air-taxi with today's technology versus a hybrid-electric road taxi, especially in cases involving low emission intensity and unfavorable driving conditions (congested traffic, aggressive driving style, and high circuitry factor values). In the case of 2035 technology, the comparison with a referenced fully electric road vehicle is detrimental to the air taxi but the values of Well-to-Wheel/Wing CO₂ with the expected Emission Intensity of 90 g/kWe for the European Union are still quite low (67 g/km). The investigation also quantifies the negative effect of battery aging on the consumption of the air taxi and on the number of consecutive flights that can be performed without fully charging the battery.

Keywords: urban air mobility; WTW emissions; hybrid electric vehicles; battery aging

Citation: Donateo, T.; Ficarella, A. A Methodology for the Comparative Analysis of Hybrid Electric and All-Electric Power Systems for Urban Air Mobility. *Energies* **2022**, *15*, 638. <https://doi.org/10.3390/en15020638>

Academic Editors: Laura Tribioli, Manfredi Villani and Tek Tjing Lie

Received: 10 December 2021

Accepted: 13 January 2022

Published: 17 January 2022

Publisher's Note: MDPI stays neutral with regard to jurisdictional claims in published maps and institutional affiliations.



Copyright: © 2022 by the authors. Licensee MDPI, Basel, Switzerland. This article is an open access article distributed under the terms and conditions of the Creative Commons Attribution (CC BY) license (<https://creativecommons.org/licenses/by/4.0/>).

1. Introduction

According to Angel et al. [1], the number of people living in cities keeps growing and is expected to double from 2011 to 2054. This increase in the mobility requirement is leading to the need for faster, cheaper, safer, and cleaner forms of transportation [2], not only to avoid the depletion of fossil energy sources but above all to preserve the environment. Transportation accounts for around one-fifth of today's global carbon dioxide (CO₂) emissions [3]. Road travel accounts for three-quarters of them, while the contribution of aviation to transport-associated emissions is 11.6%. Increasing the efficiency of the utilization of energy in transport systems, speeding up the deployment of sustainable energy sources, and enhancing zero-emission vehicles are the main actions that have been proposed to reduce the environmental impact of transportation [3] and fulfill future mobility requests.

In the last few years, many companies have developed delivery and taxi services conceived to work in the air. These new services are denoted as Urban Air Mobility (UAM) and Urban Air Delivery. This investigation focuses on Urban Air Mobility and, in particular, on the air-taxi service. In this field, several companies have developed electric vertical take-off and landing (eVTOL) aircraft over the past few years. However, there are still many open issues such as the lack of infrastructure, the need to ensure safety (in particular avoiding collisions during the mission), and the development of suitable air-traffic management systems [4–6].

UAM is an appealing application for electric power systems thanks to its short-range and limited speed requirements that make full electric powertrains possible, even with

today's batteries (i.e., despite their moderate values of energy density and power density, which are the major bottlenecks for larger aircraft). For longer distances, hybrid-electric concepts can be considered to provide the necessary range while guaranteeing silent and environmentally friendly transport systems. To ensure the success of electric and hybrid-electric air taxis, an extensive charging infrastructure powered by clean energy sources is needed as well as the availability of a large number of take-off and landing facilities [7]. Moreover, ad hoc flight mechanics analysis tools and design techniques need to be developed to tackle the challenge of sizing and management of hybrid and fully electric aircraft. In fact, the analysis of the energy request of this kind of vehicle and their environmental impact is a hot topic still in need of further research efforts, as proved by the limited works in this topic, such as the recent studies on Urban Air Delivery [8–10] and UAM [11–14].

Uber [11] performed a comparison between a traditional road vehicle and a VTOL one in terms of time spent, distance covered, and costs without considering the environmental impact. As pointed out in [12], the sustainability of air-taxi services is unclear because of the high energy requirement of this kind of vehicle, above all for take-off and climb. A comprehensive review of the research on UAM is presented in [15], where the development of more refined and high-fidelity models is suggested as one of the potential research directions in this field. This work also points out the importance of taking into account the largest safety allowed by the hybrid-electric power systems in rotorcraft thanks to the possibility of performing safe descents after an engine/motor failure.

The authors of [14], proposed a comparison of the Greenhouse Gas (GHG) emissions of a VTOL over a distance of 100 km versus ground-based passenger cars and, in particular, a conventional internal combustion engine vehicle and a battery-electric vehicle. However, this work performs a simplified analysis: the part-load efficiency of the powertrain and the large variability of energy consumption of a road vehicle due to the effect of the traffic conditions are not taken into account. The different effects of traffic conditions and weather on the travel time of road and aerial vehicles are addressed in [12] where it is also pointed out that the travel time of a VTOL is much more predictable than that of a road vehicle.

A similar but more detailed analysis is performed in [16], in which the authors developed a model to quantify trip emissions using UAM and compared them with automotive-based trips. The authors of this study consider gasoline and electric vehicles as automotive technology and calculate the emissions associated with electricity production using the emission factor of the metropolitan area of Chicago and Dallas. Moreover, this work proposes the detour ratio (defined as the distance saved or gained by using an aerial vehicle instead of a road vehicle driving the same route) as a metric to compare air and road transportation while the circuitry factor (the ratio of the shortest road route to the Euclidian distance) is proposed in [12] to compare air and road vehicles.

The present work differs from [12,16] in the following aspects that constitute its novel contribution to the scientific literature on UAM:

- The UAM is modeled with a detailed approach for the battery that takes into account non-linear and aging effects and part-load efficiencies for the engine and the motor.
- Different powertrains (conventional, fully electric, and parallel hybrid electric) are considered for the air taxi and the role of energy management is addressed in the case of the hybrid electric powertrain.
- The emissions associated with the battery charging are calculated as a function of emission intensity of the electricity production, with particular reference to the European Union.
- The road vehicles considered in this investigation are different for today and 2035 technology and are analyzed under favorable and unfavorable driving conditions (in terms of traffic congestion, driving style, and circuitry factor).
- The performances of the electrified air taxis are evaluated with the battery at the start and the end of its life.

- The environmental impact is assessed with a new well-to-wing/wheel approach per km of straight or Euclidean distance between the initial and final place of the emission (i.e., taking into account different values of the circuitry factor for the road vehicles).

A more complete analysis of the environmental impact of road and air vehicles should be performed at the cradle-to-grave emissions level [16], i.e., taking into account all processes from the extraction to the discarding of materials (thus including production, operation, and disposal phases). However, this is beyond the scope of this investigation.

After this first introductory section, the present paper is organized as follows. The second section depicts the simplified sizing of the aerial vehicles and their specification. The third part describes the proposed detailed methodology for the energy analysis of aerial vehicles. Then, the road vehicles used for the comparison are presented and the procedure for the evaluation of the environmental impact is explained in session 5. Finally, the results for today and 2035 technologies are discussed, and the conclusions are drawn.

2. Simplified Sizing of the Air-Taxis

A hypothetical four-passenger vertical take-off and landing (VTOL) rotorcraft with co-axial rotors is considered as air taxi architecture. This is in line with the works proposed in the literature; see, for example [12,17], in which electric VTOL vehicles with four to five occupants are considered for UAM.

In this work, three different power systems are proposed and compared: conventional (turboshaft-based powertrain), full electric (Lithium-ion battery and permanent magnet motors), and parallel hybrid electric (combining the previous technologies). The evaluation of the air-taxi mass in the three cases is not a trivial issue and depends on the present-day and future values for specific power and density of the main components [18–25]. The goal of the investigation is to propose a methodology for the energy analysis of a complex power system for UAM, not to analyze a particular technology. However, it is interesting to point out the strong expected improvement in the components of an electrified power system and to show how this affects the results of the proposed methodology. For this reason, the data retrieved in the scientific literature for today and future (2035) technologies (Table 1) were assumed for the turboshaft engines, the electric machines (and their inverter), and the battery. The potential different contribution of the gearbox to the weight of the proposed powertrains is neglected for simplicity.

Table 1. Current and future values of specific power and energy densities ([19,25]).

Component	Specification	Unit	Today	2035
Turboshaft engine	Specific Power	(kW/kg)	4.3	7.7–11
Inverter	Specific power	(kW/kg)	2.2	9–19
Electric machine	Specific power	(kW/kg)	2	9–16
Lithium battery	Power Density	(W/kg)	520	745–1200
Lithium battery	Specific Energy	(Wh/kg)	144	250–400

It is important to mention the relation between battery power density and energy density. The values of Table 1 are related to batteries optimized for energy density (this is the normal choice for a fully electric system), but the design of a Lithium-ion battery can be aimed at optimizing the power density at the expense of energy density or vice versa [26]. The power density of a battery mainly depends on its C_{rate} , i.e., the maximum current at which the battery can be discharged, termed as a multiple of the battery nominal capacity [26]. In fact, the nominal continuous power ($P_{batt,nom}$) of a Lithium-ion battery in discharge can be expressed as:

$$P_{batt,nom} = C_{rate} \cdot C_{nom} \cdot N_s \cdot V_{cell} \quad (1)$$

where C_{nom} is the nominal capacity (in Ah), V_{cell} is the nominal voltage of a Lithium-ion cell (3.6 V), and N_s is the number of cells in the series. Assuming a nominal voltage of

270 V for the battery pack ($Ns \cdot V_{cell}$), as suggested by Bérubé et al. [20], it is easy to verify that the values in Table 1 refer to a battery with a continuous C_{rate} , ranging between 3 and 4, but higher values of the C_{rate} can be obtained even with today’s technology [21] and without significantly penalizing the energy density. It should also be noted that, for a short interval of time compatible with the duration of the take-off (about 30 s), the battery can be operated at a current higher than C_{rate} which is named burst C_{rate} and is generally equal to $2C_{rate}$ [24,26].

To obtain realistic specifications for the UAM powertrains, the following procedure is proposed here for fast preliminary sizing:

1. The empty mass is initially assigned equal to 1000 kg.
2. A payload of 360 kg is added in all cases to account for four passengers (including luggage) and a reserve of 50 kg of fuel is considered for the conventional and hybrid electric powertrains.
3. For each of the configurations considered in this work (conventional, parallel hybrid electric, and fully electric), a tentative value is assigned to the size of the components (nominal power for the energy converters, energy content for the battery).
4. Using the data of Table 1, the take-off mass of the powertrain is estimated for current and 2035 technology.
5. The empty weight is upgraded to keep the ratio of empty-to-take-off mass equal to 0.6 [14].
6. The take-off weight is used to estimate the take-off power. If this cannot be achieved with the proposed powertrain, the size of the converters is increased.

The iteration is terminated when the convergence on the empty mass is reached.

The take-off power is calculated as suggested in the literature [12,16] for VTOL vehicles by using the formula for the power request in hover:

$$P_{hover} = \frac{Mg}{\eta_p} \sqrt{\frac{\delta}{2\rho_a}} \tag{2}$$

where δ is the disk loading and ρ_a is the sea-level air density (1.22 kg/m^3), g is the gravity acceleration. For all the powertrains, a value of 0.85 was assumed for the propulsive efficiency [16] and the disk loading was set to 380 Nm^{-2} [16,27].

The results of the procedure are shown in Figure 1, Tables 2 and 3 in terms of final take-off mass and powertrain specifications.

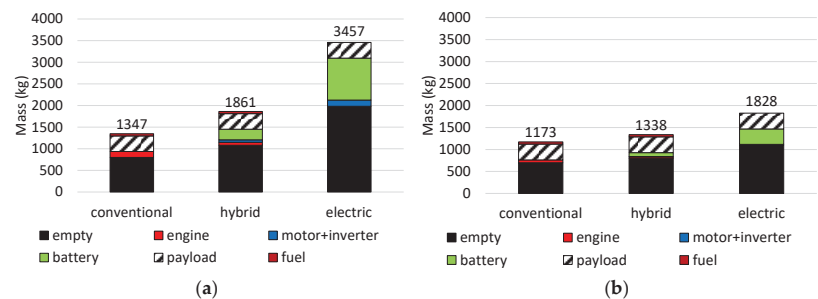


Figure 1. Estimated take-off mass (in kg) of the proposed powertrain for the aerial taxi. (a) Today’s technology; (b) 2035 technology.

Table 2. Specification of today's powertrains.

	Conventional	Hybrid	Electric
Engine size	2 × 295 kW	295 kW	-
Motor size	-	3 × 120 kW	5 × 120 kW
Battery size	-	35 kWh	140 kWh
Battery capacity (Ah) @ 270 V	-	130	520
Take-off power (kW)	194	268	498
Required battery C_{rate} (@ 270 V)	-	8	4

Table 3. Specification of the 2035 powertrains.

	Conventional	Hybrid	Electric
Engine size	2 × 295 kW	295 kW	-
Motor size	-	2 × 120 kW	4 × 120 kW
Battery size	-	35 kWh	140 kWh
Battery capacity (Ah) @ 270 V	-	130	520
Take-off power (kW)	169	193	263
Required battery C_{rate} @ 270 V	-	6	2

Regarding the take-off mass (Figure 1) the largest contribution of the powertrain to the take-off weight is associated with the battery, especially in the case of today's technology and fully electric aerial vehicles. It should also be noted that, at constant mass, the 2035 technology allows a designer to shift from conventional to hybrid (with about 1350 kg) and from hybrid to electric (accepting a take-off weight of about 1850 kg).

Regarding the installed power, in the conventional case, we considered a twin-engine configuration to allow safety in case of failure. The size of 295 kW (400 HP) was chosen according to the specification of the Hill GT500 engine [22]. Since it is difficult to scale down a turboshaft engine, the same nominal power was also considered for the 2035 technology. For the motors, we opted for modules of 120 kW since more powerful electric machines for aerospace applications are still under development [23]. The number of modules (N_{EM}) was chosen so that the take-off could be performed with ($N_{EM} - 1$) motors. The size of the battery was set equal to 35 and 140 kW for the hybrid and the full-electric case, respectively, based on the experience of the authors and with a trial-and-error procedure on the mission analysis described later in the paper.

For the hybrid electric taxi, take-off can be performed in thermal, electric, or power-assist modes. Since it is also necessary to guarantee that the battery can feed the motors in case of electric take-off, the minimum continuous C_{rate} required for the battery in the different cases was estimated and entered in Tables 2 and 4. Based on the previous discussion about the typical continuous and burst C_{rate} of today's battery, we can conclude that the battery is able to guarantee an electric take-off in all cases reported in Tables 2 and 3.

Table 4. Other specifications of the air taxis ([14,16]).

	Conventional	Hybrid	Electric
Today's L/D	6.21	7.32	5.98
2035 L/D	12	12	12

As a partial validation of the sizing procedure, it is possible to notice that the take-off mass obtained for the 2035 electric air taxis is very close to the value of 4000 lbs assumed in [11] for a UAV powered by a battery with 400 kWh/kg. However, the goal of this first step was not to propose a detailed sizing methodology but to obtain reasonable values for the take-off weights of the three powertrains to allow a fair comparison in terms of energy and power request.

3. Proposed Methodology for the Air-Taxi

Once the powertrain was defined, the energy and fuel consumptions were calculated with the procedure here explained and illustrated in Appendix A (Figure A1) for the hybrid propulsion system. Note that the fully electric and conventional powertrains can be considered as particular cases of this complex power system.

The simulations proposed in this investigation were performed with a quasi-static approach. Each mission was divided into intervals of time length h and, at any time step, the components of the power system were assumed to work in stationary conditions even if the working point was different at each time step. Such an approach is generally accepted in the minimization of fuel consumption in complex powertrains [26] because it allows the design of a supervisory controller to optimize the power flows in the propulsion system with a small computational effort. However, this approach requires the mission to be known a priori and is not able to handle feedback control problems or to take into account the dynamic response of the energy converters to a variable power request that affects the shaft dynamic in a rotorcraft or the dynamic behavior of the fuel valve [28]. A dynamic model of the whole power system, including the twin rotors, is currently being implemented by some of the authors of this investigation and preliminary results can be found in [29]. Note that a dynamic approach would be able to take into account other factors, such as the effect of temperature on each component of the power system, that are neglected in this investigation.

3.1. The Route (Start and Final Points)

The vehicles are supposed to perform the same hypothetical route which corresponds to a total straight-line or Euclidean distance of 70 km. When comparing air-taxi and ground-based transportation systems, it is necessary to take into account the circuitry factor, i.e., the ratio between actual road travel distance and coordinate-calculated Euclidean distance. A circuitry factor of 1.2 is considered in [30] for the comparison between air and road vehicles. However, this value is strongly variable from country to country, as pointed out in [18] where an average circuitry factor of 1.46 is reported for Europe.

It is important to point out that the trip time of the road taxi is strongly affected by driving style, weather, and traffic conditions. Headwinds or tailwinds, on the other hand, do not change the true airspeed (TAS) of the aerial vehicle even if they affect the groundspeed. However, frequent back and forth along a given air-taxi route would likely balance these changes [12].

3.2. Mission Profile and Flight Dynamics

Based on the white paper of Uber [11], a typical mission was considered, consisting of take-off, climb, cruise, descent, and landing. The proposed mission was characterized by a cruise altitude of 458.6 m and a cruise speed of 67 m/s (150 mph); as suggested in [11,27] the ROC (Rate of Climb) and ROD (Rate of Descent) were assumed equal to 2.54 m/s (500 ft/min) in the present investigation.

The shaft power request vs. time was estimated using literature methods and data ([16,27]). For the vertical take-off and landing, the power request was calculated as in Equation (2).

At cruise conditions:

$$P_{cruise} = \frac{Mg}{L/D} \frac{V}{\eta_p} \quad (3)$$

For climb and descent:

$$P_{climb} = \frac{Mg}{\eta_p} \left(ROC + \frac{V}{L/D} \right) \quad (4)$$

$$P_{descent} = \frac{Mg}{\eta_p} \left(ROD + \frac{V}{L/D} \right) \quad (5)$$

In these equations, M is the take-off mass of the vehicle and V is the true airspeed. The values of the propulsive efficiency η_p used in this investigation are reported in Table 2. The powertrain efficiency is included in the denominator of these formulas in the approach proposed in [16], while in the present investigation, η_p in Equations (2)–(5) is only the propulsive efficiency (i.e., the efficiency of the rotor) while the powertrain efficiency is calculated with the detailed model explained below.

It is also necessary to point out that in the conventional and hybrid-electric powertrains, the mass of the vehicle decreases in time due to the consumption of fuel. Even if this effect can be easily implemented in the proposed procedure, it is not considered here because the amount of fuel consumed in the reference mission was much smaller than the take-off mass of the vehicle, as shown later. Note that the total power requirements for VTOL flight include the additional power drawn from auxiliary systems such as avionics or passenger comforts (heating/cooling, phone charging, radio, etc.). As suggested in [16], these contributions are neglected in this investigation.

The time histories of the shaft power request for the three powertrains (according to their different masses) are reported in Figure 2.

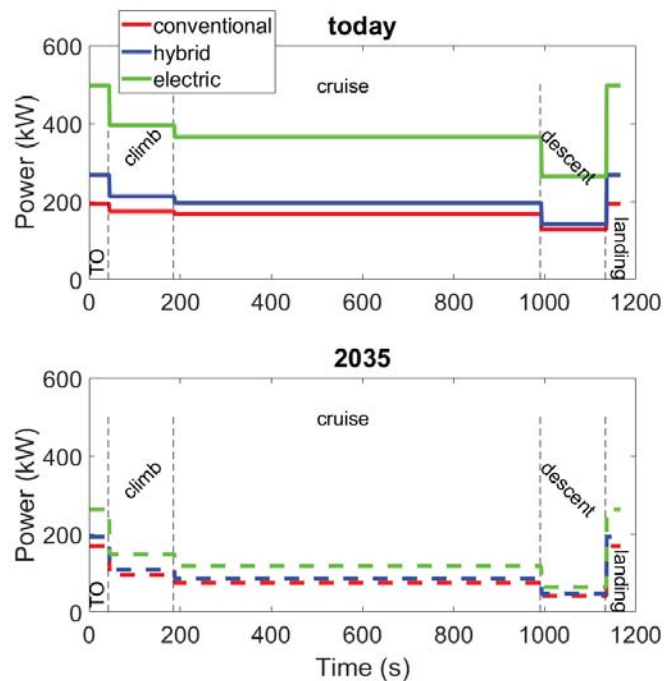


Figure 2. Power request of the three configurations with current and 2035 technology.

3.3. Simulation of the Energy Flows

The missions of Figure 2 were discretized with a time step of 1 s. At each time step, the required shaft power was used as input to the detailed model of the power system.

In the conventional case, the power shaft request is fulfilled by the engine. In the electric case, it is fully developed by the electric machines. For the hybrid electric powertrain, an appropriate energy management strategy must be defined because it can be operated in four different modes:

- *Thermal mode*: the electric drive is not used and the power request is entirely satisfied by the engine.

- *Electric mode*: the engine is turned off (or in failure) and the power request is fulfilled by the electric drive.
- *Power-assist mode*: both the electric machines and the engine give power to the shaft.
- *On-flight charge mode*: the turboshaft engine is used to meet the power request and to charge the battery during the flight.

Note that the on-flight charge mode was not implemented in this work because it was found to be of little utility in the case of air vehicles [31]. All the other modes can be obtained with a specific value of the control parameter u , which is defined here as:

$$u(h) = \frac{P_{EM}(h)}{P_{EM,nom}}, \text{ with } 0 \leq u \leq 1 \quad (6)$$

where $P_{EM,nom}$ is the nominal power of the electric machine, and $P_{EM}(h)$ is the contribution of the electric machine at time step h . Therefore, the power to be delivered by the thermal engine, $P_{ice}(h)$, is:

$$P_{ice}(h) = P_{shaft}(h) - P_{EM}(h) \quad (7)$$

Note that the denominator in the expression of the control variable u , Equation (6), should be the minimum between the nominal power of the electric motors and the available battery power. However, it has been already verified that the battery can satisfy the take-off power with reasonable values of the C_{rate} . Similarly, $P_{ice}(h)$ should be compared with the maximum power of the engine at the flight altitude $z(h)$ to ensure that the engine is able, at any moment, to satisfy the request. Since the engine is quite oversized (see Tables 2 and 4) and the other phases of the flight require much less power than take-off and landing (see Figure 2), this constraint is easily met.

In the authors' previous investigation [31], the ECMS (equivalent consumption minimization strategy) was proposed for a similar application to calculate the optimal $u(h)$. The Equivalent Consumption Minimization Strategy [26] considers the battery as an auxiliary fuel tank and converts its electrical energy into virtual fuel consumption. The virtual and actual fuel flow rates are combined to obtain the instantaneous equivalent fuel consumption in the following way:

$$\min(\dot{m}_{eq}) = \dot{m}_f(h) + f_{eq} \cdot P_{batt}(h) \cdot f_p(h) \quad (8)$$

where the equivalence factor f_{eq} converts the battery power to a virtual fuel flow rate. The virtual fuel flow rate can be either positive or negative according to the sign of the battery power (battery charged or discharged). Thus, the equivalent fuel consumption can be higher or lower than the actual fuel consumption in the ECMS original strategy. The penalty factor f_p is a correction that accounts for the divergence of the current SOC from the (constant) desired value of the battery state of charge (SOC_{ref}). In this investigation, the penalty factor f_p is calculated according to the deviation of SOC at timestep h from a reference curve $SOC_{ref}(h)$:

$$x(h) = \frac{SOC(h) - SOC_{ref}(h)}{SOC_{ref}(h)} \quad (9)$$

$$f_p(h) = (1 + |x|)^p \quad (10)$$

The optimal values of f_{eq} and p were obtained in a previous work [31].

According to the results of [31], we selected a reference SOC curve that decreases linearly over time, except in cruise where it is kept constant (the battery is not used).

During each simulation run with the proposed strategy, local optimization was performed at each time step h of the mission, by considering all the values of u ranging between 0 and 1 with a step of 0.1 and choosing the value of u corresponding to the minimum of \dot{m}_{eq} . In other words, an enumerative optimization technique was used. However, other

local search methods could have been used when the strategy was applied online in the UAM vehicle.

The ECMS has the main goal of minimizing fuel consumption during the mission. However other targets can be considered specifically for air-taxi operation. For this reason, we propose in this investigation a simple rule-based strategy aimed at reducing the environmental and acoustic impact of the hybrid-electric configuration during take-off and landing. To this scope, take-off and landing are performed in electric mode and cruise in thermal mode. The climb phase is performed in power assist mode (with $u = 1$) until the SOC reaches a threshold value (90%) to obtain the desired SOC_{ref} curve. The other phases of the flight are performed in thermal mode.

3.4. Total Fuel Burn in the Mission (M_f)

The total fuel burn is calculated starting from the $P_{ice}(h)$ of the turboshaft engine with a simple empirical model, developed in a previous investigation [31]. The specific fuel consumption $SFC(h)$ at each time step is estimated as:

$$\frac{SFC(h)}{SFC_0} = \left(\frac{P_{ice}(h)}{P_{ice,nom}} \right)^{b_2} (z_1 Z(h) + z_0)(m_2 M + m_1 M + m_0) + b_1 \quad (11)$$

where Z is the altitude (in meters) and M is the Mach number (note that this effect is negligible for this application). $P_{ice,nom}$, and SFC_0 are the shaft power and the specific fuel consumption of the engine at its design point, respectively. This equation contains seven parameters ($b_1, b_2, m_0, m_1, m_2, z_0, z_1$) whose values were fitted in [31] by comparison with a detailed model of the engine.

The fuel flow rate is calculated as $m_f(h) = SFC(h, j) \cdot P_{ice}(h)$. By numerically integrating $m_f(h)$, the total fuel burn M_f is obtained for the conventional and hybrid electric power system.

3.5. Electric Consumption of the Mission E_{tot}

The power contribution of the electric machines is used as input to calculate the electricity consumption. Each electric machine (inclusive of the driver) is modeled with a simple Willans line as proposed by [26] so that the battery current can be expressed as:

$$P_{batt}(h) = \frac{P_{EM}(h) + P_0}{e} \quad (12)$$

where e is the intrinsic efficiency of the electrical-to-mechanical energy conversion process and P_0 accounts for the losses taking place after the energy conversion (friction, heat losses, etc.). In this investigation, we assumed $e = 0.9$ and $P_0 = 1.4$ kW as reported in [26] for permanent magnet machines.

The battery is simulated with an electric equivalent circuit [26]. The Open-Circuit Voltage OCV is a function of the battery state of charge, while the internal resistance R is considered independent of the SOC but related to the specification of the battery and varying along with the battery life. Therefore, the battery current is calculated by solving the following equation:

$$P_{batt}(h) = [OCV(h) - R(t) \cdot I(h)] \cdot I(h) \quad (13)$$

By integrating the battery power, the total electric consumption of the mission E_{tot} is obtained for the hybrid electric and full electric power systems.

The battery is also affected by the Peukert effect, i.e., the battery's actual capacity decreases when the discharge power is increased. To take into account this phenomenon, the effective current I_{eff} is calculated as:

$$I_{eff}(h) = I(h) \cdot \left(\frac{I(h)}{I_{nom}} \right)^{n-1} \quad (14)$$

where n is the Peukert coefficient, I_{nom} is the current at which the nominal capacity of the battery is obtained.

Using the effective current, the state of charge is upgraded, at any time during the mission, as:

$$SOC(h) = SOC_{in} - 100 \cdot \sum_1^N \frac{I_{eff}(t)}{C} \quad (15)$$

where SOC_{in} is the battery state of charge at the beginning of the mission. The Depth of Discharge (DOD) is calculated as the change between the initial and final SOC of the battery in each mission.

With this modeling approach, it is possible to take into account the increase in battery current at constant power due to the reduction in the SOC which, in turn, determines a reduction in the OCV. Another important characteristic of the proposed battery model is that the values of capacity, internal resistance, and Peukert coefficient are updated with the battery state of health. In particular, the values of these parameters at the beginning and the end of the battery life are shown in Table 5. For more details about the aging model, please refer to [32].

Table 5. Values assumed for the battery parameters.

Battery Status	Capacity (Ah)	R_i (Ω)	n
New	C_{nom}	9.54e-5	1.09
Aged (End of life)	$0.8C_{nom}$	11.75e-5	1.19

The end of life for a vehicle drive battery is defined as the time when either the battery energy capacity or its available power (which is inversely proportional to the internal resistance) drop below a specified minimum, which is usually set equal to 80% of the initial value [33]. The time at which this condition is reached is the minimum between the cycle life (degradation due to repeated charge–discharge cycling) and the calendar life (degradation over time). Calendar and cycle life are affected by the battery operation, and in particular operating temperature, DOD, and charge/discharge current [34]. The dependence on DOD can be found in the datasheet provided by the battery manufacturer or estimated with the models proposed in the scientific literature (see for example [35,36]).

4. Reference Road Vehicles

The emissions of CO₂ of the different powertrains for air taxi will be compared with those of a road vehicle performing the same mission. Recently, the European Commission revised the Regulation setting CO₂ emission standards for cars and light commercial vehicles, reducing the target value by 37.5% in 2030 compared to the 2021 limit of 95 g CO₂/km. However, this value refers to the whole fleet and only the Tank-to-Wheel emissions are considered. For a more detailed comparison, reference road vehicles are used in this investigation.

The vehicle used as an example of today's road technology is a well-known series/parallel hybrid electric vehicle, the Toyota Prius. The reason for the choice of this car is twofold: it is one of the most common vehicles used as a road taxi and is the most-studied hybrid electric vehicle (see, for example [37]). The Prius non-plug-in vehicle has a curb mass of 1470 kg and a declared fuel consumption of 4.8 L/km over the New European Driving Cycle. However, tests performed on the same vehicle [38] revealed that the fuel consumption (FC) of the Prius can range between 3 and 6 L/100 km on regulatory cycles (depending also on the version of the vehicle) while a still higher variability is obtained in real driving conditions [39] where the fuel consumption can be as high as 14.8 L/100 km in case of urban routes and aggressive driving styles. Note that the curb mass of the Toyota Prius is 1350 kg. By adding the same payload of the aerial vehicle (360 kg), a mass of

1710 kg is obtained, a value not much different than that of the hybrid electric air taxi with today's technology.

The fully electric Nissan Leaf was chosen as exemplative of 2035 road taxi because it is one of the most-studied electric vehicles and was also proposed for road-taxi services [40]. The Nissan Leaf has a range of 200 km and a nominal electric consumption of 0.17 kWh/km [41]. The expected improvement in technology for this kind of vehicle in 2035 is difficult to evaluate. For simplicity, we will assume that the expected increased energy density will allow the usage of a larger battery with the same mass. This will translate into a strong increase in range that will enhance the usage of vehicles as taxi service, but the energy consumption will be quite unchanged. Note that the electricity consumption must be corrected with the circuitry factor, as in the case of the Toyota Prius, before performing the comparison with the aerial taxi. Moreover, the effects of traffic conditions and driving style are also to be considered [42]. For the Nissan Leaf, the study in [43] reports a value of 0.24 kWh/km in real driving conditions.

5. Environmental Impact

To compare the different vehicles from an environmental point of view, a Well-To-Wheel/Wing approach is considered, i.e., the greenhouse emissions are calculated considering the whole process from the primary energy source (e.g., crude oil) to the final energy to the wheels/wings. Moreover, they are normalized to the Euclidean distance between the initial and final places of the mission. To this scope, for gasoline and kerosene, it is possible to assume 3.15 kg_{CO2}/kg_{fuel} for the Tank-to-Wheel conversion, and 0.55 kg_{CO2}/kg_{fuel} for the WTT. In other words, the WTT emissions account for 15% of the WTW contribution [44]. The grams of CO₂ per km of Euclidean distance (*ED*) of the aerial vehicle are calculated as:

$$\text{CO}_2, \text{ thermal, aerial} = \frac{3.7M_f}{1000 \cdot ED} \quad (16)$$

where M_f is expressed in kg and ED in km.

To account for the circuitry factor, the WTW emissions of CO₂ of the Toyota Prius per km of Euclidean distance are calculated as:

$$\text{CO}_2, \text{ thermal, road} = 10 \cdot FC \cdot \rho_{\text{gasoline}} \cdot CF \cdot 3.7 \quad (17)$$

where FC is the fuel consumption in l/100 km, $\rho_{\text{gasoline}} = 0.755$ kg/L, CF is the circuitry factor, and 3.7 kg_{CO2}/kg_{fuel} is the WTW emission factor gasoline.

The contribution associated with the electricity for the aerial vehicles is linearly proportional to the amount of electricity released by the battery (E_{tot}). To account for the losses in the grid and at the charging station, an overall efficiency η_{charge} is introduced and its value is set to 80% [45]:

$$\text{CO}_2, \text{ elec, aerial} = EI \cdot \frac{E_{\text{tot}}}{\eta_{\text{charge}} ED} \quad (18)$$

where EI is the Emission Intensity factor in g/kWh for the production of electricity.

The Toyota Prius considered in this work is not a plug-in vehicle, therefore there was no electric consumption associated with the mission and the battery was continuously charged and discharged thanks to the presence of the engine (charge-sustaining strategy). For the Nissan Leaf, the electric consumption per km was corrected to take to account the circuitry factor. The same values of EI and charge efficiency of the aerial vehicle are used in this case:

$$\text{CO}_2, \text{ elec, road} = EI \cdot CF \cdot \frac{EC}{100 \cdot \eta_{\text{charge}}} \quad (19)$$

where EC is the electric consumption expressed in kWh/100 km.

For the emission intensity factor EI , a sensitivity study was conducted. In fact, even if electricity generation from renewable sources has significantly increased in the last years, most of the electric energy is currently produced from fossil fuels [46,47].

According to the European Energy Agency (EEA [48]), the greenhouse Emission Intensity for EU in 2019 is, on average, 275.0 g CO₂/kWh with a maximum of 891 g CO₂/kWh for Estonia and a minimum of 8 g CO₂/kWh for Sweden as shown in Figure 3a, where the value for Italy is also shown. However, the greenhouse emission intensity is expected to be reduced significantly in the next future. In this investigation, we will consider the average value of 90 g CO_{2eq}/kWh as the projected value in 2035.

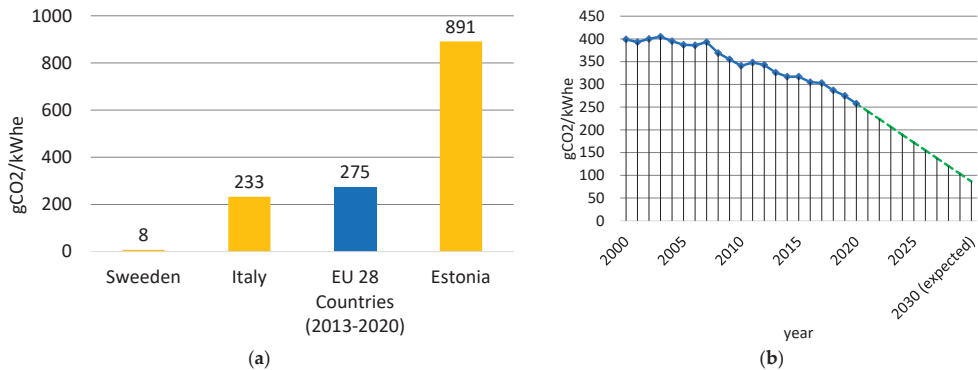


Figure 3. Past, present, and future emission intensity of European countries (elaboration of data from www.eea.europa.eu (accessed on 22 August 2021)). (a) Greenhouse Emission intensity in Europe (2019); (b) the trend of Greenhouse Emissions intensity vs. years (average value for EU 28 countries).

6. Results

The overall results of the proposed methodology are shown in Table 6 in terms of burn fuel M_f , electric consumption E_{tot} , and battery DOD for the proposed configurations. Note that with today's technology, the overall energy consumption of the air taxi is very high for all the configurations but in particular for the full electric because of its very large mass.

Table 6. Burn fuel, electricity consumption, and battery DOD for the air taxi.

	Today			2035		
	M_f (kg)	E_{tot} (kWe)	DOD (%)	M_f (kg)	E_{tot} (kWe)	DOD (%)
Conventional	23.87	-	-	16.15	-	-
Hybrid ECMS	21.46	14	40.06	9.77	14.05	40.04
Hybrid Rule-based	21.6	13.04	37.16	13.5	7.5	21.4
Electric	-	132.5	94.4	-	41.7	29.7

Starting from conventional powertrains, we can see that with current and 2035 technology the fuel consumption is 34.1 and 23.1 kg/100 km, respectively. Such levels of consumption are very high when compared with those typical of the Toyota Prius.

For the hybrid solution, the consumption strongly depends on the energy management strategy because of the different power distribution, as shown in Figure 4.

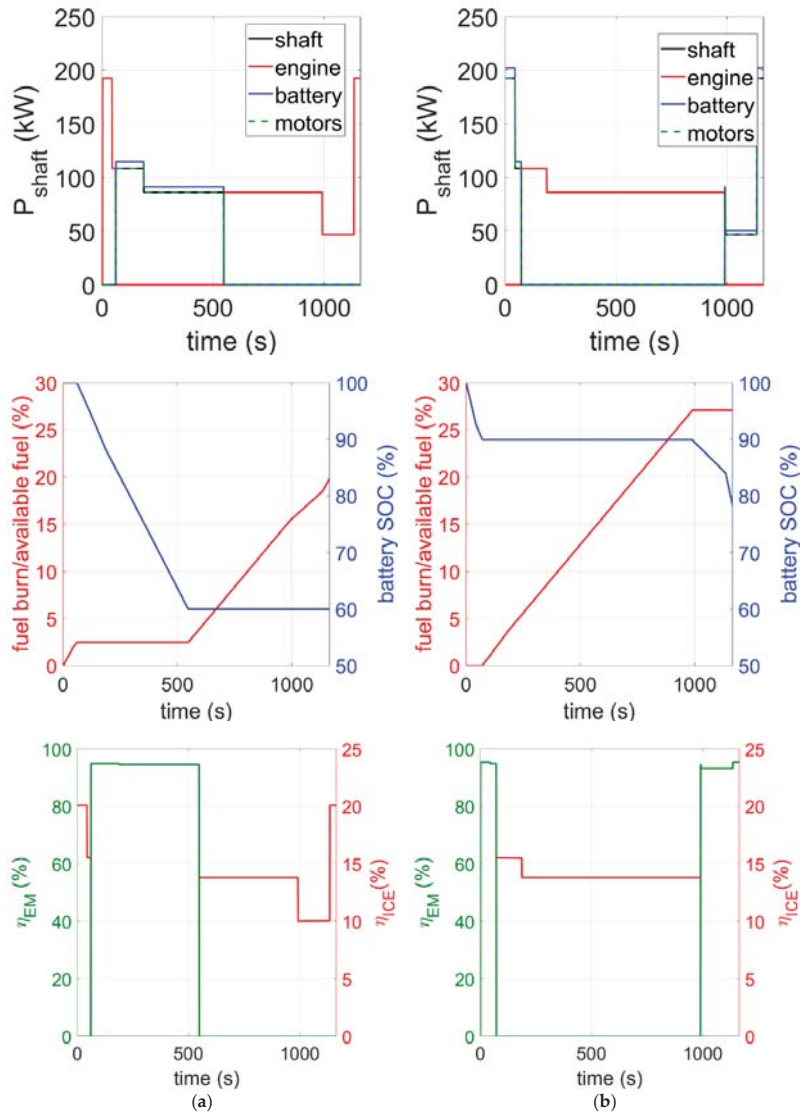


Figure 4. Power distribution, consumption, and efficiency time histories for the hybrid electric taxi with 2035 technology. (a) ECMS; (b) rule-based.

The ECMS strategy guarantees the best fuel economy because it allows the battery to be discharged up to the desired threshold of 60% at the end of the mission (for backup operation). With 2035 technology, the fuel consumption in the case of rule-based strategy is 38% higher than that obtained with the ECMS while the electric consumption is 46.6% lower. The higher fuel consumption obtained with the rule-based strategy is mainly associated with the lower usage of the battery. However, the rule-based strategy guarantees a reduction in emissions at the road level because take-off, landing, and part of the climb are performed in electric mode (see Figure 4). Moreover, the lower DOD obtained with this strategy is advantageous in terms of both battery life and charging time between two

consecutive flights. The bottom plots of Figure 4 show the efficiency curves of the motor and the engine in the two cases.

In the case of ECMS, engine efficiency is strongly dependent on the flight phases, like in a conventional aircraft. With the rule-based strategy, the engine is used only for cruise and part of the climb and is, therefore, quite oversized. This makes the engine work with an efficiency lower than 15% in the cruise phase. From a thermal efficiency point of view, it would be useful to choose a smaller engine or to select a different kind of thermal converter such as, for example, a piston engine. However, a smaller engine would not be able to perform take-off and landing in case of failure of the electric drive.

As for the electric powertrain, today's technology with the proposed size of the battery is not suitable for the mission considered in this study. In fact, the DOD is very high, and the electric consumption is 1.84 kWe/km. The very high DOD is not only detrimental to the battery life and charge time but also does not allow reserve hover time. Note that at the moment there is no official regulation from aviation authorities about the reserve energy of the battery [12].

In the case of 2035 technology the electric consumption is reduced to 0.58 kWe/km, which is still much higher than the value registered for the Nissan Leaf vehicle in the worst conditions (0.24 kWe/km). A smaller DOD could be obtained by choosing a larger battery. However, this would significantly increase the take-off weight of the fully electric vehicle according to the sizing procedure described in Section 2.

6.1. WTW Analysis with Today Technology

Figure 5 shows the WTW emissions of the air-taxi configurations with today's technology as a function of the Emission Intensity of electricity production. For simplicity, only the results with the rule-based strategy are reported for the hybrid electric vehicle. The best and worst cases related to the road taxi (Toyota Prius) were obtained with the following procedure.

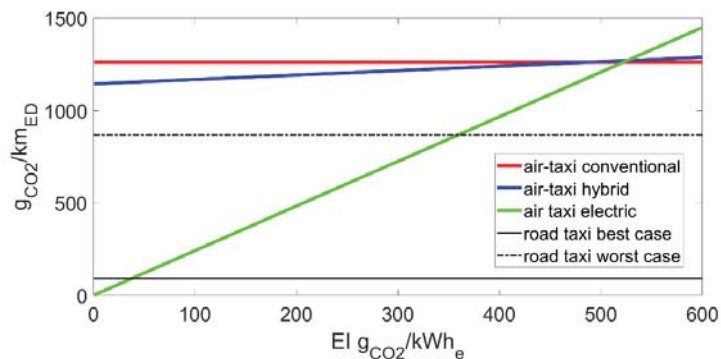


Figure 5. Comparison of WTW emissions of CO₂ per km of Euclidean distance with today technology.

The circuitry factor was increased from 1.1–2.1 [30] and Equation (17) was applied with the two values of fuel consumption (3 and 14.8 L/100 km) representative of the best and worst conditions of traffic and driving style for the Toyota Prius to obtain the plot of Figure 6. In the same plot, it was demonstrated that the WTW emissions of CO₂ per km of Euclidean distance ranged in the interval 92–868 g/km_{ED}. These are the values reported in Figure 5 as best and worst cases for the road vehicle.

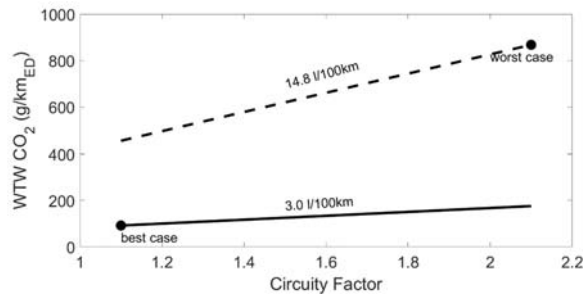


Figure 6. Equivalent WTW emissions of CO₂ of the Prius as a function of circuitry factor, traffic conditions, and driving style.

From the curve of Figure 5, we can notice that the air taxi with conventional or hybrid electric power systems generates levels of WTW emissions per km much higher than the road vehicles, even in the worst case. For the hybrid electric powertrain, the Emission Intensity of the electricity production has a weak effect on the overall values. The emissions of the full-electric air taxi are below those of the road vehicle under the best and worst driving conditions if the EI is below 40 and 360 g/kWe, respectively.

6.2. WTW Analysis with 2035 Technology

The final comparison with 2035 technology is shown in Figure 7. For the Nissan Leaf (road taxi) the best and worst cases were calculated with the following values: 24 kWh/100 km and a circuitry factor of 2.1 as the worst case, 17 kWh/100 km and CF = 1.1 as the best case.

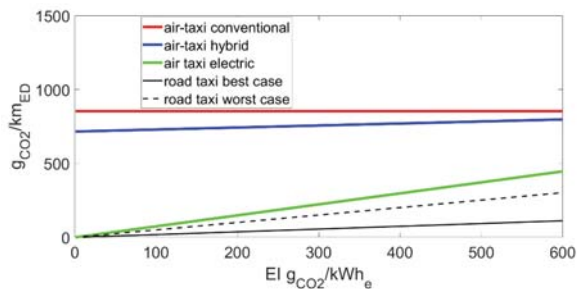


Figure 7. Comparison of WTW emissions of CO₂ per km of Euclidean distance with 2035 technology.

Even in the worst conditions, the electric road taxi is advantageous over the air taxi in terms of overall WTW emissions of CO₂ per km_{ED}.

The WTW emissions with the expected Emission Intensity of 90 g/kWe for the European Union in 2035 are quite low (67 g/km) for the full electric air taxi. Moreover, if all road taxis would be replaced by aerial vehicles, there would be a significant improvement in the traffic level with positive effects on the consumption and emissions of the whole road fleet.

Note that the two electric vehicles (road and electric air taxi with 2035 technology) have about the same mass (curb + payload) but the power demand of the aerial vehicle is much higher because of the very high cruise speed (240 km/h). As a consequence, the flight time is about 20 min while the road taxi would take from 1 to 2.5 h according to the traffic conditions with a circuitry factor of 1.28 [11,49].

To understand the corrective measures to be taken to reduce the unfavorability of aerial vs. road vehicles, it is sufficient to analyze the terms in Equation (3) since the cruise

is the most relevant flight phase in terms of energy consumption. For the road vehicle, the power request at the wheel at constant speed V and no road grade can be calculated as:

$$P_{wheel} = \frac{1}{2}c_d A_f \rho_a V^3 + c_r M g V \quad (20)$$

where c_d is the aerodynamic coefficient, A_f is the frontal area of the vehicle, c_r is the rolling friction coefficient, and ρ_a is the ambient air density. Assuming the same mass of 1800 kg for each vehicle and suitable values of $c_d A_f$ (0.7 m^2) and c_r (0.012) for a full-sized vehicle [26], the power request of the road vehicle is shown in Figure 8 and compared with those of the air taxi at the same speed (calculated from Equation (3)). Note that the road taxi power is lower than that of the aerial vehicle up to about 210 km/h, which is, however, too high a speed for a road vehicle. Moreover, improvement in $c_d A_f$ and c_r can be expected in the future for road vehicles that would further reduce the energy request of these vehicles.

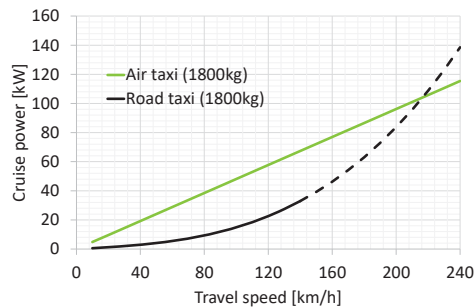


Figure 8. Cruise power vs. travel speed for an air vehicle and a road taxi with the same mass.

For the aerial vehicle, the cruise power is equally influenced by L/D and propulsive efficiency so a strong improvement of one or more of these parameters would be needed to reduce the energy consumption at constant cruise speed.

6.3. Effect of Battery Aging

The results shown in the previous section were obtained with a battery at the start of its life. If the battery-aging phenomena were considered, the same trip would require more electricity to charge the battery (because the battery would be discharged faster) and the battery would not be able to sustain the selected mission (in particular in the case of the electric vehicle with today's technology).

To take into account the effect of battery aging, the energy consumption of the hybrid electric and electric power systems with 2035 technology was recalculated with the battery at the end of its life (equivalent to 400 full discharge–recharge cycles). The results are shown in Table 7. For the hybrid electric case, only the results with the rule-based strategy are shown in Figure 9. We noticed that the aging of the battery determined a slight increase in fuel consumption (+1.5%) because of the rules used during the climb. In fact, in this phase of the flight, the battery is used until its SOC reaches the value of 90%. In the case of the aged battery, this threshold is reached at the end of take-off so the climb is performed only in thermal mode. Because of the reduced capacity, increased internal resistance, and increased Peukert coefficient, the electric consumption is 12 and 27% higher for the hybrid-electric and electric configuration, respectively. The DOD is also significantly increased in both cases with a reduction in the number of consecutive missions that the vehicle can perform before fully charging the battery. The DOD affects the charging time between two subsequent flights, which also depends on the charging current. Rapid charging introduces problems in terms of charging cost, reduces the battery life, and compromises the energy density (because there is a tradeoff between energy density and power density in the design of the batteries, as already explained).

Table 7. Effect of battery aging of consumption (with 2035 technology, rule-based strategy for the hybrid power system).

	New Battery			Aged Battery		
	Burn Fuel (kg)	Electricity (kWe)	DOD (%)	Burn Fuel (kg)	Electricity (kWe)	DOD (%)
Hybrid	13.5	7.5	21.4	14.04 (+1.5%)	9.5 (+12%)	27.0
Electric	-	41.7	29.7	-	52.9 (+27%)	37.7

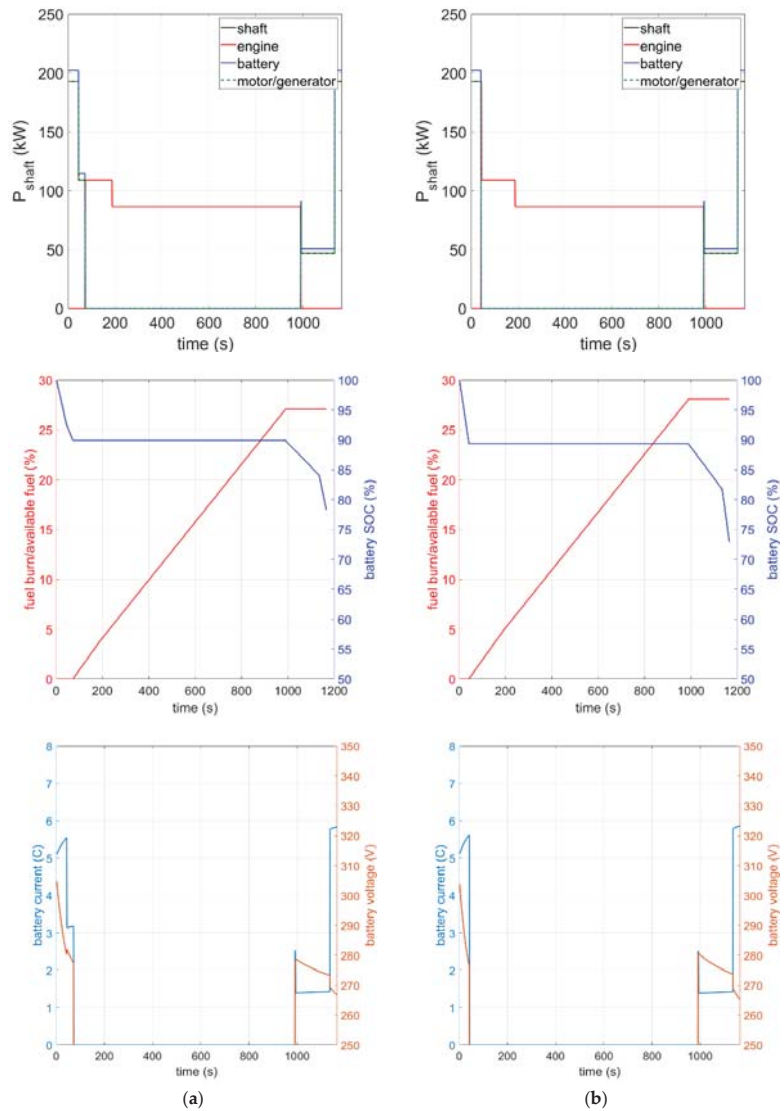


Figure 9. Effect of battery aging on the behavior of the hybrid electric air taxi (the hybrid electric taxi with 2035 technology). (a) new battery; (b) aged battery.

For a fully electric taxi, Uber [11] suggests that the vehicle should be operated continuously for at least 3 h without reaching the minimum reserve state of charge (30%) and with a 7 min recharge between each flight to partially recharge the battery. To do this, Uber suggests limiting the DOD in each mission and partially charging the battery between each mission. This approach was used here to estimate the number of consecutive missions with different levels of charging between them. This quantity was denoted as DOC (Depth of Charging) and varied between 0 (no charge) and 20%, meaning that the initial state of charge for a mission was set equal to the final SOC of the previous mission plus DOC. The simulation ended when the SOC reached the threshold of 20%. The procedure is illustrated in Figure 10 with specific reference to the electric air taxi with 2035 technology and the battery at the beginning of its life. The arrow in the Figure 10 explains the concept of DOC. The results obtained in the other cases are shown in Table 8. Note that the higher the DOC, the longer the charging time between two missions. The estimation of the charging time was not performed in this investigation because it is not relevant to the goal of this investigation.

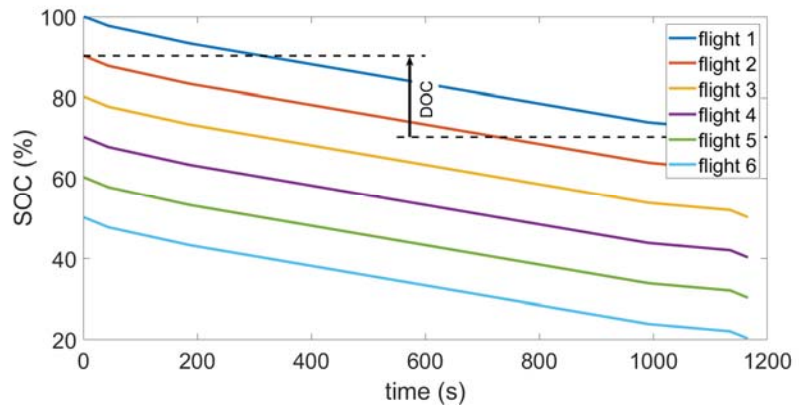


Figure 10. Repeated flights with DOC = 20% for the electric air-taxi with 2035 technology and new battery. The arrow shows the increment of charge (DOC) between the end of flight 1 and the beginning of flight 2.

Table 8. Effect of battery aging on the number of consecutive flights.

	New Battery			Aged Battery		
	DOC = 0%	DOC = 10%	DOC = 20%	DOC = 0%	DOC = 10%	DOC = 20%
Hybrid	3	7	(DOD = DOC)	2	3	7
Electric	2	3	6	2	2	3

In the case of a hybrid-electric vehicle with a DOD of 20% and a new battery, the vehicle can operate continuously because the DOD is almost equal to the DOC, while in the case of an aged battery it is possible to perform seven consecutive flights. For the fully electric vehicle, the continuous flight is obtained with DOC = 29.7% when the battery is at the beginning of its life.

The number of consecutive flights without full charge is very limited (two) in the case of DOC = zero, i.e., without intermediate partial charging for both the hybrid and the electric aerial taxis.

7. Summary and Conclusions

A new and detailed methodology was developed to analyze the performance of conventional, hybrid electric, and full-electric air taxis and to compare their environmental

impact with road taxis performing the same route. The novel contribution to the state of the art is in the detailed modeling approach of the powertrains, the evaluation of CO₂ emissions with a Well-to-Wing approach as a function of the electricity Emission Intensity factor, and the comparison with road vehicles performing the same route in different driving conditions.

In particular, the air taxis were designed according to current and 2035 technology and modeled with an in-house simulation tool. The proposed simulation approach computes the off-design efficiencies of the engine and motor during the mission and accounts for battery non-linear discharge effects (such as the Peukert dependence of capacity from discharge current) and aging phenomena. In the case of the hybrid-electric air taxi, two different energy management strategies were considered and compared.

Reference vehicles were selected for comparison with road taxis and literature values were assumed for the consumption of these vehicles in real driving conditions. The comparison demonstrated the advantages of the electrified air taxi with today's technology over a hybrid-electric road taxi, especially in the case of low emission intensity of the electricity production and penalizing boundary conditions (congested traffic, aggressive driving style, and high values of circuitry factor). In the case of 2035 technology, the comparison with a fully electric road vehicle was unfavorable but the WTW emissions with the expected Emission Intensity of 90 g/kWe for the European Union in 2035 were quite low (67 g/km). Note that these results could be interpolated for a reasonable estimation of the energy consumption and CO₂ emissions with short-term improvement (such as, for example, 2025 technologies).

The results of the simulation performed with the aged battery underlined the negative effect of this phenomenon on the consumption of the air taxi and on the number of consecutive flights that can be performed with fast intermediate charging of the battery. These results stress the importance of improving the battery technology not only in terms of power and energy density but also in terms of calendar and cycle life to enhance the usage of electrified propulsion systems as an air-taxi service. In future work, the authors will tackle the development of a dynamic model of the hybrid electric power system to account for the shaft dynamic of the rotorcraft and the transient behavior of the fuel system of the turboshaft engine.

Author Contributions: Conceptualization, T.D. and A.F.; methodology, T.D.; writing—original draft preparation, T.D.; writing—review and editing, T.D. and A.F. All authors have read and agreed to the published version of the manuscript.

Funding: This research received no external funding.

Conflicts of Interest: The authors declare no conflict of interest.

Abbreviations

CF	Circuitry Factor
DOC	Depth of intermediate Charge
DOD	Depth Of Discharge
EC	Electric consumption of the plug-in vehicle in kWh/100 km
ECMS	Equivalent Consumption Minimization Strategy
ED	Euclidean distance
EEA	European Energy Agency
EI	Emission intensity of the electricity production system
eVTOL	Electric Vertical Take-off and Landing
FC	Fuel consumption of the road vehicle in liter/100 km
GHG	Greenhouse Gas
TTW	Tank-To-Wheel/Wing
UAM	Urban Air Mobility

VTOL	Vertical Take-off and Landing
WTT	Well-To-Tank
WTW	Well-To-Wheel/Wing
A_f	Frontal area of the road vehicle
b_1, b_2	Parameters of the engine model
c_d	Aerodynamic coefficient of the road vehicle
c_r	Rolling coefficient (road vehicle)
C_{nom}	Nominal capacity of the battery
C_{rate}	Battery charging rate
e	Parameter of Willans line model of the motor
E_{lot}	Total electric consumption in the mission
f_{eq}	Equivalence factor of the ECMS strategy
$f_p(h)$	Penalty function of the ECMS strategy
g	Gravity acceleration
h	Interval of time in the mission discretization
$I(h)$	Battery current at time step h
$I_{eff}(h)$	Effective current of the battery
I_{nom}	The current at which the nominal capacity C of the battery is defined
L/D	Lift to Drag ratio
m_0, m_1, m_2	Parameters of the engine model
M	Take-off mass
m_f	Fuel flow rate
M_f	Total fuel burn in the mission
n	Peukert coefficient (battery model)
N_{EM}	Number of electric motors
$OCV(h)$	Open circuit voltage of the battery at time step h
p	Parameter of the ECMS strategy
P_0	Parameter of Willans line model of the motor
$P_{EM,nom}$	Nominal power of the electric machines
P_{EM}	Power demand for the electric machines
$P_{batt}(h)$	Battery power at time step h
P_{ice}	Power demand of the internal combustion engine
P_{shaft}	Shaft power demand
R	Internal resistance (Battery model)
ROC	Rate of Climb
ROD	Rate of Descent
$SFC(h)$	Specific Fuel Consumption at time-step h
SOC_{in}	State of the charge of the battery at the beginning of the mission
$SOC_{ref}(h)$	Reference SOC curve
SOC	Battery State of Charge
TAS	True Air Speed
$u(h)$	Control variable of the energy management
V	Speed
$x(h)$	Deviation of SOC at time step h from the reference SOC curve
z_0, z_1	Parameters of the engine model
η_{charge}	Overall efficiency of the battery charging process
η_p	Propulsive efficiency
ρ_a	Sea-level air density
$\rho_{gasoline}$	Gasoline density

Appendix A

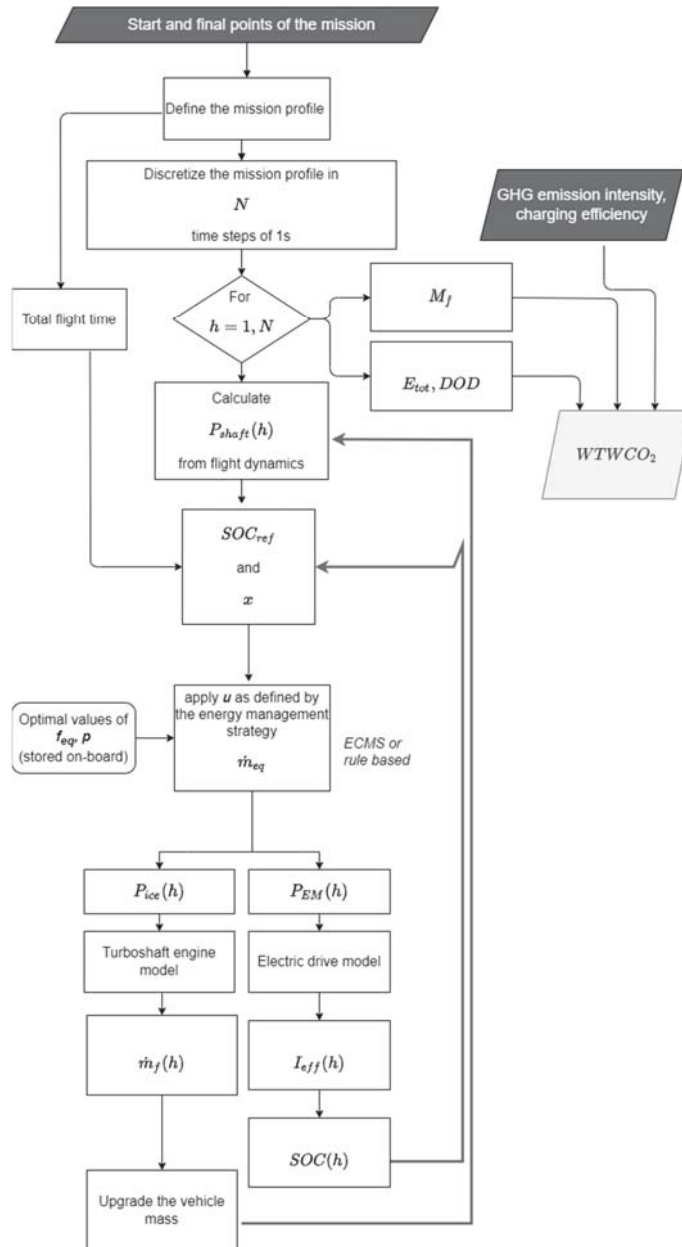


Figure A1. Flowchart of the proposed procedure.

References

1. Angel, S.; Parent, J.; Civco, D.L.; Blei, A.M. *Making Room for a Planet of Cities*; Lincoln Institute of Land Policy: Cambridge, MA, USA, 2011; ISBN 978-1-55844-212-2.
2. Papadopoulos, E.; Aggelakakis, A.; Tromaras, A. The Future of the European Transport Sector: Identifying the Key Trends Regarding the Transport Concepts of the Future. In Proceedings of the International Conference on Traffic and Transport Engineering—ICTTE, Belgrade, Serbia, 27 September 2018.
3. A European Strategy for Low-Emission Mobility. Available online: https://ec.europa.eu/commission/presscorner/detail/en/MEMO_16_2497 (accessed on 22 August 2021).
4. Malaud, F. Urban Air Mobility: Is This a Different Way of Saying “Aviation in Cities”? Available online: <https://unitingaviation.com/news/safety/urban-air-mobility-is-this-a-different-way-of-saying-aviation-in-cities/> (accessed on 9 March 2021).
5. Galindo, A. Detect-and-Avoid (DAA): How Airborne Collision Avoidance Works. Available online: <https://www.irisonboard.com/detect-and-avoid-how-airborne-collision-avoidance-works/#:~:text=However%2C%20the%20majority%20of%20manned,commonly%20flown%20at%20low%20altitudes> (accessed on 10 March 2021).
6. Honeywell International Inc. Autonomy and Avionics for Urban Air Mobility. Available online: <https://aerospace.honeywell.com/en/learn/products/navigation-and-radios/autonomy-and-avionics-for-urban-air-mobility> (accessed on 10 March 2021).
7. Electric Propulsion for a Disruptive Mobility Concept. Available online: <https://www.rolls-royce.com/products-and-services/electrical/propulsion/air-taxis.aspx> (accessed on 10 August 2021).
8. Goodchild, A.; Toy, J. Delivery by drone: An evaluation of unmanned aerial vehicle technology in reducing CO₂ emissions in the delivery service industry. *Transp. Res. Part D* **2018**, *61*, 58–67. [CrossRef]
9. Kirschstein, T. Comparison of energy demands of drone-based and ground-based parcel delivery services. *Transp. Res. Part D Transp. Environ.* **2020**, *78*, 102209. [CrossRef]
10. Zhang, J.; Campbell, J.F.; Sweeney, D.C.; Hupman, A.C. Energy consumption models for delivery drones: A comparison and assessment. *Transp. Res. Part D Transp. Environ.* **2021**, *90*, 102668. [CrossRef]
11. Uber Elevate. Uber Air Vehicle Requirements and Missions. Available online: <https://s3.amazonaws.com/uber-static/elevate/Summary+Mission+and+Requirements.pdf> (accessed on 22 August 2021).
12. Uber. Uber Elevate: Fast Forwarding to a Future of On-Demand Urban Air Transportation. 2016. Available online: <https://www.uber.com/elevate.pdf> (accessed on 22 August 2021).
13. Kasliwan, A.; Furbush, N.J.; Grawron, J.H.; McBride, J.R.; Wallington, T.J.; De Kleine, R.D.; Kim, H.C.; Keoleian, G.A. Role of flying cars in sustainable mobility. *Nat. Commun.* **2019**, *10*, 1555. [CrossRef]
14. Johnson, W.; Silva, C.; Solis, E. Concept Vehicles for VTOL Air Taxi Operations. In Proceedings of the AHS Technical Conference on Aeromechanics Design for Transformative Vertical Flight, San Francisco, CA, USA, 16–19 January 2018.
15. Garrow, L.A.; German, B.J.; Leonard, C.E. Urban air mobility: A comprehensive review and comparative analysis with autonomous and electric ground transportation for informing future research. *Transp. Res. Part C* **2021**, *132*, 103377. [CrossRef]
16. Mudumba, S.V.; Chao, H.; Maheshwari, A.; DeLaurentis, D.A.; Crossley, W.A. Modeling CO₂ Emissions from Trips using Urban Air Mobility and Emerging Automobile Technologies. *Transp. Res. Rec.* **2021**, *2675*, 1237–1244. [CrossRef]
17. Datta, A. *Commercial Intra-City On-Demand Electric-VTOL Working Report*; Vertical Flight Society: Fairfax, VA, USA, 2018.
18. Snyder, C.A.; Tong, M.T. Modeling Turboshift Engines for the Revolutionary Vertical Lift Technology Project. In Proceedings of the American Helicopter Society 75th Annual Forum, Philadelphia, PA, USA, 13–16 May 2019.
19. GE Turbines and Small Engines Overview. Available online: https://arpa-e.energy.gov/sites/default/files/14_deBock_GE%20Turbines%20and%20small%20engines%20overview%20-%20ARPA-e%20INTEGRATE%20V2.pdf (accessed on 3 November 2021).
20. Bérubé, D.; Dessaint, L.A.; Liscouet-Hanke, S.; Lavoie, C. Simulation of a hybrid emergency power system for more electric aircraft. *Can. Aeronaut. Space J.* **2011**, *57*, 155–162. [CrossRef]
21. Donato, T.; Spedicato, L. Fuel economy of hybrid electric flight. *Appl. Energy* **2017**, *206*, 723–738. [CrossRef]
22. Hill Helicopters Reveals New Turboshift Engine. Available online: <https://www.flyer.co.uk/hill-helicopters-reveals-new-turboshift-engine> (accessed on 22 August 2021).
23. Knight, H. Airbus and Siemens Investigate Hybrid-Electric Propulsion Systems for Low Emission Aviation. 18 April 2016. Available online: <https://www.theengineer.co.uk/airbus-and-siemens-investigate-hybrid-electric-propulsion-for-low-emission-aviation/> (accessed on 31 August 2021).
24. Lipol Battery. Available online: www.lipolbattery.com (accessed on 3 February 2017).
25. Cole, J.A.; Rajauski, L.; Loughran, A.; Karpowicz, A.; Salinger, S. Configuration Study of Electric Helicopters for Urban Air Mobility. *Aerospace* **2021**, *8*, 54. [CrossRef]
26. Guzzella, L.; Sciarretta, A. *Vehicle Propulsion Systems: Introduction to Modeling and Optimization*; Springer: Berlin, Germany, 2007.
27. Johnson, W.; Silva, C.; Solis, E. NASA concept vehicles and the engineering of advanced air mobility aircraft. *Aeronaut. J.* **2022**, *126*, 59–91. [CrossRef]
28. Park, Y.-K.; Moon, S.-W.; Kim, T.-S. Advanced Control to Improve the Ramp-Rate of a Gas Turbine: Optimization of Control Schedule. *Energies* **2021**, *14*, 8024. [CrossRef]
29. Donato, T.; Spada Chiodo, L.; Ficarella, A. Transient behavior of a hybrid electric air-taxi. In Proceedings of the International Symposium on Sustainable Aviation, Bangkok, Thailand, 25–27 November 2021.

30. Ballou, R.H.; Rahardja, H.; Sakai, N. Selected country circuitry factors for road travel distance estimation. *Trans. Res. Part A Policy Pract.* **2002**, *36*, 843–848. [[CrossRef](#)]
31. Donato, T.; Ficarella, A. Off-line and On-line Optimization of the Energy Management Strategy in a Hybrid Electric Helicopter for Urban Air-Mobility. *Aerosp. Sci. Technol.* **2021**, *113*, 106677. [[CrossRef](#)]
32. Donato, T.; Ficarella, A. A Modeling Approach for the Effect of Battery Aging on the Performance of a Hybrid Electric Rotorcraft for Urban Air-Mobility. *Aerospace* **2020**, *7*, 56. [[CrossRef](#)]
33. Hoke, A.; Brissette, A.; Maksimović, D.; Pratt, A.; Smith, K. Electric vehicle charge optimization including effects of lithium-ion battery degradation. In Proceedings of the 2011 IEEE Vehicle Power and Propulsion Conference, Chicago, IL, USA, 6–9 September 2011; pp. 1–8. [[CrossRef](#)]
34. Fares, R.L.; Webber, M.E. What are the tradeoffs between battery energy storage cycle life and calendar life in the energy arbitrage application? *J. Energy Storage* **2018**, *12*, 37–45. [[CrossRef](#)]
35. Millner, A. Modeling Lithium Ion battery degradation in electric vehicles. In Proceedings of the 2010 IEEE Conference on Innovative Technologies for an Efficient and Reliable Electricity Supply, Waltham, MA, USA, 27–29 September 2010; pp. 349–356. [[CrossRef](#)]
36. Li, J.; Gee, A.M.; Zhang, M.; Yuan, W. Analysis of battery lifetime extension in a SMES-battery hybrid energy storage system using a novel battery lifetime model. *Energy* **2015**, *86*, 175–185. [[CrossRef](#)]
37. Zeng, X.-H.; Wang, Q.; Wang, Q.-N. Simulation and analysis of THS II based on ADVISOR software. In Proceedings of the ICCASM 2010, International Conference on Computer Application and System Modeling, Taiyuan, China, 22–24 October 2010; Volume 5, pp. V5131–V5136. [[CrossRef](#)]
38. Fontanas, G.; Pistikopoulos, P.; Samaras, Z. Experimental evaluation of hybrid vehicle fuel economy and pollutant emissions over real-world simulation driving cycles. *Atmos. Environ.* **2008**, *42*, 4023–4035. [[CrossRef](#)]
39. Pitanuwat, S.; Sripakagorn, A. An Investigation of Fuel Economy Potential of Hybrid Vehicles under Real-World Driving Conditions in Bangkok. *Energy Procedia* **2015**, *79*, 1046–1053. [[CrossRef](#)]
40. Nissan Leaf Taxi. Available online: <https://www.greencarreports.com/news/nissan-leaf-taxi> (accessed on 27 October 2021).
41. Electric Vehicle Database. Available online: <https://ev-database.org/car/> (accessed on 27 October 2021).
42. Donato, T.; Ingrosso, F.; Bruno, D.; Laforgia, D. Effect of driving conditions and auxiliaries on mileage and CO₂ emissions of a gasoline and an electric city car. *SAE Tech. Pap.* **2014**, *1*, 1–13. [[CrossRef](#)]
43. Gan, L.; Topcu, U.; Low, S. Optimal decentralized protocol for electric vehicle charging. In Proceedings of the 2011 50th IEEE Conference on Decision and Control and European Control Conference (CDC-ECC), Orlando, FL, USA, 12–15 December 2011.
44. Thiel, C.; Schmidt, J.; Van Zyl, A.; Schmid, E. Cost and well-to-wheel implications of the vehicle fleet CO₂ emission regulation in the European Union. *Transp. Res. Part A* **2014**, *63*, 25–42. [[CrossRef](#)]
45. Donato, T.; Ingrosso, F.; Licci, F.; Laforgia, D. A method to Estimate the Environmental Impact of an Electric City Car during Six Months of Testing in an Italian City. *J. Power Sources* **2014**, *270*, 487–498. [[CrossRef](#)]
46. Ang, B.W.; Su, B. Carbon emission intensity in electricity production: A global analysis. *Energy Policy* **2016**, *94*, 56–63. [[CrossRef](#)]
47. Cerdeira Bento, J.P.; Moutinho, V. CO₂ emissions, non-renewable and renewable electricity production, economic growth, and international trade in Italy. *Renew. Sustain. Energy Rev.* **2016**, *55*, 142–155. [[CrossRef](#)]
48. European Environment Agency. Available online: <https://www.eea.europa.eu/> (accessed on 23 August 2021).
49. Donato, T.; Ficarella, A.; Surdo, L. Energy consumption and environmental impact of Urban Air Mobility. In Proceedings of the 11th Easn Virtual International Conference on Innovation in Aviation & Space to the Satisfaction of the European Citizens, Salerno, Italy, 1–3 September 2021.

Article

Adaptive Driving Cycles of EVs for Reducing Energy Consumption

Iwona Komorska ^{1,*}, Andrzej Puchalski ¹, Andrzej Niewczas ², Marcin Ślęzak ² and Tomasz Szczepański ²

¹ Department of Mechanical Engineering, Kazimierz Pulaski University of Technology and Humanities in Radom, Malczewskiego 29, 26-600 Radom, Poland; andrzej.puchalski@uthrad.pl

² Motor Transport Institute, Jagiellońska 80, 03-301 Warszawa, Poland; andrzej.niewczas@its.waw.pl (A.N.); marcin.slezak@its.waw.pl (M.Ś.); tomasz.szczepanski@its.waw.pl (T.S.)

* Correspondence: iwona.komorska@uthrad.pl

Abstract: A driving cycle is a time series of a vehicle's speed, reflecting its movement in real road conditions. In addition to certification and comparative research, driving cycles are used in the virtual design of drive systems and embedded control algorithms, traffic management and intelligent road transport (traffic engineering). This study aimed to develop an adaptive driving cycle for a known route to optimize the energy consumption of an electric vehicle and improve the driving range. A novel distance-based adaptive driving cycle method was developed. The proposed algorithm uses the segmentation and iterative synthesis procedures of Markov chains. Energy consumption during driving is monitored on an ongoing basis using Gaussian process regression, and speed and acceleration are corrected adaptively to maintain the planned energy consumption. This paper presents the results of studies of simulated driving cycles and the performance of the algorithm when applied to the real recorded driving cycles of an electric vehicle.

Keywords: electric vehicle; driving cycle; energy consumption; Markov chains; driving range

Citation: Komorska, I.; Puchalski, A.; Niewczas, A.; Ślęzak, M.; Szczepański, T. Adaptive Driving Cycles of EVs for Reducing Energy Consumption. *Energies* 2021, 14, 2592. <https://doi.org/10.3390/en14092592>

Academic Editor: Laura Tribioli

Received: 22 March 2021

Accepted: 27 April 2021

Published: 1 May 2021

Publisher's Note: MDPI stays neutral with regard to jurisdictional claims in published maps and institutional affiliations.



Copyright: © 2021 by the authors. Licensee MDPI, Basel, Switzerland. This article is an open access article distributed under the terms and conditions of the Creative Commons Attribution (CC BY) license (<https://creativecommons.org/licenses/by/4.0/>).

1. Introduction

The popularization of electric vehicles may decrease air pollution, particularly in cities. The more fossil-fuel-burning vehicles are replaced with electric vehicles, the less harmful substances (pollutants in particulate matter and gases, mainly nitrogen oxides and sulfur oxides) are released into the air. This is the most significant benefit of electromobility from the perspective of environmental impact. It will also reduce the emissions of greenhouse gases (particularly carbon dioxide and ozone). For vehicle owners, the primary advantage is significantly lower operating costs compared to those of conventional vehicles. An energy management system is critical for the development of electric vehicles because it directly affects their capacity to save energy. Power management aims to create the optimum policy for controlling power supplied to the vehicle. The applied driving cycle is required to optimize and assess power management in electric vehicles.

Predicting the driving cycle of a vehicle is becoming increasingly important in modern intelligent transport, particularly for controlling energy consumption in electric vehicles, planning the trajectory of autonomous terrestrial vehicles, energy management in hybrid electric vehicles, etc. In general, driving cycles illustrate changes in vehicle speed as a function of time. They are of fundamental importance to vehicle engineering. Originally, the primary application of driving cycles was to identify the performance characteristics of a vehicle, such as exhaust emissions and fuel consumption for cars with an internal combustion engine. Along with the development of HEVs, PHEVs and EVs, many studies have addressed the adaptation of driving cycles to these types of vehicles [1–6].

Driving cycles should reflect actual road conditions as well as local conditions in a particular country or region. Driving cycles with equivalent properties can be generated only using a dataset with recorded information about a vehicle or fleet operation as the

basis for generating time signals and final assessment of the quality of induced cycles. Many properties of the driving profile characterizing local driving cycles, such as the average, maximum and minimum values and standard deviations of speed, acceleration and delay, have been defined in the listed articles [1,3,7–12]. The impact of the velocity profile on energy consumption in EVs is analyzed in [13].

There are various methods for generating driving cycles, and they are still being developed. In general, however, three primary approaches can be identified: segmentation, Markov chain method and mixed method (a combination of the first two methods). Each method requires a sufficiently large dataset. The cycle is divided into microtrips in the segmentation method, defined as the speed trace between two successive stops [10] or as sections of the route grouped according to specific criteria, such as different road types, traffic conditions or speed limits. Segments are combined stochastically to generate new driving cycles.

The Markov chain method represents another mathematical approach to driving cycle generation. In the simplest algorithm, speeds are divided into classes, and the probability of transition from class to class is included in the TPM. Then, the TPM and speed probability distribution are used to generate new driving cycles. Their equivalence to the reference cycle is verified based on specific criteria [14–23].

The mixed method combines the two methods mentioned above so that the segment classes (e.g., cruising, idling, acceleration, deceleration or other defined classes) are selected according to the Markov chain algorithm [1,6,24,25]. The methods used for generating driving cycles in this study are discussed more specifically in Section 2.

Previous studies on driving cycles were used to synthesize the type of drive and the city region's test cycle characteristic. The new approach proposed in this article consists of modifying the driving cycle during its duration to the driving range extension based on well-known Markov process models. Here, energy consumption is estimated based on a statistical model (machine learning method), which is easily determined for each vehicle based on an exemplary driving profile. We go a step further by proposing a modification of the velocity profile during its duration using the new DBADC (distance-based adaptive driving cycle) method. The purpose of this study is to predict the driving cycle and correct it on an ongoing basis depending on road conditions and the vehicle energy consumption. Because of this purpose, driving cycles will be considered as distance-based velocity and not as time-based velocity, as is usually the case. The transition probability matrix (TPM) will be corrected on an ongoing basis during driving, not exceeding the energy-use boundary of a particular route. This method is dedicated to electric vehicles with autopilot feature and driven on specific routes, such as cars rented for a short time in the form of car-sharing and delivery vehicles, buses, etc.

2. Methods

This study uses the segmentation method and iterative Markov chains. Figure 1 shows an illustration of the method, referred to as distance-based adaptive driving cycle (DBADC), which consists of the following components: data collection and their synchronization based on distance, route segmentation and determination of the TPM for the segments, generation of a representative driving cycle and estimated energy consumption using Gaussian process regression (GPR; model-based energy calculation), and on-line correction of the current cycle (an adaptation of the current driving cycle).

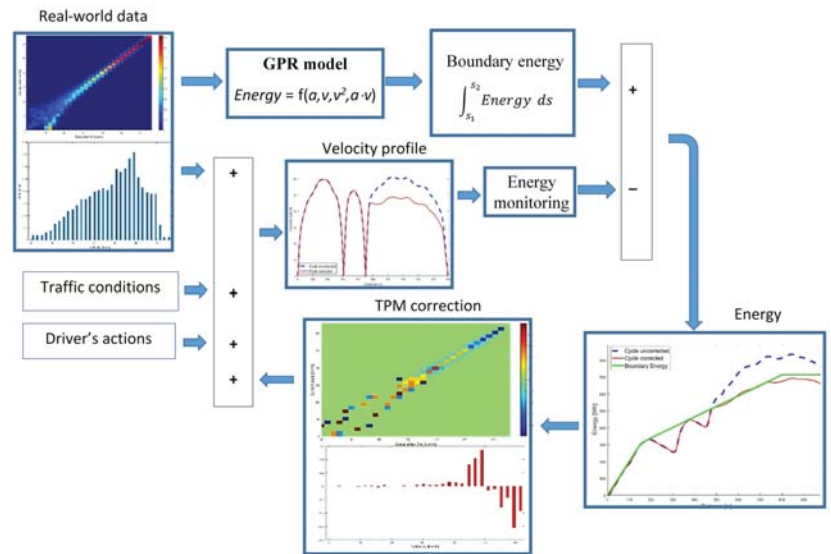


Figure 1. Illustration of the DBADC method.

First, it is necessary to collect a dataset of driving cycles on routes in the particular region or on planned routes and associated instantaneous or average electricity consumption during these driving cycles.

2.1. Cycle Segmentation

A typical microtrip in a driving cycle is presented by Austin et al. [26] as the speed trace between two stops. The cycle begins with the idling phase, followed by the acceleration, cruise and deceleration phases. The entire driving cycle consists of such microtrips. The duration of the driving cycle varies depending on average speed and acceleration. Austin et al. suggest three methods for combining microtrips: random, best incremental (based on the Watson plot) and hybrid. The set of driving cycle candidates thus generated is used to select the driving cycle for which the probability distribution of acceleration and speed most closely resembles the actual driving dataset. Further versions of this method are based on improved methods for stochastically combining microtrips. Determination of the optimum combination of microtrips using a genetic algorithm (GA) is proposed in [10]. In this, segments with differing numbers of microtrips are combined until the desired driving cycle duration is reached. In [27], Nesamani et al. used microtrips based on road type to develop a driving cycle for PHEV city buses. A computer program was devised to select microtrips at random until the target distance was reached. The percentage of microtrips depending on road type and time spent on every road type was also calculated to further represent the observed data. In [6], kinematic segments were divided depending on the distance between successive bus stops, whereas the two-dimensional Monte Carlo Markov chain (MCMC) method was used to synthesize driving cycles between each interval of subsequent bus stops.

In the segmentation method, real driving cycles are divided into driving segments grouped according to similar average speed, road surface, traffic conditions or other criteria. The segments are connected stochastically. Lin and Niemeier [24] used the acceleration signal and the maximum likelihood estimation (MLE) method to divide the cycle into segments to associate the segment with specific modal operating conditions (e.g., cruise control, idling, acceleration or deceleration). Here, every class characterizes the driving style and, consequently, also represents a possible state in the Markov chain. Zähringer et al. [28] present the enhanced modal cycle construction (EMCC) method, which is a

modification of the method described in [24]. Here, the global driving state acceleration, deceleration and cruising are subdivided into substates. This enables development of a complete driving cycle using a first-order Markov chain with a constant transition matrix. The control segments to be combined are constructed parametrically based on characteristic values.

This paper proposes dividing a route into segments. Depending on the type of vehicle, segments range from one to several microtrips, which do not have to begin or end with the idling phase. For instance, for cars or delivery vehicles, the segment may include the route between intersections or longer, even though the idling phase may be absent when passing through an intersection. For a bus, the segments may include the route from one stop to another, with traffic lights on the way and a segment beginning and ending with the idling phase.

Figure 2 shows a sample segment of a driving cycle, recorded between traffic lights and covering a distance of approximately 700 m, frequently driven in heavy, congested traffic.

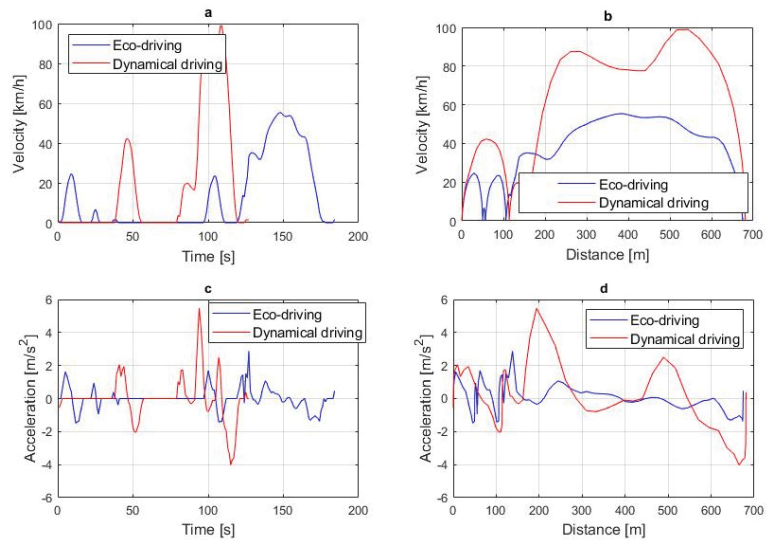


Figure 2. A sample segment (a) velocity vs. time, (b) velocity vs. distance, (c) acceleration vs. time, (d) acceleration vs. distance.

The two sample segments between traffic lights shown in Figure 2 have different maximum speeds, accelerations and travel times. This makes it difficult to compare them in the time domain (Figure 2a,c). However, cycles analyzed in the distance domain (Figure 2b,d) are more transparent. Because driving cycles are recorded at equal time intervals, it is necessary to use a cycle synchronization procedure based on travel distance.

The length of the segment is selected individually depending on the route and the type of vehicle. A single microtrip between traffic lights is shown in Figure 2. However, the segments should contain more microtrips, grouped according to road conditions such as driving on the ring road, route with heavy traffic (city center) and a built-up zone (residential). This allows for more effective cycle correction.

When the segments are analyzed in the distance domain, the idling phase is hidden. However, idling in electric vehicles affects only energy consumption unrelated to driving, used to power HVAC (heating, ventilation and air-conditioning) systems, radio or lights. Energy consumed during the idling phase can be statistically considered in each segment, if necessary. In this study, the idling phase was omitted from the development of the driving cycle. However, the energy consumption during this phase was statistically included.

When driving cycles are analyzed in the distance domain, known cycle lengths based on the planned route can be used to synthesize Markov chains.

2.2. Markov Chain Method

A Markov chain is the process wherein computation of the random variable future value is based on the current value, irrespective of the previous value. In mathematical terms, the random process $X = \{X_1, X_2, X_3, \dots\}$ in the discrete space of states E is the first-order Markov chain; if for each $j \in E$ and $n = 0, 1, 2, \dots$ the conditional distribution X_{n+1} is a function of the X_n variable only [15]:

$$\Pr\{X_{n+1} = j | X_0 = i_0, X_1 = i_1, \dots, X_n = i_n\} = \Pr\{X_{n+1} = j | X_n = i_n\}, \quad (1)$$

for each set of states i_0, i_1, \dots, i_n .

Suppose a Markov chain is stationary, with probabilities not changing depending on time. In that case, the distribution of probabilities of transitions between particular k -states can be presented as a matrix called the transition probability matrix (TPM) $P \in R^{k \times k}$. This is a stochastic matrix:

$$P = \begin{bmatrix} P_{11} & \cdots & P_{1k} \\ \vdots & \ddots & \vdots \\ P_{k1} & \cdots & P_{kk} \end{bmatrix} \quad (2)$$

The elements of the P matrix P_{ij} can be calculated using the following equation:

$$P_{ij} = \frac{N_{ij}}{\sum_j N_{ij}} \quad (3)$$

where P_{ij} is equal to the probability of transition from state i to state j , when $j \neq i$ or remains in state i , when $j = i$. N_{ij} is the number of transitions from state i and to state j . All entries of this matrix $P_{ij} \geq 0$, and the sum of the values of entries in each row, i.e., probabilities of remaining or leaving a given state, is equal to one.

Over the last decade, the Markov chain method has been used in an ongoing effort to improve driving cycles. Stochastic and statistical methods were combined by Lee and Filipi in [16]. They proposed a procedure for synthesizing real driving cycles to model naturalistic driving patterns for any distance. In [17], Gong et al. collected a large dataset of speed measurements for PHEV. The speed profiles were grouped into classes. Driving patterns were identified based on the grouping results, and the Markov chain model was used for the stochastic generation of speeds for different driving patterns. Souffran et al. [18] proposed a stochastic model of driving cycles based on a Markov matrix of three variables—vehicle speed, acceleration and road slope—representing real driving conditions. In [6], Liu et al. considered speed, road slope and passenger load for a real bus route with a plug-in hybrid electric bus (PHEB). Kinematic segments were divided according to the distance between successive bus stops, whereas the two-dimensional MCMC method was used to synthesize the driving cycle between each interval of successive bus stops. A transition based on multidimensional Markov chains is presented by Silvas et al. in [19]. After the generation process, the result was verified according to the selected criteria. Moreover, this method can generate a driving cycle of the desired length by compressing the original driving cycle. Nyberg et al. [14] defined the mean tractive force (MTF) to verify equivalent driving cycles. When the individual components of MTF are used to generate driving cycles using Markov chains, equivalent driving cycles can be generated, sharing the same vehicle power usage based on real driving data. In [20], Zhao et al. synthesized a stochastic driving cycle based on their model. They combined the Markov chain process with the transition probability based on driving data input to determine the next possible state of the vehicle. In particular, speed and road slope were generated at the same time using a three-dimensional Markov chain model. After the generation process, the result was verified according to selected criteria. Puchalski et al. [21] used a multifractal criterion to verify the

equivalence of driving cycles. Shi et al. [22] provided validation of the Markov property of the driving cycle. They used the theory of ergodicity to determine the relationship between speed and acceleration probability and the state transition matrix.

In the approach presented in this paper, the vehicle speed change process is regarded as a discrete Markov chain. During autonomous or partially autonomous driving, the driving cycle is determined step by step, as in a Markov chain. The next state $v(i+1)$ depends on the previous state $v(i)$ and disruption caused by road conditions.

Markov chains are efficient when the length is known in advance. Obviously, the longer the chain, the easier it is to achieve a given probability distribution. In the presented literature, Markov chains were used to represent a travel cycle with given duration. As the segment travel time is unknown and the distance is known, this article proposes a modification of the TPM. Transitions from one state to another take place in the distance domain, not the time domain.

2.3. Data-Driven Model of Energy Calculation

A mathematical model is needed to estimate electricity consumption. A backward model is generally used to compute the energy consumption of the vehicle from travel. Electric vehicle energy models are described in [10,13,29,30]. For this study, it was necessary to determine the relationship between the driving cycle parameters (speed and acceleration) and electric energy. We decided to use the statistical model developed with the machine learning method.

Regardless of the parameters of the vehicle, assuming a constant friction coefficient, it can be further assumed that instantaneous energy is a function of the kinematic variables of the vehicle and the slope of the road:

$$E = f[a(t), v(t), v(t)^2, a(t) \cdot v(t), slope] \quad (4)$$

where $v(t)$ is velocity and $a(t)$ is acceleration of the vehicle.

Machine learning methods were used to identify the function representing the kinematic variables of the vehicle.

Taking into account energy recovered from braking, energy consumption is integrated both in the tracking and braking phases:

$$E = \int_t P_v dt \quad (5)$$

Average energy consumption \bar{E} is defined as:

$$\bar{E} = \frac{E}{s} \quad (6)$$

where s is the mileage.

There are many ways of modelling continuous signals using experimentally derived datasets. The most frequent method is linear regression, where the set of estimating functions is limited to linear forms, and the values of the parameters are inferred using the least-squares method. Other polynomial, logarithmic, exponential or logistic functions and other loss functions different from the sum of the squares of deviations of real values relative to the theoretical values are also used. An equally popular method is to estimate the signals' parameters by determining the maximum likelihood that a specific sample will occur (MLE). This method can be used to analyze nonlinear signals represented even by short time series, and the estimators thus obtained are asymptotically unbiased.

The Gaussian process regression (GPR) method was used in the study [31] to estimate the system's response, represented by current energy consumption, to input in the form of speed and acceleration measurement signals.

The vectors created from the signal input measurement and the signal output were adopted due to a random experiment, which means that the probability density function for their distribution includes complete information about their values.

When constructing a regression model, we assumed that the expected observed value y can be written as a specific monotonic linear transformation of a combination of independent variables corresponding to the model parameters $\theta = \theta_1, \theta_2, \dots, \theta_k$. This means that it is possible to determine the likelihood $f(y|\theta)$, which is a function of parameter θ .

In the maximum likelihood estimation method, the values of the estimated parameters are selected to maximize the likelihood function. In practice, this task requires solving the analytically equivalent problem of maximizing the logarithm $\ln f(y|\theta)$. Using Bayesian inference in estimating the discussed regression model requires determining the posterior probability $f(\theta|y)$ of parameter θ under the condition of observation y . The posterior distribution density function of the parameters is obtained from the Bayesian formula:

$$f(\Theta/y) = \frac{f(y/\Theta)f(\Theta)}{f(y)} \quad (7)$$

where $f(\Theta)$ is the prior probability of the parameters, and $f(y)$ is the factor normalizing the posterior probability—independent of Θ —the so-called global likelihood or evidence.

Maximum a posteriori estimation (MAP) can take into account both the past probability and earlier data concerning the event. The confidence intervals can also be interpreted more intuitively.

For a more accurate model, the cycles were divided into three parts: tractive phase, regenerative braking and idle phase. The energy consumption/recovery model in each phase was considered separately. The model identification result is expressed by one of the errors, e.g., RMSE (root mean squared error) or the R2 coefficient for the predicted response vs. true response dependence. The results of model identification using the GPR method for the real object, as well as the quality of this mapping, are discussed in Section 3.2.

2.4. Adaptation of the Current Driving Cycle

The dataset of driving cycles collected on the investigated route is used to determine representative driving cycles to estimate average electricity consumption. It is not the purpose of this study to develop driving cycles representative for the region; rather, the study aims to select adaptive driving cycles that can be used to optimize electricity consumption.

This entails the necessity of defining the values of typical driving cycles. Twenty-seven variables describing the driving cycle were summarized in [3]. The following parameters characterizing the segments of the cycle were selected for the purposes of this study (Table 1).

In the set of monitored parameters, va was introduced, which is the speed and acceleration product. It is one of the inputs in the data-driven energy calculation model and significantly impacts energy consumption. The main component of the tractive force is the inertial force of the vehicle ($ma(t)$), and the mechanical power is the product of force and speed. Therefore, the product of speed and acceleration (va) is a significant component of the model.

Boundary energy values are determined individually for each segment of the route. These parameters can be used to select energy-efficient cycles or cycles with average electricity consumption. They may be averaged values for a typical driving cycle on a particular route, values depending on the battery capacity, etc.

The boundary energy course is determined based on averaged energy consumption courses for a given vehicle and route. It means the total electricity consumption from the beginning of the segment to which the actual energy consumption of the car should aim. It consists of three phases: acceleration, cruising and braking. It is assumed that energy consumption increases linearly in the cruising phase, but in reality, this is not the case. Multiple microtrips can take place during this time. However, energy consumption should be around the assumed limit. In the last phase, braking, zero consumption is assumed, although energy is recovered. This makes it possible to make up for any energy losses in

the segment without additional cycle corrections. The limit of energy consumption may be additionally limited due to the driving range caused by the battery capacity, distance from the charging station, etc.

Table 1. The calculated parameters in driving cycles.

Number	Parameter
1	Average speed
2	Average speed (only cruising)
3	Standard deviation of speed
4	Maximum acceleration
5	Average acceleration
6	Standard deviation of acceleration
7	Maximum deceleration
8	Average deceleration
9	Standard deviation of deceleration
10	% of time when idling
11	% of time when speed is 0–15 (km·h ⁻¹)
12	% of time when speed is 15–30 (km·h ⁻¹)
13	% of time when speed is 30–50 (km·h ⁻¹)
14	% of time when speed is >50 (km·h ⁻¹)
15	% of time when va^1 is <0 (m ² ·s ⁻³)
16	% of time when va is 0–3 (m ² ·s ⁻³)
17	% of time when va is 3–6 (m ² ·s ⁻³)
18	% of time when va is 6–10 (m ² ·s ⁻³)
19	% of time when va is >10 (m ² ·s ⁻³)
20	Total duration
21	Time of cruising without idling
22	Average energy consumption

¹ va is the product of vehicle velocity and acceleration.

The adaptive method involves the continuous monitoring of average energy consumption in each segment of the cycle, comparing this consumption with the boundary energy in a particular segment and appropriate correction of speed and acceleration. If energy consumption in a given segment exceeds the boundary energy, the vehicle speed is corrected. A 1000 m driving segment was simulated to illustrate the applied DBADC method. The algorithm plot is shown in Figure 3.

The red line in Figure 3b refers to the boundary energy, which triggers a correction of vehicle speed if it is exceeded. Due to road conditions during the cycle, the vehicle accelerated three times and braked three times, and it was only during the third acceleration that the boundary energy was exceeded. During speed correction, energy oscillated around the boundary energy, only to fall below the boundary energy at the end of the microtrip due to energy recovery during braking. If the correction had been insufficient, the next correction would have reduced the vehicle speed and acceleration.

3. Results

3.1. Experiment Description

Road tests were performed by the Motor Transport Institute in cooperation with Tesla Warsaw. The Tesla Model X vehicle with 90D drive was used for the tests presented in this article. The vehicle had three electric motors with a total 540 HP, driving both axles. The battery had a capacity of 90 kWh and a maximum power of 350 kW. The unladen mass of the vehicle was 2475 kg. The vehicle also had a second-generation autopilot, software version 9.0 (partially autonomous driving), which was used in the tests. The route included city traffic in the very center of Warsaw. The streets formed a closed loop with a shape resembling a square, with a total travel distance of approximately 6.5 km. The altitude was 137 m, varying within a range of +/− 6 m. Road slope did not exceed 1°, which means that the area was relatively flat. A map with the travel route is shown in Figure 4.

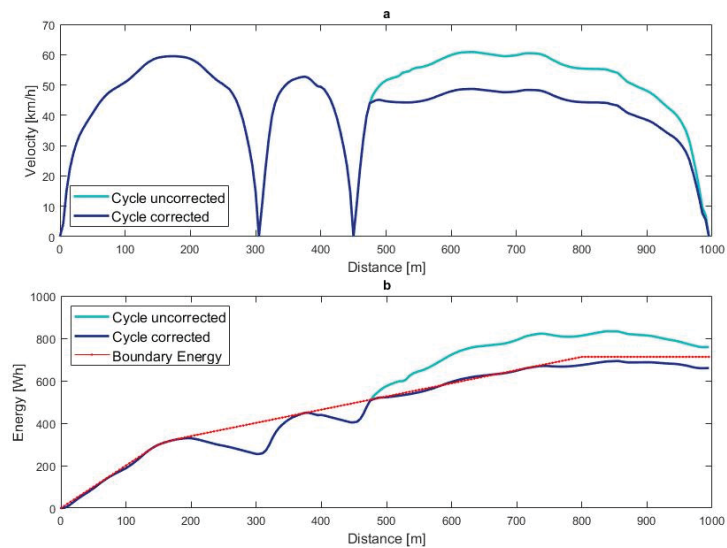


Figure 3. Simulation of a sample driving cycle (a) and energy consumption (b) during a cycle with and without correction.

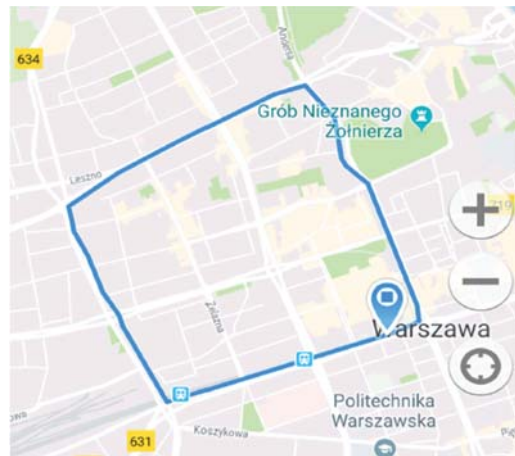


Figure 4. Travel route.

The tests were conducted in February on working days from 2:00 p.m. to 5:00 p.m., i.e., when traffic in the area was fairly heavy. The duration of a single cycle ranged from 15 to 22 min. The weather conditions during the test cycles varied only to a small extent because testing days were chosen to meet specific conditions, namely temperature between 8 and 13 °C, pressure between 970 and 995 hPa, humidity between 30 and 50%, wind speed of 10 km/h or less, no rain and dry pavement. Interior heating was on during the tests, with the temperature set at a constant 22 °C. Exterior lighting and the main screen, which was used to track the vehicle with a GPS and show messages from the onboard computer, were also turned on. The remaining devices were off. Battery charge status before each test was no less than 50% and no more than 80%. The vehicle was driven by two test drivers, each of whom represented two driving styles: calm and dynamic. The autopilot feature was used as well, and it drove the vehicle for at least 67% of the travel time. During the remaining

time, the test drivers controlled the vehicle themselves, driving calmly. The cycles during which the autopilot drove the vehicle were treated in the statistical calculations as if a third, independent driver was driving, although this driver was not able to change the driving style from calm to dynamic.

Figure 5a shows travel speeds as a function of time, and Figure 5b shows travel speeds as a function of travel distance. The figures show a comparison of cycles driven by the dynamic driver, the calm driver and the autopilot.

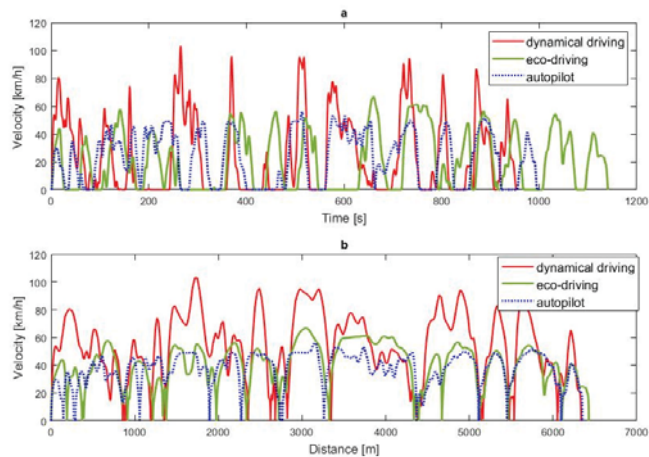


Figure 5. Recorded driving cycles (a) as a function of time, (b) as a function of travel distance for dynamic driving, eco-driving and autopilot.

Natural segments of the route separated by traffic lights can be easily distinguished in Figure 5b. It is possible to compare the speeds of the drivers in individual segments. Places with slower traffic are easy to identify.

Further analysis was carried out for speeds as a function of distance. The travel distance may differ in real segments by several or several dozen meters due to differences in lane lengths.

3.2. Energy Consumption

The recorded cycles were used to determine a statistical model of energy consumption using Gaussian process regression (GPR) depending on vehicle speed and acceleration. Figure 6 shows model verification results on the same route with a 95% prediction interval, a fragment of which has been magnified in Figure 6b, with the fit of the model shown in Figure 6c. The R^2 coefficient for the predicted response vs. true response dependence (Figure 6c) was close to 1.

The energy consumption of the HVAC during the test was 1.074 kW.

The GPR model can be used to monitor electricity consumption during any driving cycle. To analyze the impact of speed and acceleration on electricity demand, four 1 km segments of driving cycles were simulated (Figure 7a). Figure 7b shows the energy consumption for the simulated cycles, which increased together with distance travelled.

The highest energy consumption corresponded to cycle 1 due to the highest vehicle speed. Cycle 3 showed a quick initial increase in energy consumption due to high acceleration, yet lower overall consumption in the microtrip because the average speed was lower than in cycle 1. Alternate braking and acceleration did not significantly impact the total energy used during the microtrip. During cycle 2, in which speed and accelerations were reduced to approximately 80% of those in cycle 1, energy consumption was approximately 73% of that in cycle 1. Cycle 4, which simulated driving in congested traffic, showed that such driving was very energy-efficient, although it excessively prolonged travel time.

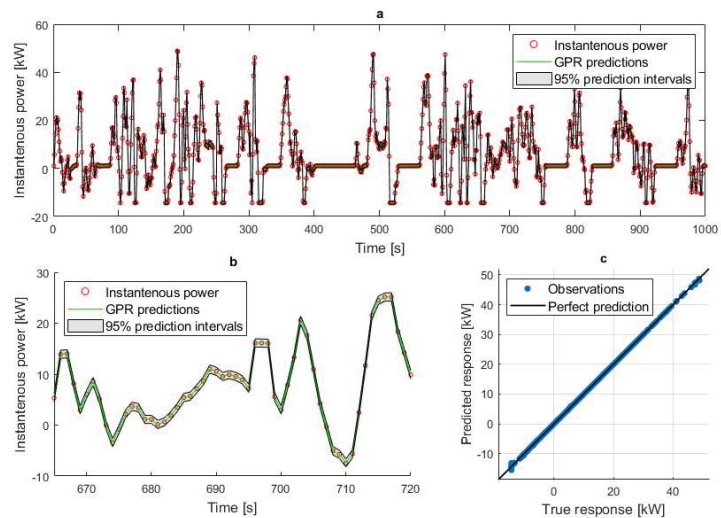


Figure 6. Verification of the GPR model: (a) the predicted responses and 95% prediction intervals using the fitted model, (b) zoom, (c) predicted vs. true response.

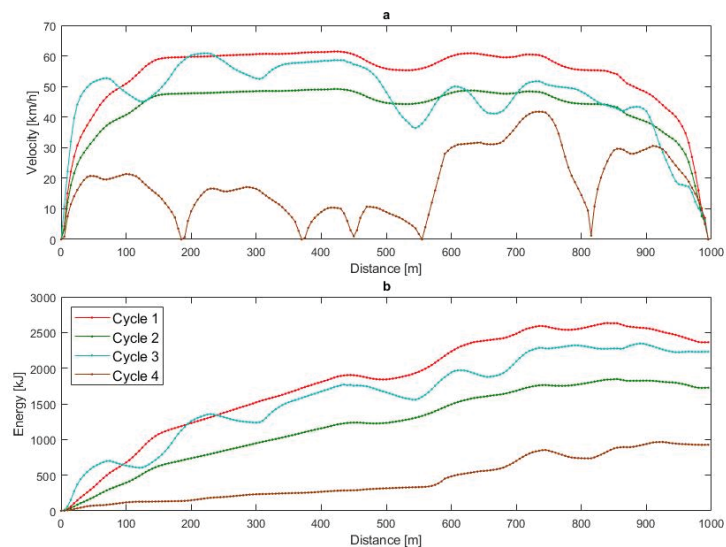


Figure 7. Simulated segments of the driving cycle as a function of distance (a) and corresponding energy consumption (b).

3.3. Representative Driving Cycle

The characteristic parameters specified in Table 1 were determined for the cycles described in Section 3.1 and averaged for dynamic driving, calm driving and autopilot driving. The results are presented in Table 2. Due to the small number of recorded cycles, they cannot be regarded as representative of local driving and only illustrate the method.

Table 2. Driving cycle parameters.

No.	Parameter	Dynamical Driving	Eco-Driving	Autopilot
1	Average speed	22.90	19.86	19.06
2	Average speed (only cruising)	35.15	29.03	28.84
3	Standard deviation of speed	25.45	19.38	19.32
4	Maximum acceleration	5.69	2.43	2.20
5	Average acceleration	1.18	0.62	0.62
6	Standard deviation of acceleration	0.47	0.48	0.47
7	Maximum deceleration	-4.22	-2.61	-3.12
8	Average deceleration	-0.95	-0.63	-0.67
9	Standard deviation of deceleration	0.74	0.47	0.55
10	% of time when idling	36.7	33.3	35.9
11	% of time when speed is 0–15 (km·h ⁻¹)	13.5	15.1	14.9
12	% of time when speed is 15–30 (km·h ⁻¹)	15.2	18.3	17.4
13	% of time when speed is 30–50 (km·h ⁻¹)	17.0	24.8	24.8
14	% of time when speed is >50 (km·h ⁻¹)	17.6	8.5	7.0
15	% of time when va1 is <0 (m ² ·s ⁻³)	33.6	31.8	29.1
16	% of time when va is 0–3 (m ² ·s ⁻³)	8.5	15.1	14.7
17	% of time when va is 3–6 (m ² ·s ⁻³)	5.7	9.9	9.1
18	% of time when va is 6–10 (m ² ·s ⁻³)	4.1	5.7	5.8
19	% of time when va is >10 (m ² ·s ⁻³ v)	10.9	3.2	3.8
20	Total duration (s)	999.3	1147.2	1214.0
21	Time of cruising without idling (s)	648.8	780.5	789.0
22	Average energy consumption (Wh·km ⁻¹)	427.6	260.7	309.4

Parameters 10–14 are shown in Figure 8a, and parameters 15–19 are shown in Figure 8b.

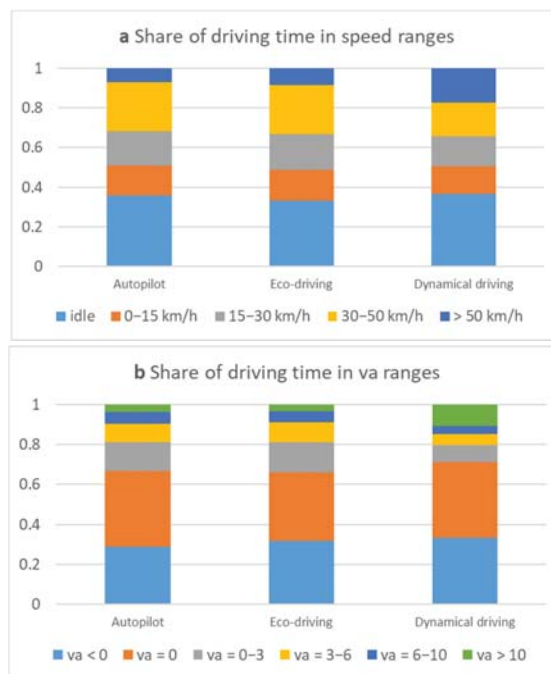


Figure 8. Comparison of driving cycle parameters for autopilot, eco-driving and dynamical driving: (a) percentage of time in speed ranges, (b) percentage of time in va ranges.

The driving profiles for autopilot and eco-driving were similar. However, the autopilot was found to have a slightly higher v_a , which resulted in higher energy consumption. Dynamic driving displayed a noticeable increase in the share of speeds over $50 \text{ km}\cdot\text{h}^{-1}$ and an increase of $v_a > 10 \text{ [m}^2\cdot\text{s}^{-3}\text{]}$, which resulted in a significant increase in average energy consumption and cruising time (Figure 9).

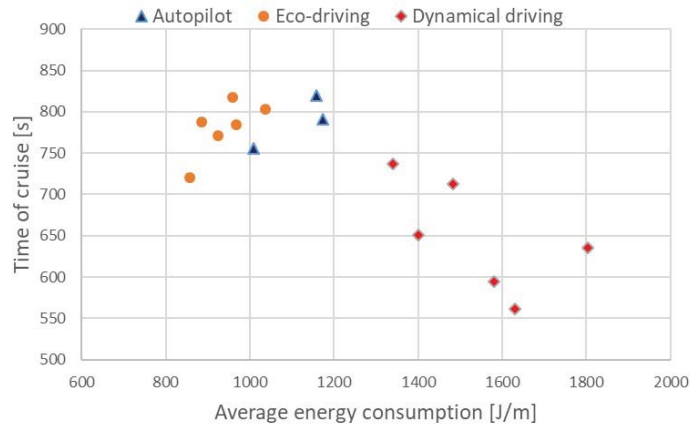


Figure 9. Cruising time (without idling) vs. average energy consumption.

As noted above, the lowest consumption was recorded for eco-driving, slightly higher for autopilot and the highest for dynamic driving, which had the broadest distribution. Travel times for eco-driving and autopilot were comparable; they were shorter for dynamic driving, although they too were characterized by significant breadth of distribution.

The recorded cycles were used to determine the speed acceleration probability density (SAPD) for the entire route, taking into account only the eco-driving and autopilot phases (Figure 10).

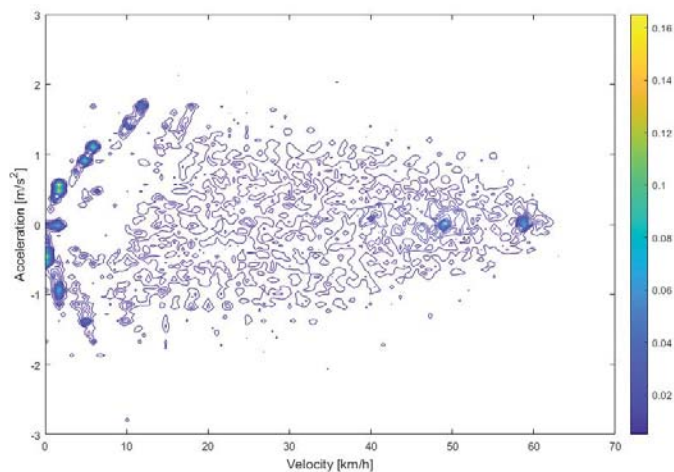


Figure 10. SAPD for investigated driving cycle.

The average distributions of vehicle speeds (Figure 11) and TPM (Figure 12) were also recorded. The resolution of vehicle speeds was found to be 2.0875 km/h .

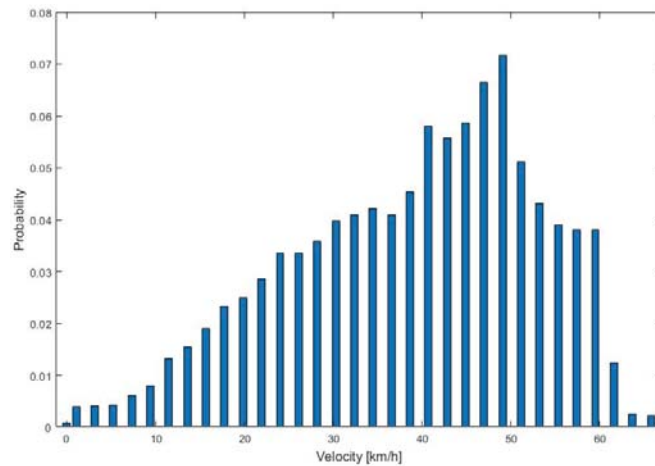


Figure 11. Average histogram of vehicle speeds on the tested route.

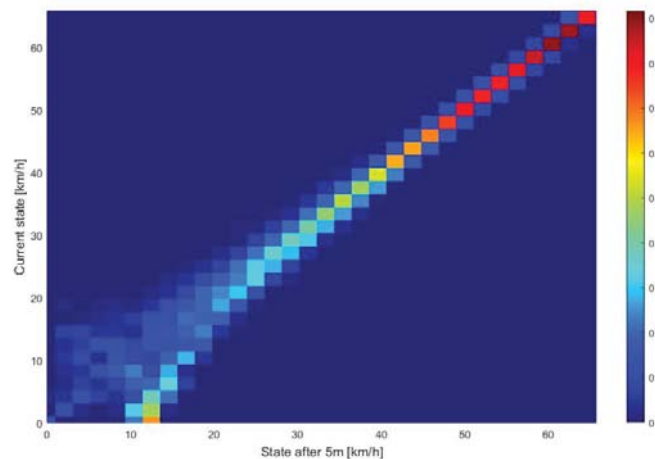


Figure 12. Average probability transition matrix for driving cycles on the route investigated.

After the route was divided into segments consisting of groups of microtrips or grouped according to traffic volume, speed limit etc., the TPM was determined for each segment and boundary energy.

3.4. Simulation Results

This method is dedicated to autonomous vehicles or vehicles with an autopilot feature (driving in semiautonomous mode). The test route was divided into four segments. The TPM was used to generate the next state that determines speed and acceleration. This state can be interrupted at any time by road conditions and traffic. Thus, the TPM is corrected on an ongoing basis, assuming that microtrips between traffic lights are driven at the speed limit and acceleration is additionally limited by energy consumption.

The division into segments was made to illustrate the functioning of the algorithm. For a longer route, a single segment could be used due to the road conditions. The application of the method for a sample driving cycle is shown in Figure 13. The energy boundary was determined based on average energy consumption during the driving cycles by the eco-driver. The corrected cycle was determined by simulation. Figure 13a shows the

uncorrected distance-based driving cycle (blue dashed line) for driving with the autopilot and a cycle corrected by the algorithm (red line). In Figure 13b, the energy boundary for each of the four segments and energy consumption during driving (from the beginning of the segment) are added for the corrected and uncorrected cycle.

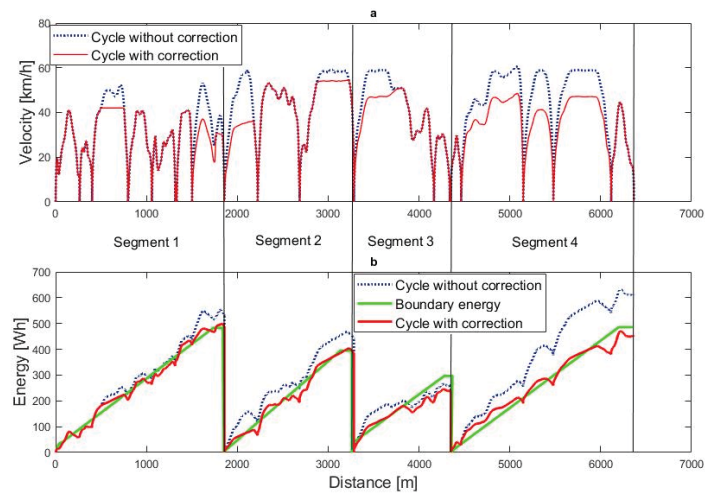


Figure 13. Illustration of the method using the investigated driving cycle: (a) distance-based driving cycle, (b) electricity consumption at successive route segments.

Figure 14 shows the corrected and uncorrected cycle as a function of time.

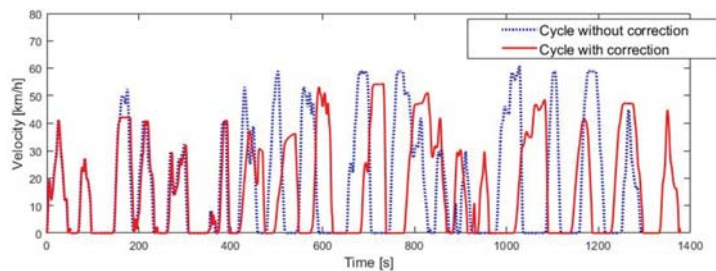


Figure 14. Time-based driving cycles for Figure 13a.

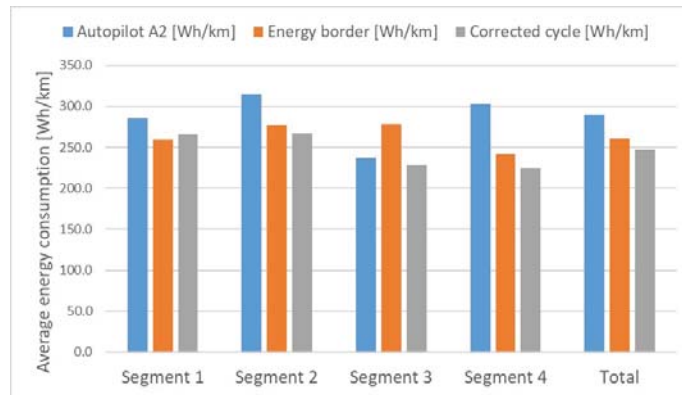
Table 3 shows average energy consumption during each driving segment and for the entire cycle. Reduced speed and acceleration results in approximately 15% reduction of energy consumption, albeit an 82 s (approximately 10%) extension of travel time (without idling).

Data from Table 3 are shown in the chart below (Figure 15).

Electricity consumption should oscillate around the boundary energy because braking at the end of each segment provides an opportunity to recover some of the energy expended. In the first segment, the vehicle speed is corrected, but if energy consumption at the end of the segment exceeds the boundary energy—as is the case in the first segment—the next (second) segment begins with a correction of speed and acceleration. The correction is made only with accelerations because decelerations result in energy recovery. The correction is implemented only until energy consumption drops below the boundary energy. In the fourth segment, speed is initially corrected; then, later in two microtrips, both speed and acceleration are corrected. The last microtrip does not require any correction.

Table 3. Comparison of average electricity consumption during driving in each segment in relation to the assumed boundary energy.

Parameter	Segment 1	Segment 2	Segment 3	Segment 4	Total	Difference %
Distance (km)	1.858	1.425	1.067	2.016	6.366	
Average energy for autopilot (Wh/km)	285.5	314.8	237.0	302.7	289.4	11.0
Average boundary energy (Wh/km)	259.6	276.8	278.3	241.1	260.7	0
Average energy for cycle with correction (Wh/km)	266.0	267.1	228.4	224.7	246.9	−5.3

**Figure 15.** Comparison of electricity consumption in the uncorrected and corrected cycle in relation to the assumed boundary energy in each segment and in the overall cycle.

4. Conclusions

This article presents an adaptive method for optimizing the driving cycle with regard to energy consumption. Compared to methods used to develop representative driving cycles, the method described herein proposes distance-based driving cycles instead of time-based driving cycles. Driving cycles are segmented based on a driving cycle dataset. The next state, determined by speed and acceleration, is defined as the Markov chain next stage. However, this state can be disrupted by traffic conditions. Thus, TPM is updated on an ongoing basis and corrected where necessary if energy consumption is greater than assumed. Energy consumption during driving is monitored and compared with the assumed boundary energy. An autopilot driving cycle was verified in the study, with the cycle adapting to very restrictive limits on energy consumption. Speed or product of the speed and acceleration (v_a) were reduced when consumption was too high. Energy consumption was reduced by approximately 15%, although travel time was prolonged by approximately 10%.

The tests showed that driving was most energy-efficient at low speeds and accelerations (e.g., driving in congestion). However, many users would not regard this as the optimum driving cycle. It is also necessary to consider travel time, which is a significant aspect in the case of buses, and traffic flow, although this parameter cannot be measured directly. Further study should focus on the optimization criteria and the algorithm used to determine the energy boundary.

The study does not deal in detail with the energy consumption of HVAC systems. However, this energy has been statistically included in the design of the energy boundary. While the motor consumes no electricity during the idling phase, HVAC energy consumption is a real challenge in EV.

This paper is relevant to the topic of energy management in so-called intelligent public transport. Energy management is important for the transport of people (car-sharing, public bus transport) and goods (delivery vehicles).

Author Contributions: Conceptualization, I.K.; methodology, I.K. and A.P.; software, I.K.; validation, A.P. and A.N.; formal analysis, A.P.; investigation, M.S. and T.S.; resources, M.S.; data curation, T.S.; writing—original draft preparation, I.K.; writing—review and editing, I.K.; visualization, I.K.; supervision, A.N. All authors have read and agreed to the published version of the manuscript.

Funding: This research received no external funding.

Conflicts of Interest: The authors declare no conflict of interest.

Abbreviations

DBADC	distance-based adaptive driving cycle
DC	driving cycle
EV	electric vehicle
GPR	Gaussian process regression
HEV	hybrid electric vehicle
HVAC	heating, ventilation and air-conditioning
MC	Markov chains
MCMC	Monte Carlo Markov chain
MLE	maximum likelihood estimation
PHEV	plug-in hybrid electric vehicle
SAPD	speed acceleration probability density
TPM	transition probability matrix
va	velocity and acceleration product

References

- Ashtari, A.; Bibeau, E.; Shahidinejad, S. Using Large Driving Record Samples and a Stochastic Approach for Real-World Driving Cycle Construction: Winnipeg Driving Cycle. *Transp. Sci.* **2012**, *48*, 170–183. [\[CrossRef\]](#)
- Berzi, L.; Delogu, M.; Pierini, M. Development of driving cycles for electric vehicles in the context of the city of Florence. *Transp. Res. Part D Transp. Environ.* **2016**, *47*, 299–322. [\[CrossRef\]](#)
- Brady, J.; Mahony, M. Development of a driving cycle to evaluate the energy economy of electric vehicles in urban areas. *Appl. Energy* **2016**, *177*, 165–178. [\[CrossRef\]](#)
- Sun, Z.; Wen, Z.; Zhao, X.; Yang, Y.; Li, S. Real-World Driving Cycles Adaptability of Electric Vehicles. *World Electr. Veh. J.* **2020**, *11*, 19. [\[CrossRef\]](#)
- Yuan, X.; Zhang, C.; Hong, G.; Huang, X.; Li, L. Method for evaluating the real-world driving energy consumptions of electric vehicles. *Energy* **2017**, *141*, 1955–1968. [\[CrossRef\]](#)
- Liu, X.; Ma, J.; Zhao, X.; Du, J.; Xiong, Y. Study on Driving Cycle Synthesis Method for City Buses considering Random Passenger Load. *J. Adv. Transp.* **2020**, *2020*, 1–21. [\[CrossRef\]](#)
- Brundell, K.; Ericsson, E. Influence of street characteristics, driver category and car performance on urban driving patterns. *Transp. Res. Part D Transp. Environ.* **2005**, *10*, 213–229. [\[CrossRef\]](#)
- Hung, W.T.; Tong, H.Y.; Lee, C.P.; Ha, K.; Pao, L.Y. Development of a Practical Driving Cycle Construction Methodology: A Case Study in Hong Kong. *Transp. Res. Part D Transp. Environ.* **2007**, *12*, 115–128. [\[CrossRef\]](#)
- Borucka, A.; Wiśniowski, P.; Mazurkiewicz, D.; Świdorski, A. Laboratory measurements of vehicle exhaust emissions in conditions reproducing real traffic. *Measurement* **2021**, *174*, 108998. [\[CrossRef\]](#)
- Chen, Z.; Zhang, Q.; Lu, J.; Bi, J. Optimization-based method to develop practical driving cycle for application in electric vehicle power management: A case study in Shenyang, China. *Energy* **2019**, *186*, 1157–1166. [\[CrossRef\]](#)
- Ma, R.; He, X.; Zheng, Y.; Zhou, B.; Lu, S.; Wu, Y. Real-world driving cycles and energy consumption informed by large-sized vehicle trajectory data. *J. Clean. Prod.* **2019**, *223*, 564–574. [\[CrossRef\]](#)
- Esser, A.; Zeller, M.; Foulard, S.; Rinderknecht, S. Stochastic Synthesis of Representative and Multidimensional Driving Cycles. *SAE Int.* **2018**. [\[CrossRef\]](#)
- Desrevelaux, A.; Bouscayrol, A.; Trigui, R.; Castex, E.; Klein, J. Impact of the Velocity Profile on Energy Consumption of Electric Vehicles. *IEEE Trans. Veh. Technol.* **2019**, *68*, 11420–11426. [\[CrossRef\]](#)
- Nyberg, P.; Frisk, E.; Nielsen, L. Generation of Equivalent Driving Cycles Using Markov Chains and Mean Tractive Force Components. *IFAC Proc.* **2014**, *47*, 8787–8792. [\[CrossRef\]](#)
- Semal, P. Monotone Iterative Methods for Markov Chains. *Linear Algebra Its Appl.* **1995**, *230*, 35–46. [\[CrossRef\]](#)
- Lee, T.-K.; Filipi, Z.S. Synthesis of Real-World Driving Cycles Using Stochastic Process and Statistical Methodology. *Int. J. Veh. Des.* **2011**, *57*, 17–36. [\[CrossRef\]](#)
- Gong, Q.; Midlam-Mohler, S.; Marano, V.; Rizzoni, G. An Iterative Markov Chain Approach for Generating Vehicle Driving Cycles. *SAE Int. J. Engines* **2011**, *4*, 1035–1045. [\[CrossRef\]](#)

18. Souffran, G.; Miegerville, L.; Guerin, P. Simulation of Real-World Vehicle Missions Using a Stochastic Markov Model for Optimal Powertrain Sizing. *IEEE Trans. Veh. Technol.* **2012**, *61*, 3454–3465. [[CrossRef](#)]
19. Silvas, E.; Hereijgers, K.; Peng, H.; Hofman, T.; Steinbuch, M. Synthesis of realistic driving cycles with high accuracy and computational speed, including slope information. *IEEE Trans. Veh. Technol.* **2016**, *65*, 4118–4128. [[CrossRef](#)]
20. Zhao, B.; Hofman, T.; Lv, C.; Steinbuch, M. Intelligent synthesis of driving cycle for advanced design and control of powertrains. In Proceedings of the IEEE Intelligent Vehicles Symposium (IV) 2018, Changshu, China, 26–30 June 2018. [[CrossRef](#)]
21. Puchalski, A.; Komorska, I.; Ślęzak, M.; Niewczas, A. Synthesis of naturalistic vehicle driving cycles using the Markov Chain Monte Carlo method. *Eksplloat. Niezawodn. Maint. Reliab.* **2020**, *22*, 316–322. [[CrossRef](#)]
22. Shi, S.; Nan, L.; Zhang, Y.; Chaosheng, H.; Liu, L.; Lu, B.; Cheng, J. Research on Markov property analysis of driving cycle. In Proceedings of the IEEE Vehicle Power and Propulsion Conference, Piscataway, NJ, USA, 10–18 October 2013; pp. 1–5.
23. Zhang, M.; Shi, S.; Cheng, W.; Shen, Y. Self-Adaptive Hyper-Heuristic Markov Chain Evolution for Generating Vehicle Multi-Parameter Driving Cycles. *IEEE Trans. Veh. Technol.* **2020**, *69*, 6041–6052. [[CrossRef](#)]
24. Lin, J.; Niemeier, D.A. Estimating Regional Air Quality Vehicle Emission Inventories: Constructing Robust Driving Cycles. *Transp. Sci.* **2003**, *37*, 330–346. [[CrossRef](#)]
25. Borucka, A.; Niewczas, A.; Hasilova, K. Forecasting the readiness of special vehicles using the semi-Markov model. *Eksplloat. Niezawodn. Maint. Reliab.* **2019**, *21*, 662–669. [[CrossRef](#)]
26. Austin, T.C.; DiGenova, F.J.; Carlson, T.R.; Joy, R.W.; Gianlini, K.A.; Lee, J.M. *Characterization of Driving Patterns and Emissions from Light-Duty Vehicles in California*; Final Report 1993; Sierra Research Inc.: Street Sacramento, CA, USA, 1993. [[CrossRef](#)]
27. Nesamani, K.S.; Subramanian, K.P. Development of a Driving Cycle for Intra-City Buses in Chennai, India. *Atmos. Environ.* **2011**, *45*, 5469–5476. [[CrossRef](#)]
28. Zähringer, M.; Kalt, S.; Lienkamp, M. Compressed Driving Cycles Using Markov Chains for Vehicle Powertrain Design. *World Electr. Veh. J.* **2020**, *11*, 52. [[CrossRef](#)]
29. Zhang, X.; Göhlich, D.; Li, J. Energy-Efficient Torque Allocation Design of Traction and Regenerative Braking for Distributed Drive Electric Vehicles. *IEEE Trans. Veh. Technol.* **2018**, *67*, 285–295. [[CrossRef](#)]
30. Xu, W.; Chen, H.; Zhao, H.; Ren, B. Torque optimization control for electric vehicles with four in-wheel motors equipped with regenerative braking system. *Mechatronics* **2019**, *57*, 95–108. [[CrossRef](#)]
31. Rasmussen, C.E.; Williams, C.K.I. *Gaussian Processes for Machine Learning*; MIT Press: Cambridge, MA, USA, 2006.

Article

Cooling System Energy Consumption Reduction through a Novel All-Electric Powertrain Traction Module and Control Optimization

Simone Lombardi *, Manfredi Villani *, Daniele Chiappini and Laura Tribioli

Department of Industrial Engineering, University of Rome Niccolò Cusano, Via Don Carlo Gnocchi, 3, 00195 Rome, Italy; daniele.chiappini@unicusano.it (D.C.); laura.tribioli@unicusano.it (L.T.)

* Correspondence: simone.lombardi@unicusano.it (S.L.); manfredi.villani@unicusano.it (M.V.)

Abstract: In this work, the problem of reducing the energy consumption of the cooling circuit for the propulsion system of an all-electric vehicle is approached with two different concepts: improvement of the powertrain efficiency and optimization of the control strategy. Improvement of the powertrain efficiency is obtained through a modular design, which consists of replacing the electric powertrain with several smaller traction modules whose powers sum up to the total power of the original powertrain. In this paper, it is shown how modularity, among other benefits, also allows reducing the energy consumption of the cooling system up to 54%. The energy consumption of the cooling system is associated with two components: the pump and the fan. They produce a so-called auxiliary load on the battery, reducing the maximum range of the vehicle. In conventional cooling systems, the pump and the fan are controlled with a thermostat, without taking into account the energy consumption. Conversely, in this work a control strategy to reduce the auxiliary loads is developed and compared with the conventional approach, showing that the energy consumption of the cooling system can be reduced up to 27%. To test the control strategy, numerical simulations have been carried out with a 1-D model of the cooling system. On the other hand, all the thermal loads of the components have been calculated with a vehicle simulator, which is able to predict the vehicle's behavior under different driving cycles.

Keywords: electric vehicle; propulsion cooling system; modularity; thermal management; control optimization

Citation: Lombardi, S.; Villani, M.; Chiappini, D.; Tribioli, L. Cooling System Energy Consumption Reduction through a Novel All-Electric Powertrain Traction Module and Control Optimization. *Energies* **2021**, *14*, 33. <https://doi.org/10.3390/en14010033>

Received: 15 November 2020

Accepted: 21 December 2020

Published: 23 December 2020

Publisher's Note: MDPI stays neutral with regard to jurisdictional claims in published maps and institutional affiliations.



Copyright: © 2020 by the authors. Licensee MDPI, Basel, Switzerland. This article is an open access article distributed under the terms and conditions of the Creative Commons Attribution (CC BY) license (<https://creativecommons.org/licenses/by/4.0/>).

1. Introduction

One of the most limiting factors of all-electric vehicles is the limited range [1,2]. The most advanced electric rechargeable energy storage systems (RESS), such as Li-ion batteries, still suffer of low energy density when compared to fuels, meaning that large and heavy batteries would be required to meet the travel range of conventional vehicles. In addition, severe ambient conditions can dramatically reduce the range and reliability of battery powered vehicles [3]. Another important drawback of all-electric vehicles is that the battery is the only energy storage on-board and therefore it is also required to provide the energy for the operation of the auxiliary loads, such as the air conditioning compressor and the fan and pump of the propulsion cooling system. In all-electric vehicles, reducing these loads is of primary importance, as they drain energy from the battery and can further decrease the range of the vehicle.

Generally, studies on the impact of auxiliary loads on energy consumption are limited to weather and climatic conditions—i.e., Heating, Ventilation, Air Conditioning (HVAC) consumption and thermal comfort measures [4–7]—driver behavior and traffic conditions. Lalhoul et al. [8] proposed a thermal comfort management approach that optimizes the thermal comfort while preserving the driving range during a trip is proposed. A large number of weather and traffic situations are simulated, and results show the efficiency

of the proposed approach in minimizing energy consumption while maintaining a good comfort. Similarly, Desrevaux et al. [9], in order to plan the annual charging operation of an eco-campus, developed a simulation tool for an accurate determination of the consumption of an electric vehicle throughout the year. An overconsumption up to 33% in winter due to heating, and only 15% in summer due to air conditioning was found. Basciotti et al. [10] developed advanced simulation tools to improve the efficiency of climate control systems in order to accurately evaluate both the energy savings and thermal comfort.

On the other hand, very seldom the influence on energy consumption owe to cooling of powertrain components is included in the analysis. For example, the integrated thermal management of a pure electric vehicle is described in [11], including battery cooling/preheating, electric machines (EM) cooling and Air Conditioning (AC) or heat pump. Different approaches are proposed, but not modularity nor optimized control. Shojaei et al. [12] investigate the impact of the cooling power demands of the cabin and battery on the vehicle performance, focusing more on comfort levels and battery degradation. In [13], the National Renewable Energy Laboratory's modeling framework was used to explore control strategies for an electric vehicle combined loop system. The control approach included a mode selection algorithm and controllers for the compressor speed, cabin blower flow rate, coolant flow rate, and the front-end heat exchanger coolant bypass rate. The impact of these thermal systems on electric vehicle range during warmup was simulated showing up to a 10.9% improvement in range for the full system over the baseline during warmup from cold soak. The need to reduce the significant energy drain and resulting drive range loss due to auxiliary electrical loads is also addressed in [14].

As shown in the above literature review, in most of the research works, the problem of reducing the energy consumption of the auxiliary loads in an all-electric vehicle is translated into the effort of reducing the energy consumption of the AC system. On the other hand, in this work the energy consumption of the auxiliaries used in the propulsion cooling system is considered and two approaches are proposed to reduce it. To the author's knowledge, there are no contributions in the literature where the reduction of the energy consumption of the auxiliary loads from the propulsion cooling system is investigated. The first approach, at a design level, is modularity. The second approach, at a control level, is the optimization of the energy management.

The concept of modularity has been developed in DRIVEMODE, a project funded by the European Commission under the Horizon 2020 framework. The DRIVEMODE project stems from the idea of integrating a high-speed gearbox, a high-speed electric motor (e-motor) and a Si-C inverter to provide a highly efficient and compact integrated drivetrain module (IDM) to be used in cars of different classes, including mass produced battery and hybrid electric vehicles, low performance and high performance vehicles and different types of heavy-duty vehicles. Multiple IDM can be used in place of single larger electric machines and power electronic components. In the modules, the smaller electric machines, even though characterized by lower maximum efficiencies, will work in more efficient regions of the operating map, resulting in a lower thermal load to be rejected through the cooling system. In this paper, it is shown how modularity, among other benefits, also allows reducing the energy consumption of the cooling system.

The second approach consists of improving the energy management of the propulsion cooling system. Most of the works regarding the thermal management in electric vehicles are focused on either improving the battery cooling [15–17] or the e-motor cooling [18,19], without taking into account the cooling system energy consumption. Conventional control strategies are based on a feedback control on the radiator inlet temperature, with a thermostat valve. An interesting control approach to reduce the motor cooling system energy consumption is proposed in [20], but the considered vehicle is a hybrid electric. In this work a control strategy that reduces the energy consumption of the cooling system, namely of pump and fan, has been tuned for steady-state conditions and then tested with numerical simulation on different driving cycles. Even though the benefits of this control

strategy are smaller compared to those obtained with modularity, the implementation comes at no costs, since it does not require additional components or sensors.

This work relies on numerical simulation of experimentally validated models. Transient simulations of driving cycles have been carried out with a robust 1-D model of the vehicle cooling system built in GT-Suite [21]. On the other hand, all the thermal loads of the components of the drivetrain have been calculated with a vehicle simulator developed in Matlab/Simulink® [22].

The remainder of this paper is organized as follows: Section 2 presents the single e-motor and dual IDM configurations and modeling; Section 3 describes the cooling circuits for the two cases; finally, in Section 4 the simulations are presented, and the results are discussed; the conclusions are presented in Section 5.

2. System Description and Modeling

The vehicle considered in this study is an all-electric sedan-class car. The main parameters of the vehicle are listed in Table 1.

Table 1. Characteristics of the vehicle.

Parameter	Value
vehicle mass	1745 kg
passenger mass	235 kg
vehicle frontal cross-section area	2.618 m ²
aerodynamic drag coefficient	0.29
tire rolling resistance coefficient	0.009
wheel radius	0.335 m

Two powertrain configurations are considered and further described in the next subsections: the single e-motor (with power electronics and transmission) and the dual Integrated Drivetrain Module (which incorporates e-motor, gearbox, and inverter). In both cases, the total power of the propulsion system must meet the speed and grade requirements indicated in Table 2.

Table 2. Performance requirements of the vehicle.

Parameter	Value
acceleration from 0 to 50 km/h	5.5 s
acceleration from 0 to 100 km/h	10 s
maximum climbing at 80 km/h	12%
maximum climbing at 130 km/h	4%
maximum speed	150 km/h

The general layout of the cooling system is composed of four integrated circuits (with a fifth separate loop for cooling charger and converters (400V-12V DC/DC and 800V-400V DC/DC)), as shown in Figure 1. The four loops are:

1. Air Conditioning (AC) refrigerant loop (shown in blue);
2. Heat Ventilation Air Conditioning (HVAC) coolant loop (shown in red);
3. Propulsion loop (shown in purple);
4. Rechargeable energy storage system (RESS) coolant loop (shown in green).

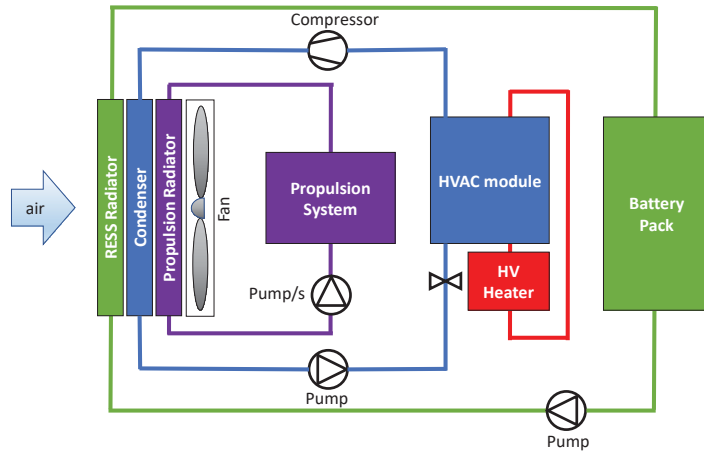


Figure 1. Cooling system circuits: AC refrigerant loop (blue), HVAC coolant loop (red), propulsion loop (purple), RESS loop (green).

The first loop provides air conditioning for cabin cooling through a compressed vapor cycle, whereas the second provides cabin heating. The third loop is responsible for the propulsion system cooling and the fourth loop ensures that the battery is maintained in the operating temperature range. These loops are all highly integrated, but this analysis is focused only on the propulsion coolant loop, which, however, is influenced by the HVAC refrigerant circuit through the condenser and by the RESS circuit through the RESS radiator: as shown on the left side of Figure 1, the same fan provides the air mass flow rate for the cooling of RESS, HVAC system (whose condenser is shown in blue) and propulsion module. The conditions of the air flow at the outlet of the RESS radiator and AC condenser are experimentally measured and used as an input to the simulations performed in this study.

2.1. Single Electric Motor

The conventional all-electric powertrain is composed of one single e-motor and one inverter. The e-motor is then connected through the transmission to the vehicle front wheels, as qualitatively shown in Figure 2.

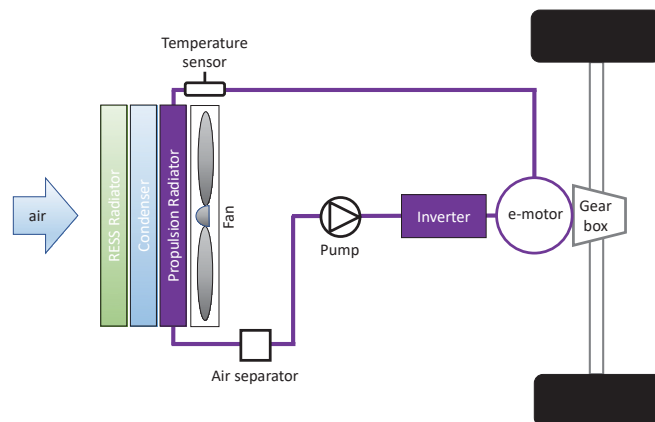


Figure 2. Single e-motor propulsion system and cooling system.

The electric machine has a max peak power of 150 kW and max/min continuous torque of 266 N·m, with corner speed of 1500 RPM. Figure 2 also shows the layout of the propulsion cooling system. The main components of the circuit are:

1. pipes and hoses;
2. the electric coolant pump;
3. the electric fan.

As already mentioned, the fan is used to suck in the air and increase the air mass flow rate through the radiators of propulsion, condenser and RESS cooling loops. The coolant consists of water mixed with ethylene glycol (50% water + 50% glycol).

2.2. Dual Integrated Drivetrain Module

Introducing the concept of modularity [23], two smaller e-motors can be used instead of the larger single motor. Each of the smaller e-motors is integrated with gearbox and Si-C inverter to form a highly efficient and compact integrated drivetrain module (IDM). Two 75 kW IDMs are used in this study to replace the single motor, as qualitatively shown in Figure 3.

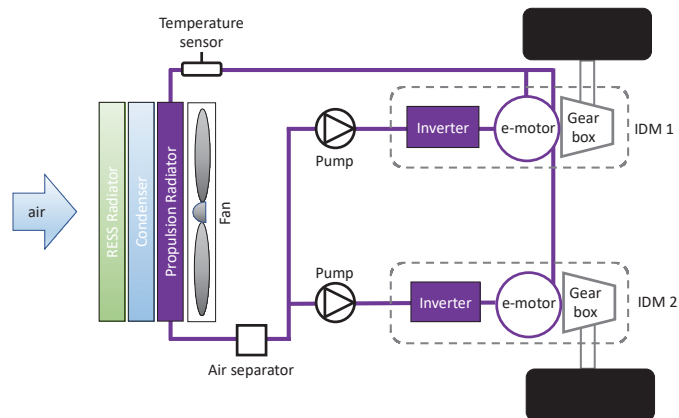


Figure 3. Dual IDM propulsion system and cooling system.

In particular, each module has a dedicated cooling circuit, with the coolant flowing through the IDM components in a series configuration. Eventually, the coolant streams coming from the two modules are sent to the same main radiator for heat rejection to the ambient. This configuration helps designing a single compact cooling circuit for the thermal management of all the propulsion components.

The benefits of modularity, i.e., using a larger number of smaller electric machines, are twofold: increased overall efficiency during the vehicle operation and reduced components heat rejection. The first benefit is explained considering that in a typical driving cycle the operating conditions will be mostly in the low-medium speeds and torques. This means that a larger EM will operate in the lower efficiency regions, while for a smaller EM most of the operating points will fall in the maximum efficiency region. Therefore, even though the larger EM could achieve greater maximum efficiency, during a driving cycle the overall efficiency of a modular propulsion system will be higher. The second benefit is strictly related to the first one, as a more efficient operation of the powertrain components will lead to less losses and heat rejection. This, in turn, will reduce the energy demand of the propulsion system cooling circuit, further improving the overall vehicle energy consumption.

2.3. Electric Vehicle Model

E-motor and inverter generate heat during their operation, especially at high power demands, because of ohmic losses. The cooling system is required to reject the generated thermal load to the ambient, keeping the temperatures within the operating range of the components. To evaluate the thermal load generated during the propulsion system operation, a quasi-static model of the electric vehicle has been developed in Matlab/Simulink®. The power losses in the inverter \dot{Q}_{INV} , which are equal to the heat generated, can be calculated as a function of the instantaneous inverter power P_{INV} , with the following equation:

$$\dot{Q}_{INV} = P_{INV}(1 - \eta_{INV}) \quad (1)$$

where for the inverter efficiency η_{INV} a constant average value equal to 97% has been used. This value results in being a bit conservative with respect to the first measurements at test bench.

On the other hand, the thermal load of the e-motor, \dot{Q}_{EM} , can be calculated as a function of the motor power, P_{EM} , and efficiency, η_{EM} , using the following equation:

$$\dot{Q}_{EM} = P_{EM}(1 - \eta_{EM}) \quad (2)$$

The efficiency of the single e-motor is evaluated from the map shown in Figure 4, which is obtained in [23] with the method proposed in [24].

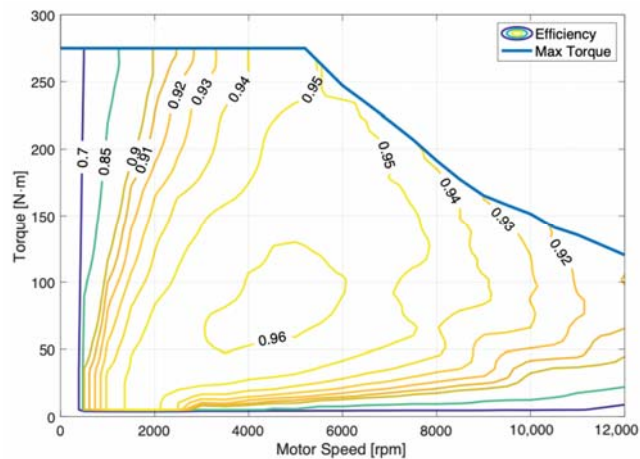


Figure 4. Single e-motor efficiency map.

For the e-motors of the two IDMs, the Willans line model [25] has been used to scale down the single e-motor map. The result is shown in Figure 5, with the maximum peak power of the scaled motors being one half of the maximum power of the original e-motor. Thus, the two e-motors for the dual IDM configuration have the same total power as the single e-motor configuration.

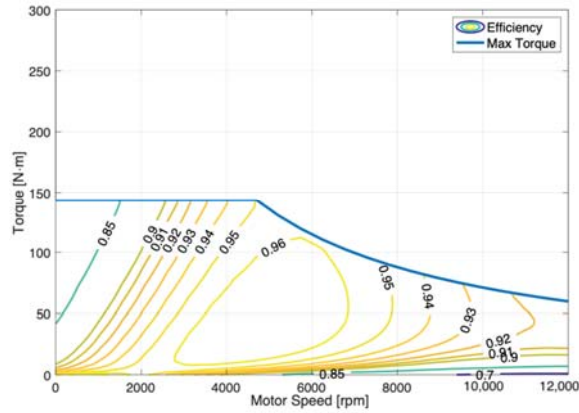


Figure 5. IDM e-motor efficiency map.

The maps shown in Figures 4 and 5 have been implemented in the Matlab/Simulink® model to obtain a quasi-static forward-looking simulator of the entire vehicle. The power demand on the propulsion system components is evaluated by solving the longitudinal dynamics of the vehicle and using the following expression of the road load:

$$F_{load} = \frac{1}{2}C_d\rho_{air}A_fv^2 + Mg \sin\theta + C_rMg \cos\theta \quad (3)$$

The first term on the right-hand side of Equation (3) is the aerodynamic drag force, with C_d the drag coefficient, ρ_{air} the air density, A_f the frontal area of the vehicle and v the longitudinal speed of the vehicle. The second term is the force due to the road grade θ , where g is the gravity constant and M is the vehicle mass. Finally, the third term is the rolling resistance force, which is a function of grade, vehicle mass and tires rolling resistance coefficient C_r . The values of these parameters have been previously reported in Table 1.

The simulator includes a driver’s model based on a PID controller to track the desired speed profile (i.e., driving cycle) and a zero-th order equivalent circuit model for the battery. The main characteristics for the battery pack are listed in Table 3.

Table 3. Battery pack main characteristics.

Parameter	Value
operating voltage (Max/Nominal)	796/720 V DC
operating current (Max/Nominal)	280/140 A
battery capacity	46 kWh

The battery performance is obtained starting from the open circuit voltage (OCV) and internal resistance (R_0) curves, shown in Figures 6 and 7, which have been derived from data available in [26] for a Li-Ion battery cell manufactured by A123 Systems, LCC (Livonia, MI, USA).

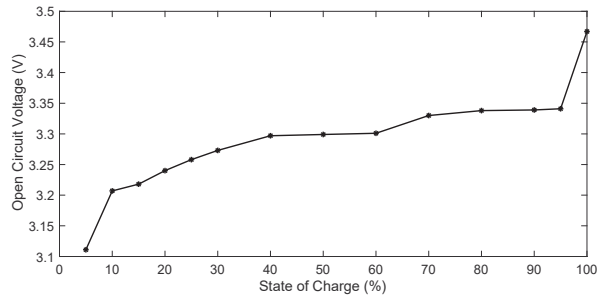


Figure 6. Battery cell open circuit voltage dependence on state of charge.

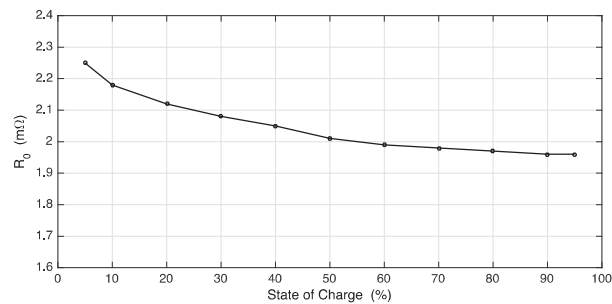


Figure 7. Battery cell internal resistance dependence on state of charge.

With the zero-th order equivalent circuit model the battery heat rejection, \dot{Q}_{batt} , can be calculated as:

$$\dot{Q}_{batt} = I^2 \cdot R_0(SoC) \quad (4)$$

The battery current I is a function of the battery open circuit voltage, V_{OC} , the power request, P_{batt} , and the equivalent internal resistance $R_0(SoC)$, function of the state of charge (SoC):

$$I = \frac{V_{OC} - \sqrt{V_{OC}^2 - 4P_{batt}R_0}}{2R_0} \quad (5)$$

2.4. Cooling Circuit Model

The heat rejection profiles for each component, obtained with the Matlab/Simulink® model described above, are then used as input for the propulsion cooling circuit model developed in GT-Suite and shown in Figure 8. The other input to the GT-model is the vehicle speed, which is directly related to the air flow through the cooling system radiators. Two sides or two circuits are highlighted in the model:

- Coolant side (red)—closed loop circuit with pump, accumulator, IDM components, etc.;
- Air side (blue)—circuit with Fan object, RESS and Condenser heat addition objects.

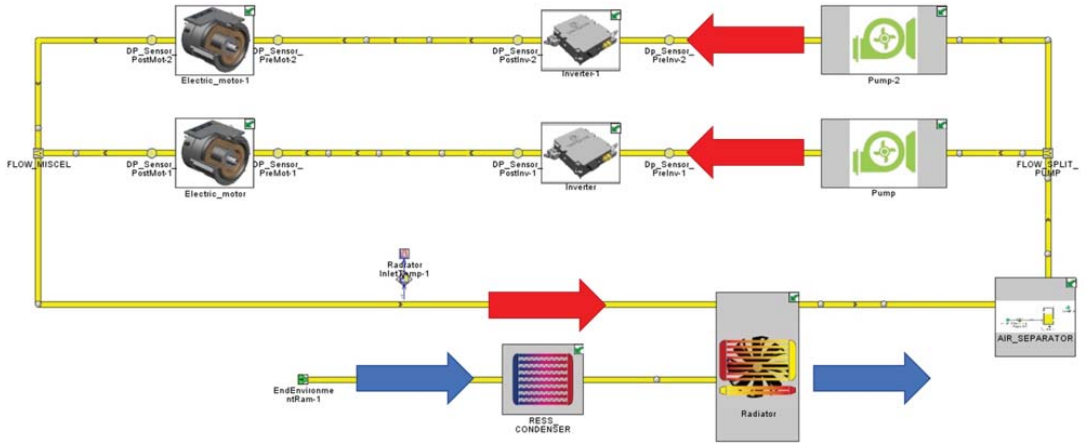


Figure 8. Propulsion cooling system model in GT-Suite (dual e-motor configuration).

The main components of the circuit have been modeled as follows:

- the coolant (water/glycol ethyl 50-50) properties are retrieved from the RefPROP [27] library;
- pipes and hoses, whose dimensions are the results of a sensitivity analysis aiming to minimize the circuit pressure drops and ensuring the required mass flow rate for cooling, have inner diameter of 19 mm, locally 18 mm in some connectors;
- the coolant pump, which is an electric pump, is modeled with the operating map shown in Figure 9;
- the electric fan, modeled with the operating map shown in Figure 10.

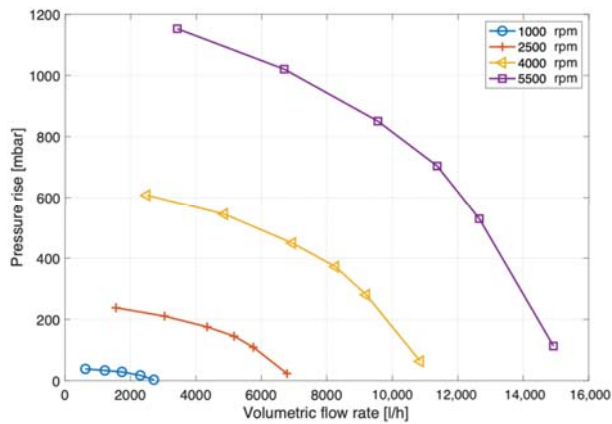


Figure 9. Cooling system pump map.

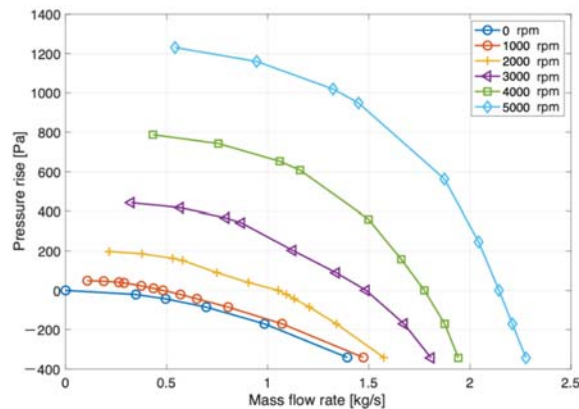


Figure 10. Cooling system fan map.

Additionally, the thermal load of the propulsion radiator is an output of the analysis rather than an input. All the data needed to model the heat transfer behavior of the radiator have been provided by the car manufacturer. The performance that the propulsion cooling system must meet are summarized in Table 4. In particular, the temperature must not exceed 65 °C. In the case of the dual IDM the constraint on the minimum volumetric flow rate imposes the usage of two pumps. This has been found to be consistent with the modularity requirement of the DRIVEMODE project, since each module comes with its own pump.

Table 4. Preliminary requirements for the cooling circuit.

e-motor	
temperature (inlet)	<65 °C
pressure drop	<500 mbar @ 10 L/min
vol. flow rate	>10 L/min @ maximum power
inverter	
temperature (inlet)	<65 °C
pressure drop	<300 mbar @ 10 L/min
vol. flow rate	>10 L/min @ maximum power

3. Cooling Circuit Control Strategy

The second approach to reduce the energy consumption from the auxiliary loads related to the propulsion cooling system consists of optimizing the control strategy of fan and pump. The fan is responsible for increasing the air flow through the radiator, thus improving the heat rejection when the driving loads are high. The pump is used to ensure the desired flow of coolant through the propulsion system components and keep their temperature in the admissible range. In the following subsections, the conventional control strategy and the proposed optimized strategy are presented. Both strategies apply to either the single e-motor or the dual IDM configurations.

3.1. Conventional Control

The conventional control strategy acts on two control variables, which are the pump speed, and the input signal of the fan (on/off). The pump speed is initially set at 10 L/min and then it is linearly increased as the coolant temperature at the radiator inlet increases above 40 °C. The fan is off as long as this temperature is below 65 °C. For higher values, the fan is switched on at its maximum capacity (i.e., input signal equal to 90%) and is maintained on until the temperature drops down below 55 °C, performing a hysteresis

cycle. When the radiator inlet temperature reaches 65 °C and the fan is turned on, the pump flow rate is kept constant at its maximum value. The linear dependency of the pump speed (proportional to the pump flow rate) on the coolant temperature at the radiator inlet is shown in Figure 11. The minimum pump speed corresponds to 10 L/min, as per the constraint reported in Table 4, while the maximum volumetric flow rate is obtained for the maximum pump speed.

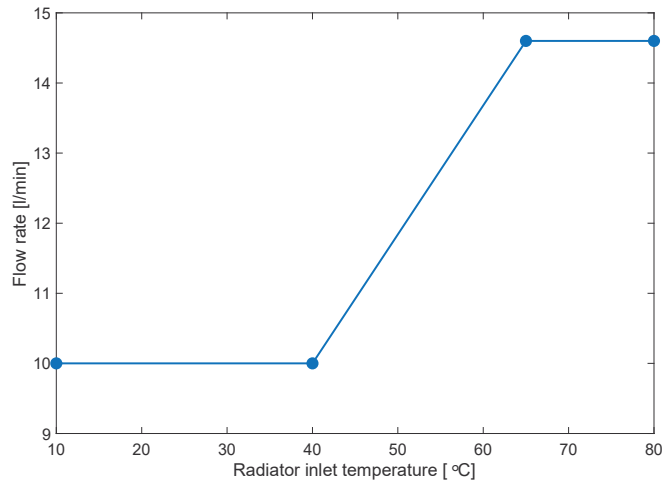


Figure 11. Pump conventional control strategy: linear dependence of mass flow rate on coolant temperature at radiator inlet.

3.2. Optimized Control

The optimized control strategy aims at reducing the energy consumption of pump and fan, ensuring the temperature constraints on the e-motor and inverter are met. In contrast with the conventional strategy, in this case the speed of the pumps is controlled based on the actual vehicle speed, actual heat rejection of the components and fan state. These signals are already available in the vehicle, as they are used for other tasks of the electronic control unit, so no additional sensors are required to implement the new control strategy.

The control strategy is built on the observation that for a given vehicle speed and thermal load on the cooling circuit, the pump speed corresponding to the minimum energy consumption is the lowest possible speed that avoids the fan to be switched on. Therefore, an optimization process has been carried out to evaluate the minimum pump speed required to reject different thermal loads at different vehicle speeds, without turning on the fan. A design of the experiment was performed with the Matlab/Simulink[®] simulator, varying vehicle speed and road grade to obtain the heat rejection of the components for different road load conditions. Those results were then used for steady-state simulations of the 1-D GT-Suite cooling circuit together with built in optimization algorithms from GT-Suite to create the control map shown in Figure 12. For the same vehicle speed, higher loads correspond to higher heat rejections and require higher mass flow rates (thus, pump speeds).

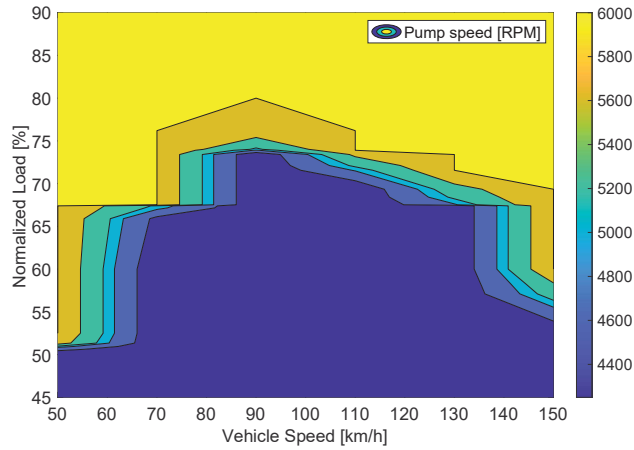


Figure 12. Optimized control strategy: optimized pump speed as a function of vehicle speed and propulsion normalized load.

The map shows a step-shape because the pump speed has a low impact on the coolant temperature. Indeed, the most important variables for the heat transfer in the radiator are the air mass flow rate and the air temperature, which are influenced by vehicle speed and fan state. In other words, for the same level of required heat rejection, while the speed of the pumps can only produce a small change of the radiator inlet temperature, the fan state and vehicle speed can have a much greater impact. As a result, there is no advantage in maintaining high pump speeds during the fan operation, because the main contribution to lowering the temperature is from the fan, and the increasing fan operational time is negligible. Following this consideration, the optimal pump speed from the map is overwritten when the fan is turned on, setting the speed to its minimum value.

In the first step of the control strategy, the calculation of the pump speed is only based on the actual vehicle speed (i.e., air flow rate through the radiator) and heat rejection from the components, using the control map shown in Figure 12, which is embedded into a 2D lookup table. The actual optimal speed output signal from the 2D lookup table is time averaged to smooth speed variations. This is necessary to dampen the dynamics of the inputs to the lookup table, which is built from steady-state simulations.

In a second step, the actual coolant temperature at the radiator inlet is checked. If the temperature of the coolant exceeds 60 °C, then the fan is turned on and the minimum pump speed is imposed, overwriting the optimal speed output of the 2D lookup table. The fan performs the same hysteresis cycle between 60 °C and 55 °C as already described in the previous section.

To summarize, the control strategy is designed to optimize the speed of the pump(s) when the fan is off, and to set it to the minimum allowed value when the fan is on:

$$n_{\text{pump}}(x_{\text{fan}}, \dot{Q}_{\text{loss}}, v_{\text{vehicle}}) = \begin{cases} \bar{n}_{\text{pump}}(\dot{Q}_{\text{loss}}, v_{\text{vehicle}}), & x_{\text{fan}} = 0 \\ n_{\text{pump}} = 4250 \text{ rpm}, & x_{\text{fan}} = 1 \end{cases} \quad (6)$$

where x_{fan} is the actual state of the fan, equal to 1 if the fan is on and equal to 0 if the fan is off; \dot{Q}_{loss} represents the total heat rejection of the components that is a function of time; v_{vehicle} is the actual vehicle speed; n_{pump} is the speed of the pump and \bar{n}_{pump} is the time averaged value of n_{pump} coming from the optimized control map. After a sensitivity analysis the averaging time of \bar{n}_{pump} has been set equal to 25 s for all the simulations.

4. Simulations and Results

To investigate the operation and performance of the cooling system, three different driving cycles (i.e., vehicle speed time profiles) have been selected: Aachen drive cycle, shown in Figure 13a; Federal Highway Driving Schedule (FHDS) drive cycle (repeated 10 times), shown in Figure 13b; World harmonized Light-duty vehicles Test Procedure (WLTC) drive cycle (repeated 3 times), shown in Figure 13c.

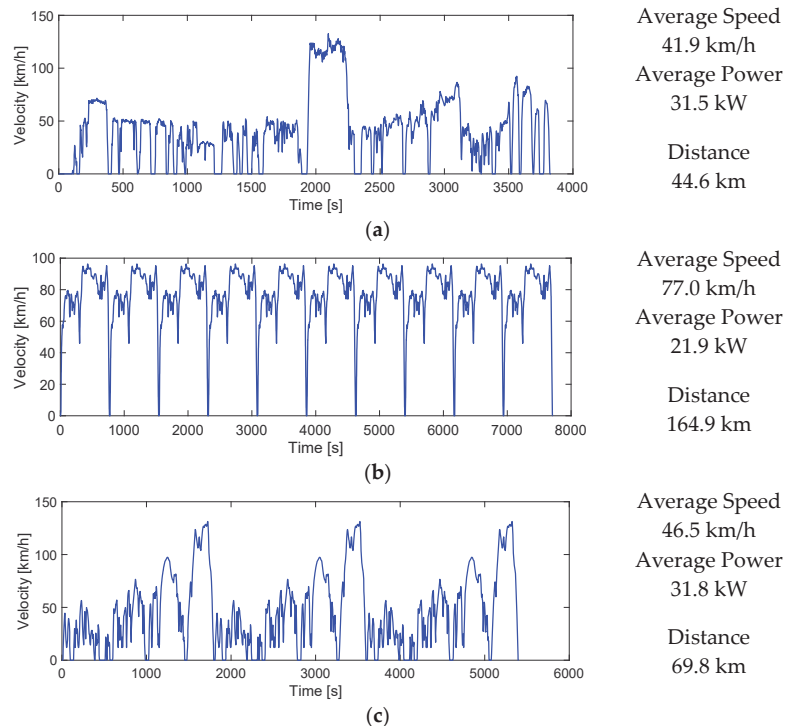


Figure 13. Test driving cycles: (a) Aachen; (b) FHDS \times 10; (c) WLTC \times 3.

The cycle repetitions are needed to obtain the same cooling circuit operating time and realistic trip length. Also, to add variability to the road power demand, each cycle repetition is characterized by a different road grade profile.

In the Matlab/Simulink[®] forward-looking model both the single motor and dual IDM configurations were simulated for the three driving cycles. The main outputs of these simulations are the heat rejection profile of the components and the effective vehicle speed. The operating average efficiency of the e-motors for the different driving cycles and the different powertrain architectures is reported in Table 5. It is clear that the modularity can improve the operating efficiency of the e-motors, thus reducing the heat generation that the cooling circuit will have to reject to the ambient.

Table 5. E-motor average efficiency.

Driving Cycle	Single e-motor EM Efficiency (%)	Dual IDM EM Efficiency (%)
Aachen	82.8	92.6
FHDS \times 10	83.5	88.4
WLTC \times 3	88.4	93.5

The heat rejection profile and the vehicle speed are then used as inputs to the GT-Suite model, which solves the transient 1-D thermo-fluid dynamic problem and evaluates the performance of the cooling circuit. Both the conventional and the optimized control strategy for the pump(s) control are simulated.

The effectiveness of the control strategies has been tested under the following additional assumptions: constant gear box efficiency of 0.97; mass of the vehicle equal to the gross weight; no AC condenser heat rate; ambient temperature of 40 °C; coolant initial temperature of 40 °C. These extreme operating conditions have been chosen to stress the cooling system and trigger fan starting events. As an example, Figure 14 shows the heat rejections of the motor, inverter, and battery with respect to time for the WLTC \times 3 cycle.

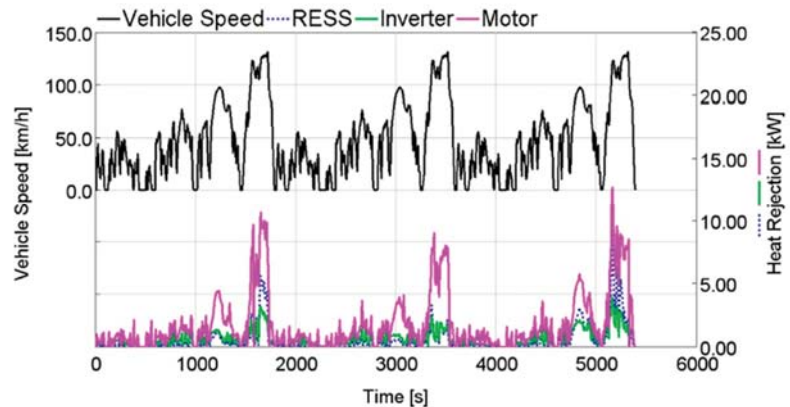


Figure 14. Outputs of the all-electric vehicle model: actual vehicle speed profile (top); motor, inverter and RESS heat rejections vs. time (bottom).

As one may note, there is a correlation between the velocity profile and the heat rejection, which is obviously affected by the road load. These plots are mostly provided to prove the soundness of the energy-based vehicle simulator. Those heat rejections have been calculated with the set of equations from (1) to (4).

Results Discussion and Comparison

To understand the impact of modularity and optimized control strategy on the energy consumption reduction, four cases have been analyzed for every driving cycle:

1. Single e-motor, standard propulsion cooling management;
2. Single e-motor, optimized propulsion cooling management;
3. Dual IDM, standard propulsion cooling management;
4. Dual IDM, optimized propulsion cooling management.

The different driving cycles highlight different aspects of the powertrain configurations and control strategies.

For the WLTC \times 3 drive cycle, the speeds of pump and fan (which can be considered to be a measure of the energy consumption) are shown in Figures 15 and 16 for the single e-motor and the dual IDM configurations, respectively. The WLTC \times 3 is the most power demanding driving cycle and in all the cases the fan must be activated to lower the coolant temperature. Moreover, comparing Figures 15 and 16, the single e-motor configuration requires one more fan start due to the higher heat rejection of the components in this powertrain.

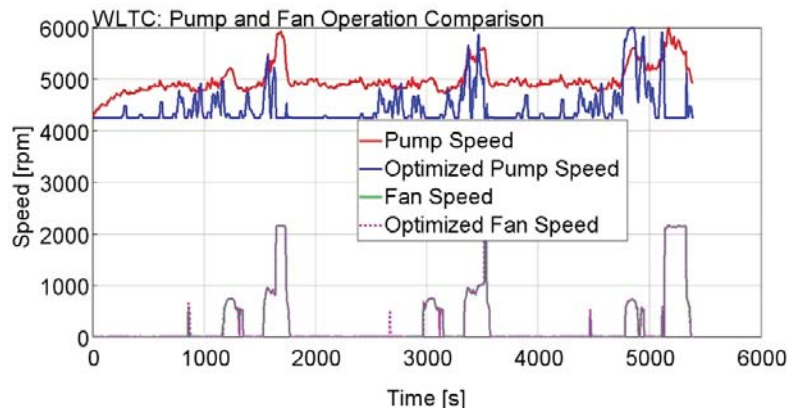


Figure 15. Control strategy comparison for single e-motor on WLTC driving cycle: coolant pump speed (top); radiator fan speed (bottom).

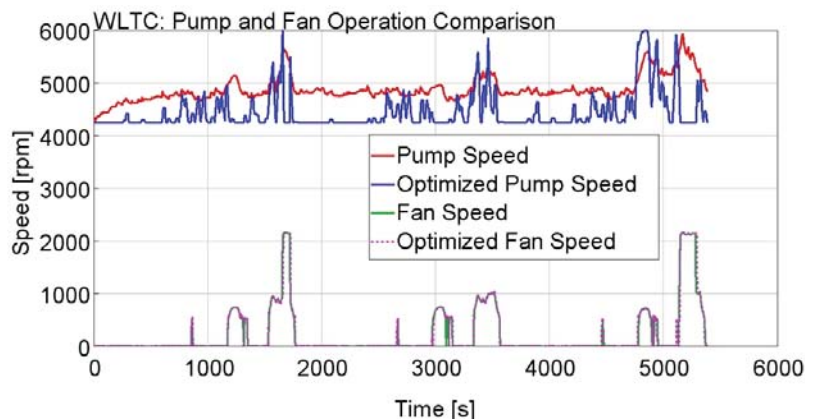


Figure 16. Control strategy comparison for dual IDM on WLTC driving cycle: coolant pump speed (top); radiator fan speed (bottom).

The bar plot in Figure 17 allows a comparison among the energy consumptions of every component, for both configurations and control strategies. The optimized control strategy for the dual IDM leads to higher fan energy consumption compared to the conventional strategy because the minimum pump speed is imposed during the fan operation time. However, the overall energy consumption is still better for the optimized control strategy because the energy savings of the pumps are much greater than the increased fan consumption. This confirms that the contribution of the fan on lowering the coolant temperature is prominent with respect to the pump. Furthermore, setting the pumps at the minimum speed leads to only a few seconds of fan additional operating time. For a specific powertrain (e.g., either Figure 15 or Figure 16), it is difficult to observe the differences in the fan operation times, since the pump(s) only have a limited impact on the coolant temperature. However, the difference between conventional and optimized control strategy is evident in terms of pump speed. As expected, the optimized control strategy is able to minimize the pump(s) speed, thus their energy consumption during most of the trip length.

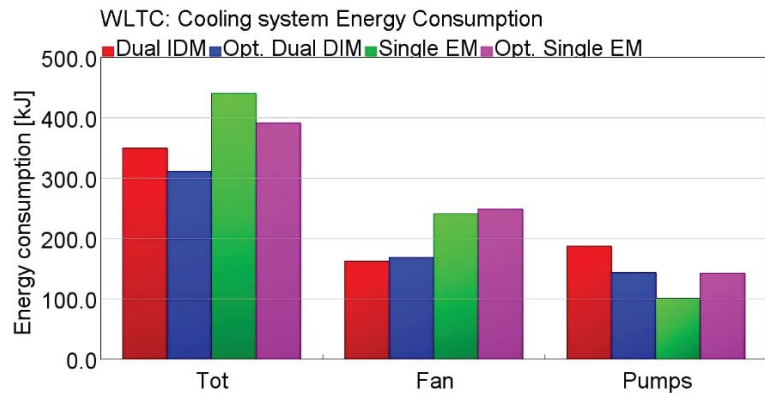


Figure 17. Impact of modularity and optimized control strategy on the energy consumption reduction for the WLTC driving cycle.

Regarding the temperature profiles at the radiator inlet, Figure 18 shows the differences for the four cases.

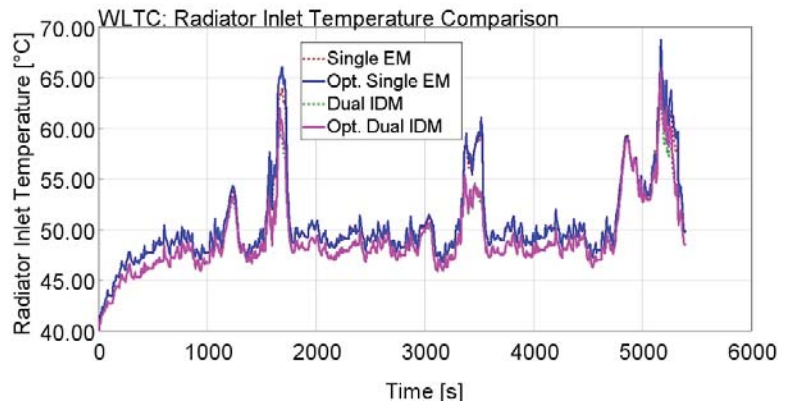


Figure 18. Impact of modularity and optimized control strategy on the coolant temperature at the radiator inlet for the WLTC driving cycle.

The difference in the shape of the peaks (see left plots in Figure 18) is caused by the difference in the actual battery state of charge and grade conditions for the three repetitions, leading to different maximum heat rejections. Because of the high energy demand and road grade, the single e-motor configuration is not able to meet the radiator inlet temperature constraint and both conventional and optimized control strategy lead to temperatures higher than 65 °C during the heat rejection peaks. On the other hand, the dual IDM configuration always meets the constraint with the conventional controller, while the optimized controller slightly exceeds 65 °C for 20 s. Comparing the four cases, the temperature is lower in the dual IDM configuration during the whole trip and there is no temperature difference between optimized and conventional control strategy when the fan is turned off.

The results for the FHDS drive cycle that is the less power demanding cycle, are shown in Figures 19–22.

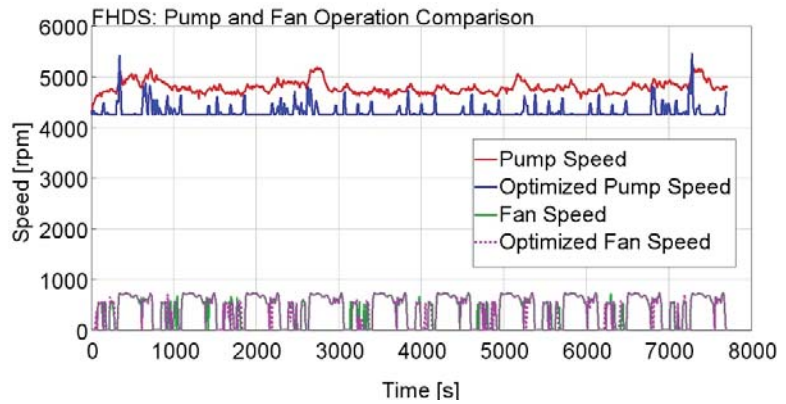


Figure 19. Control strategy comparison for single e-motor on FHDS driving cycle: coolant pump speed (top); radiator fan speed (bottom).

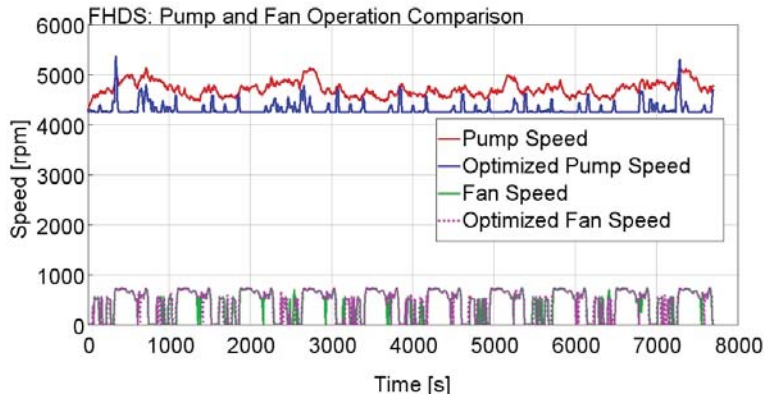


Figure 20. Control strategy comparison for dual IDM on FHDS driving cycle: coolant pump speed (top); radiator fan speed (bottom).

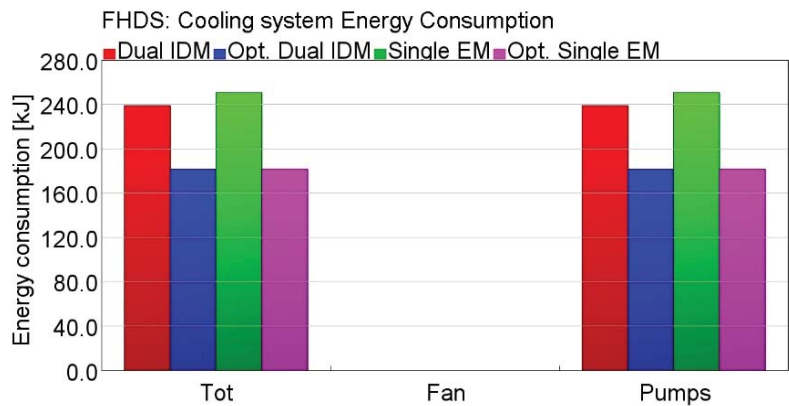


Figure 21. Impact of modularity and optimized control strategy on the energy consumption reduction for the FHDS driving cycle.

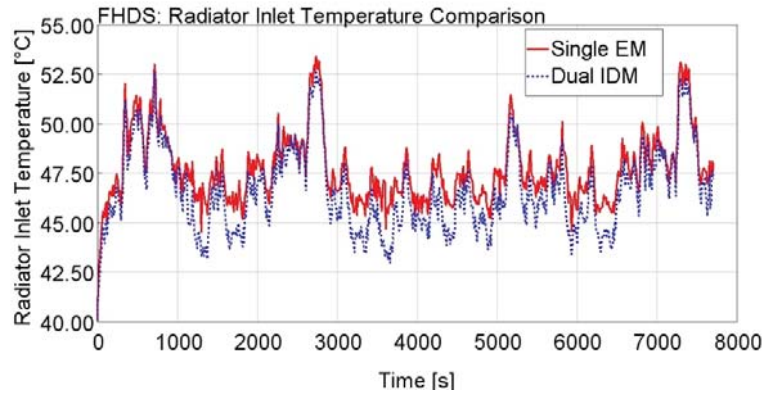


Figure 22. Impact of modularity and optimized control strategy on the coolant temperature at the radiator inlet for the FHDS driving cycle.

Even though Figures 19 and 20 show a non-zero fan speed, in both cases the fan is never switched on and the reported speeds result from the vehicle speed dragging the fan blades and producing the so-called “windmill” effect. This results in a clear energy saving for the optimized control strategy, as shown in the bar plot in Figure 21. In this driving cycle, the optimized control map leads to lower average speeds, thus the pump(s) give a significant contribution to the energy consumption reduction, while the conventional control strategy sets a high speed on average because the coolant temperature is in the range 50–55 °C most of the time, as shown in Figure 22, resulting in higher energy consumptions. Figure 22 also shows that for each powertrain configuration, the optimized control strategy leads to nearly the same temperature as the conventional strategy, such that the two temperature profiles overlap, and only one profile is shown in Figure 22. It can be concluded that in medium-low road power demand conditions the optimized control strategy can reduce the propulsion cooling system energy consumption.

Finally, for the Aachen driving cycle, the simulation results are shown in Figures 23–26. In this case, a large difference is found for the two powertrain configurations. In general, these simulations show how modularity can reduce the total heat rejection thanks to the higher operating efficiency of the 2 IDMs, therefore the cooling system is less stressed and energy consumption is lower. Comparing Figures 23 and 24, the dual IDM configuration never turns on the fan (also in this case the speed of the fan is due to windmill effect), while the single e-motor requires multiple fan starts. Looking at Figure 23, for the single e-motor the operation time of the fan is longer with the optimized control strategy, due to the lower pump speed imposed during the fan operation time. However, this little drawback is canceled out by the lower optimized pump speed (thus energy consumption) during the whole trip length.

Finally, the consumptions for the Aachen drive cycle are summarized in the bar plot in Figure 25. Regarding the temperatures, Figure 26 shows in detail the temperature difference between optimized and conventional control strategy, with slightly higher temperatures for the optimized strategy, which in turn result in lower energy consumptions, still meeting the cooling requirements.

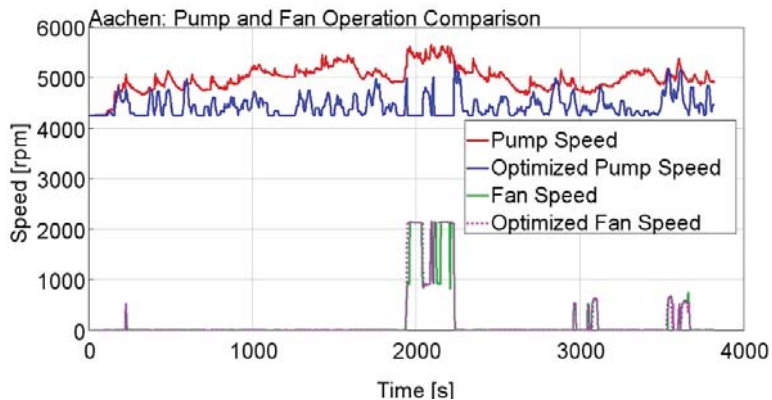


Figure 23. Control strategy comparison for single e-motor on Aachen driving cycle: coolant pump speed (top); radiator fan speed (bottom).

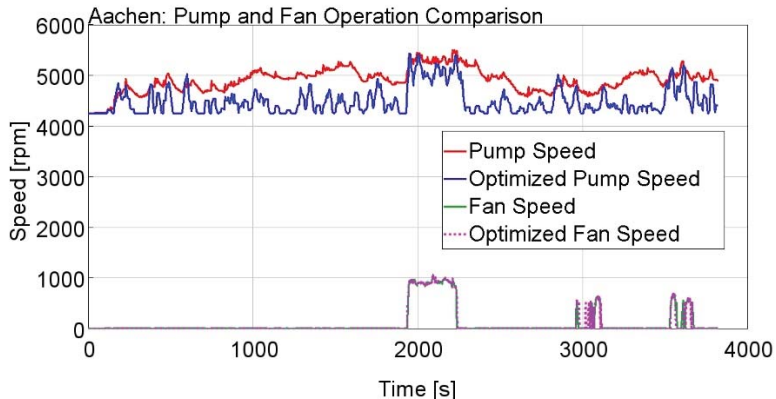


Figure 24. Control strategy comparison for dual IDM on Aachen driving cycle: coolant pump speed (top); radiator fan speed (bottom).

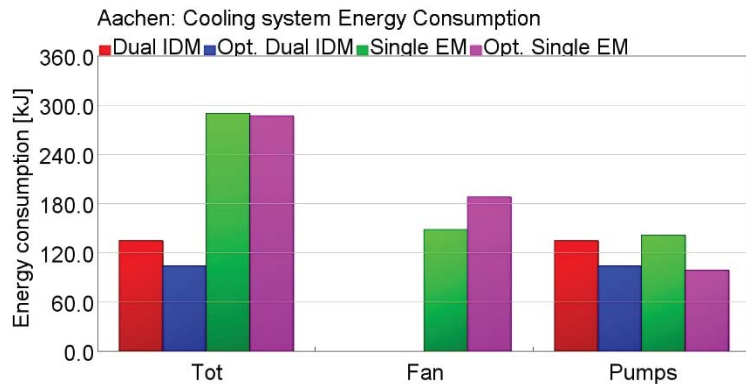


Figure 25. Impact of modularity and optimized control strategy on the energy consumption reduction for the Aachen driving cycle.

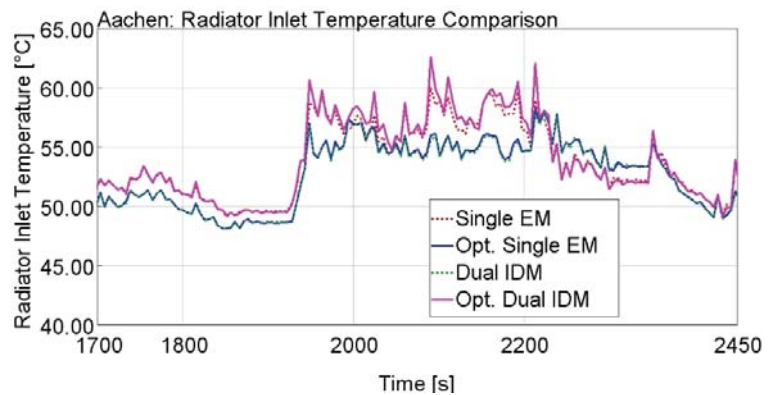


Figure 26. Impact of modularity and optimized control strategy on the coolant temperature at the radiator inlet for the Aachen driving cycle.

5. Conclusions

Methods to reduce the propulsion system cooling circuit energy consumption in an all-electric vehicle have been investigated in this paper. To achieve the goal of reducing the energy consumption of the auxiliaries that actuate the propulsion cooling system, both improvement of the powertrain efficiency and optimization of the cooling system control strategy have been analyzed. In particular, the improvement of the powertrain efficiency is obtained with a dual integrated drivetrain module configuration, which allows for lower heat rejection from the drivetrain components. On the other hand, an optimized control strategy for the cooling system has been designed in order to minimize the power demand of the cooling system. The cooling system simulations have been carried out with a 1-D model built upon experimental data in GT-Suite, while a vehicle simulator developed in Matlab/Simulink[®] has been used to evaluate the thermal loads of the components under different driving cycles. From the analysis of the results presented in the previous section, the following conclusions can be drawn:

1. The dual IDM configuration leads to an overall efficiency improvement due to the increased average efficiency of the e-motors, which intrinsically results in lower heat rejection and lower energy demand from the propulsion cooling system. However, in terms of energy consumption reduction of the propulsion system cooling circuit, the benefit of the dual IDM configuration steps out only in severe load conditions that stress the cooling circuit and trigger the fan. Indeed, for the FHDS driving cycle, the single e-motor and dual IDM have similar performance in terms of cooling circuit energy consumption. In this case, compared to the single e-motor configuration, modularity achieves only a 5% reduction of energy consumption. However, in the WLTCx3 and Aachen driving cycles, modularity results in a 21% and 54% reduction of energy consumption of the propulsion cooling system compared to the single e-motor configuration, respectively.
2. The optimized control strategy implemented in the propulsion cooling management always leads to lower energy consumption. The effectiveness of the control strategy comes from the reduction of the energy consumption of the cooling circuit pumps. Because of this, the optimized propulsion cooling management steps out in medium load conditions, when the control of the speed of the pumps is needed to lower the coolant temperature, but no action from the fan is requested. Indeed, when the fan is turned on, it will increase the overall consumption of the cooling circuit, decreasing the relative weight of the pumps on the consumption and consequently decreasing the impact of the optimized control strategy. In the Aachen driving cycle, compared to the single e-motor, the optimal control strategy achieves a 1% energy consumption

reduction, whereas 11% and 27% reductions are achieved for the WLTCx3 and FHDS driving cycles, respectively.

As a consequence of conclusions 1 and 2, in order to decrease the auxiliary loads of the propulsion cooling system in all-electric powertrains, increasing the powertrain efficiency leads to good results only if the cooling circuit is stressed enough, or in other words, if the fan is activated during the vehicle operation. On the other hand, the optimization of the control strategy is relevant if normally the cooling circuit is capable of lowering the coolant temperature without the intervention of the fan.

Author Contributions: Conceptualization: S.L., M.V., D.C. and L.T.; Formal analysis, S.L., M.V., D.C. and L.T.; Investigation, S.L. and L.T.; Methodology, M.V. and L.T.; Project administration, D.C. and L.T.; Software, S.L.; Supervision, D.C. and L.T.; Validation, S.L.; Visualization, M.V.; Writing—original draft, M.V.; Writing—review & editing, M.V., D.C. and L.T. All authors have read and agreed to the published version of the manuscript.

Funding: This project has received funding from the European Union’s Horizon 2020 research and innovation program under grant agreement No 769989. The opinions expressed in this document reflect only the author’s view and reflects in no way the European Commission’s opinions. The European Commission is not responsible for any use that may be made of the information it contains.

Institutional Review Board Statement: Not applicable.

Informed Consent Statement: Not applicable.

Data Availability Statement: The data presented in this study are possibly available on request from the corresponding authors. The data are not publicly available due to confidentiality reasons.

Conflicts of Interest: The authors declare no conflict of interest.

References

- Varga, B.; Sagoian, A.; Mariasiu, F. Prediction of Electric Vehicle Range: A Comprehensive Review of Current Issues and Challenges. *Energies* **2019**, *12*, 946. [\[CrossRef\]](#)
- Michaelides, E.E. Thermodynamics and energy usage of electric vehicles. *Energy Convers. Manag.* **2020**, *203*, 112246. [\[CrossRef\]](#)
- Iora, P.; Tribioli, L. Effect of Ambient Temperature on Electric Vehicles’ Energy Consumption and Range: Model Definition and Sensitivity Analysis Based on Nissan Leaf Data. *World Electr. Veh. J.* **2019**, *10*, 2. [\[CrossRef\]](#)
- Samadani, E.; Fraser, R.; Fowler, M. Evaluation of air conditioning impact on the electric vehicle range and li-ion battery life. *SAE Tech. Pap.* **2014**, *1*. [\[CrossRef\]](#)
- Rugh, J.; Farrington, R. *Vehicle Ancillary Load Reduction Project Close-Out Report: An Overview of the Task and a Compilation of the Research Results*; National Renewable Energy Laboratory: Golden, CO, USA, 2008.
- Gao, G. Investigation of climate control power consumption in DTE estimation for electric vehicles. *SAE Tech. Pap.* **2014**, *1*. [\[CrossRef\]](#)
- Kambly, K.R.; Bradley, T.H. Estimating the HVAC energy consumption of plug-in electric vehicles. *J. Power Sources* **2014**, *259*, 117–124. [\[CrossRef\]](#)
- Lahlou, A.; Ossart, F.; Boudard, E.; Roy, F.; Bakhouya, M. Optimal Management of Thermal Comfort and Driving Range in Electric Vehicles. *Energies* **2020**, *13*, 4471. [\[CrossRef\]](#)
- Desreveaux, A.; Bouscayrol, A.; Castex, E.; Trigui, R.; Hittinger, E.; Sirbu, G.-M. Annual Variation in Energy Consumption of an Electric Vehicle Used for Commuting. *Energies* **2020**, *13*, 4639. [\[CrossRef\]](#)
- Basciotti, D.; Dvorak, D.; Gellai, I. A Novel Methodology for Evaluating the Impact of Energy Efficiency Measures on the Cabin Thermal Comfort of Electric Vehicles. *Energies* **2020**, *13*, 3872. [\[CrossRef\]](#)
- Wang, Y.; Gao, Q.; Zhang, T.; Wang, G.; Jiang, Z.; Li, Y. Advances in integrated vehicle thermal management and numerical simulation. *Energies* **2017**, *10*, 1636. [\[CrossRef\]](#)
- Shojaei, S.; Robinson, S.; McGordon, A.; Marco, J. Passengers vs. Battery: Calculation of Cooling Requirements in a PHEV. *SAE Tech. Pap.* **2016**, *2016*. [\[CrossRef\]](#)
- Titov, G.; Aaron Lustbader, J. Modeling Control Strategies and Range Impacts for Electric Vehicle Integrated Thermal Management Systems with MATLAB/Simulink. In Proceedings of the WCX17: SAE World Congress Experience, Detroit, MI, USA, 4–6 April 2017.
- Chowdhury, S.; Leitzel, L.; Zima, M.; Santacesaria, M. Total Thermal Management of Battery Electric Vehicles (BEVs). *SAE Tech. Pap.* **2018**. [\[CrossRef\]](#)
- Wu, W.; Wang, S.; Wu, W.; Chen, K.; Hong, S.; Lai, Y. A critical review of battery thermal performance and liquid based battery thermal management. *Energy Convers. Manag.* **2019**, *182*, 262–281. [\[CrossRef\]](#)
- Arasu, M.; Ahmed, Q.; Rizzoni, G. Optimizing battery cooling system for a range extended electric truck. *SAE Tech. Pap.* **2019**, *2019*, 1–9. [\[CrossRef\]](#)

17. Kong, D.; Peng, R.; Ping, P.; Du, J.; Chen, G.; Wen, J. A novel battery thermal management system coupling with PCM and optimized controllable liquid cooling for different ambient temperatures. *Energy Convers. Manag.* **2020**, *204*, 112280. [[CrossRef](#)]
18. Davin, T.; Pellé, J.; Harmand, S.; Yu, R. Experimental study of oil cooling systems for electric motors. *Appl. Therm. Eng.* **2015**, *75*, 1–13. [[CrossRef](#)]
19. Fang, G.; Yuan, W.; Yan, Z.; Sun, Y.; Tang, Y. Thermal management integrated with three-dimensional heat pipes for air-cooled permanent magnet synchronous motor. *Appl. Therm. Eng.* **2019**, *152*, 594–604. [[CrossRef](#)]
20. Huang, J.; Naini, S.S.; Miller, R.; Rizzo, D.; Sebeck, K.; Shurin, S.; Wagner, J. A Hybrid Electric Vehicle Motor Cooling System—Design, Model, and Control. *IEEE Trans. Veh. Technol.* **2019**, *68*, 4467–4478. [[CrossRef](#)]
21. Gamma Technologies | The Standard in Multi-Physics System Simulation. Available online: <https://www.gtisoft.com/> (accessed on 30 October 2020).
22. MathWorks—Makers of MATLAB and Simulink—MATLAB and Simulink. Available online: <https://www.mathworks.com/> (accessed on 30 October 2020).
23. Tribioli, L.; Chiappini, D.; Vukotić, M.; Miljavec, D. Performance Evaluation of an Electric Vehicle with Multiple Electric Machines for Increased Overall Drive Train Efficiency. *SAE Tech. Pap.* **2019**. [[CrossRef](#)]
24. Zheng, J.; Zhao, W.; Lee, C.H.T.; Ji, J.; Xu, G. Improvement torque performances of interior permanent-magnet machines. *CES Trans. Electr. Mach. Syst.* **2019**, *3*, 12–18. [[CrossRef](#)]
25. Rizzoni, G.; Guzzella, L.; Baumann, B.M. Unified modeling of hybrid electric vehicle drivetrains. *IEEE/ASME Trans. Mechatron.* **1999**, *4*, 246–257. [[CrossRef](#)]
26. Lee, S.; Cherry, J.; Safoutin, M.; McDonald, J.; Olechiw, M. Modeling and Validation of 48V Mild Hybrid Lithium-Ion Battery Pack. *SAE Int J. Altern. Powertrains* **2018**, *7*. [[CrossRef](#)]
27. REFPROP | NIST. Available online: <https://www.nist.gov/srd/refprop> (accessed on 30 October 2020).

Article

Digging Trajectory Optimization for Cable Shovel Robotic Excavation Based on a Multi-Objective Genetic Algorithm

Qiushi Bi ¹, Guoqiang Wang ¹, Yongpeng Wang ^{2,3}, Zongwei Yao ^{1,4,*} and Robert Hall ^{5,*}

¹ School of Mechanical and Aerospace Engineering, Jilin University, Changchun 130025, China; bqs@jlu.edu.cn (Q.B.); wggq@jlu.edu.cn (G.W.)

² Taiyuan Heavy Industry Co., LTD., Taiyuan 030024, China; wyp1989318@163.com

³ State Key Laboratory of Mining Equipment and Intelligent Manufacturing, Taiyuan 030024, China

⁴ Key Laboratory of CNC Equipment Reliability, Ministry of Education, Changchun 130025, China

⁵ School of Mining and Petroleum Engineering, University of Alberta, Edmonton, AB T6G 2H5, Canada

* Correspondence: yzw@jlu.edu.cn (Z.Y.); rhall1@ualberta.ca (R.H.)

Received: 12 May 2020; Accepted: 11 June 2020; Published: 16 June 2020

Abstract: As one of the most essential earth-moving equipment, cable shovels significantly influence the efficiency and economy in the open-pit mining industry. The optimal digging trajectory planning for each cycle is the base for achieving effective and energy-saving operation, especially for robotic excavation, in which case, the digging trajectory can be precisely tracked. In this paper, to serve the vision of cable shovel automation, a two-phase multi-objective genetic algorithm was established for optimal digging trajectory planning. To be more specific, the optimization took digging time and energy consumption per payload as objects with the constraints of the limitations of the driving system and geometrical conditions. The WK-55-type cable shovel was applied for the validation of the effectiveness of the multi-objective optimization method for digging trajectories. The digging performance of the WK-55 cable shovel was tested in the Anjialing mining site to establish the constraints. Besides, the digging parameters of the material were selected based on the tested data to make the optimization in line with the condition of the real digging operations. The optimization results for different digging conditions indicate that the digging time decreased from an average of 20 s to 10 s after the first phase optimization, and the energy consumption per payload reduced by 13.28% after the second phase optimization, which validated the effectiveness and adaptivity of the optimization algorithm established in this paper.

Keywords: digging trajectory; cable shovel; robotic excavation; multi-objective genetic algorithm

1. Introduction

A cable shovel is one of the key equipment in the open-pit mining industry traditionally operated by trained operators [1]. Abundant research results indicate that human factors have become a main factor inducing maintenance cost and reliability risk [2,3]. Current shovels with larger bucket capacity bring the benefit of lower digging cost, but higher operational difficulty, which makes the concept of robotic excavation a practical option for effective and steady digging processes.

Rational planning of digging trajectory is the base for robotic excavation. Awuah-Offei K. et al. optimized the hoist and crowd speed of a P&H 2100b cable shovel based on the Balovnev model with the objective of minimizing the unit payload energy consumption [4]. Dunbabin M. et al. designed an operation assistant system for cable shovels, which can help the driver plan the digging trajectory and predict the bucket fullness [5]. Wei B. et al. came up with a three degree of freedom (DOF) working mechanism of a cable shovel with an optimal design of the handle structure with the goal of

minimizing the unit payload energy consumption [6]. Wang X. et al. established a digging resistant force model, based on which the digging trajectory of a cable shovel was optimized with a result described by the curves of hoist and crowd velocities [7]. The unit payload energy consumption is commonly taken as the object in digging trajectory optimization. However, the digging efficiency is also a critical factor influencing cable shovel operations, especially for shovels with large bucket capacity. Hence, a multi-objective optimization algorithm should be applied for optimal digging trajectory planning.

Different multi-objective optimization algorithms have been widely used in the design of earth-moving machinery. Xu G. et al. applied the improved multi-objective evolutionary algorithm (MOEA) for TriPower shovel attachment working performance optimization [8]. Jang G. et al. applied the genetic algorithm (GA) on trajectory optimization of the hydraulic excavator for the optimization of energy consumption and the total length of the dig trajectory [9]. Yu X. et al. optimized the design of the bucket of a hydraulic excavator by solving a multi-objective problem, achieving a light-weight and high-strength product [10]. Feng H. et al. focused on the task of precise control of the hydraulic excavator using multi-objective genetic algorithm optimization [11]. Li X. et al. improved the digging efficiency of the hydraulic excavator by optimization of the working mechanism based on the algorithm of parallel PSO [12]. Kim J.-W. et al. optimized the working performance of the hydraulic excavator for multiple objects through the hybrid Taguchi random coordinate search algorithm [13]. Barakat N. and Sharma D. provided an optimal design method for the bulldozer blade based on the evolutionary multi-objective optimization algorithm [14]. Masih-Tehrani M. and Ebrahimi-Nejad S. combined the genetic algorithm and integer linear programming technique for multi-objective optimization of the powertrain of the bulldozer [15]. Zhang Z. and He B. developed a multi-objective optimization platform for wheel loader working mechanism design [16]. Cao B-w. et al. applied a genetic algorithm for multi-objective optimization of the stroke difference for wheel loaders [17].

Compared with other earth-moving equipment, the digging performance of the cable shovel is more difficult to predict because of the huge bucket capacity and the complex digging condition. Hence, optimal planning of the digging trajectory appears to be more necessary for each operation cycle of the cable shovel. In this paper, taking digging time and energy consumption per payload as objects, a two-phase multi-objective optimization based on genetic algorithms is applied for planning a practical digging trajectory with an equal value of the soil cutting angle. The research background is introduced in the first part of this paper. The second part explains how the digging trajectory is generated. In the third part, the model of working performance is established, based on which the optimization procedure is accomplished in the fourth part. A cable shovel with a nominal dipper capacity of about 55 m³ (Type WK-55) is used for validation of the optimization method in the fifth part. Finally, conclusions are summarized in the last part.

2. Digging Trajectory of the Cable Shovel

According to the classic theory for cable shovel performance evaluation, the soil cutting condition should be kept the same during the whole digging process [18]. Therefore, the digging trajectory is traditionally designed as a logarithmic spiral curve, as shown in Figure 1.

The value of the digging angle δ remains the same when the tip of the shovel bucket tracks the logarithmic spiral curve. Based on the geometrical relationship explained in Figure 1a, the value of polar diameter ρ can be expressed as a function of polar angle φ through integral operation:

$$\frac{d\rho}{\rho \cdot d\varphi} = \cot \delta, \rho = \rho_0 \cdot e^{\varphi \cot \delta} \quad (1)$$

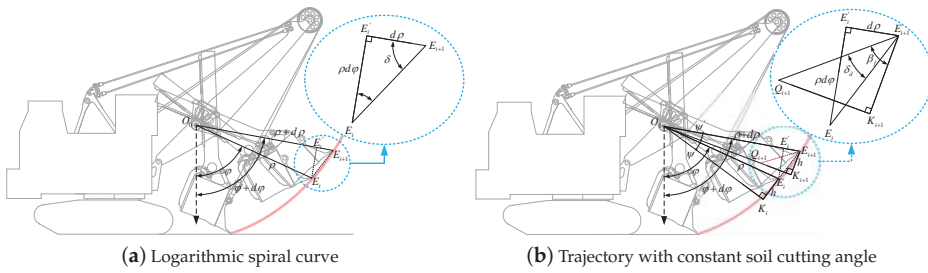


Figure 1. Theoretical digging trajectory for cable shovels.

The symbol ρ_0 indicates the initial value of the polar diameter when the digging process has started. As can be seen from Figure 1a, the digging angle δ cannot fully reflect the impact of the lip front. Therefore, as shown in Figure 1b, based on the logarithmic spiral curve, the curve with a constant value of cutting angle δ_d is developed:

$$\frac{d\rho}{\rho \cdot d\varphi} = \cot \left[\left(\frac{\pi}{2} - \psi' \right) - (\beta_f - \delta_d) \right], \rho = \frac{h}{c} \cdot (p_\rho \cdot e^{c \cdot \varphi_\rho} - 1) \tag{2}$$

where:

$$\begin{cases} p_\rho = 1 + c \cdot \left(\frac{\rho_0}{h} - \frac{h}{2 \cdot \rho_0} \right) \\ \varphi_\rho = \varphi - \arcsin \left(\frac{h}{\rho} \right) \\ c = \tan (\beta_f - \delta_d) \end{cases} \tag{3}$$

For the convenience of programming, the value of the angle ψ_i in iterative step i can be calculated using the value of the polar diameter in iterative step $i - 1$:

$$\psi_i = \frac{h}{\rho_{i-1}} \tag{4}$$

Combining Equations (2)–(4), the theoretical digging trajectory with a constant digging angle can be established by setting the value of the initial polar diameter ρ_0 and cutting angle δ_d .

Even though the curve with constant soil cutting angle δ_d can theoretically maintain the same digging condition, it is difficult to track this kind of digging trajectory practically. The working device of the cable shovel is a two DOF mechanism as shown in Figure 2. Corresponding to such a theoretical digging trajectory, either the hoist speed or the crowd speed changes from a non-zero value and ends up with another non-zero value. Taking the digging trajectory generated through the parameters shown in Table 1 as an example, the hoist speed curve and crowd speed curve are shown in Figure 3.

Table 1. Digging trajectory parameter: an example.

ρ_0 (m)	δ_d (degree)	φ (degree)	β_f (degree)	Dig Time t_D (s)
9.5	49.3	0–90	51.6	10.281

3.1. Kinematic Modeling

Establish the Cartesian coordinate system as shown in Figure 2. The polar diameter $\rho(t)$ corresponds to $l_{O_1O_2}(t)$, and the polar angle $\varphi(t)$ transforms into $\theta_1(t)$.

As shown in Figure 2, $v_{crowd} = l_{O_1O_2}$, the radius of the saddle block can be symbolized as r_1 . Based on the principle shown in Figure 4, the initial distance of l_{C_qC} can be symbolized as $l_{C_qC_0}$, and the angle of η_C can be calculated as $\eta_C = \arctan \frac{l_{C_qC_0} + l_{O_1O_2} \times t}{r_1 + H_C} - (\frac{\pi}{2} - \theta_1)$. Hence, the hoist speed can be calculated through the equations:

$$v_{hoist} = l_{O_0C} \times \dot{\theta}_1 \times \cos \beta_C - l_{O_1O_2} \times \cos \varepsilon_C \tag{5}$$

where:

$$\begin{cases} l_{O_0C} = \sqrt{(r_1 + H_C)^2 + (l_{C_qC_0} + l_{O_1O_2} \times t)^2} \\ \beta_C = \arcsin \left(\frac{R_{O_T}}{l_{O_T C}} \right) - \left[\frac{\pi}{2} - \arccos \frac{l_{O_0C}^2 + l_{O_T C}^2 - l_{O_0O_T}^2}{2 \times l_{O_0C} \times l_{O_T C}} \right] \\ l_{O_T C} = \sqrt{l_{O_0C}^2 + l_{O_0O_T}^2 - 2 \times l_{O_0C} \times l_{O_0O_T} \times \cos(\eta_C + \delta)} \\ \varepsilon_C = \arctan \left(\frac{l_{C_qC_0} + l_{O_1O_2} \times t}{r_1 + H_C} \right) + \beta_C \end{cases} \tag{6}$$

It is necessary to analyze the speed of the bucket tip for the purpose of confirming the direction of the digging force. Figure 5 shows the principle of the calculation:

$$\begin{cases} v_{Ea} = \sqrt{v_{Ee}^2 + l_{O_1O_2}^2 - 2 \times v_{Ee} \times l_{O_1O_2} \times \cos \varphi_E} \\ v_{Ea} = \sqrt{(r_1 + H_E)^2 + (l_{E_qE_0} + l_{O_1O_2} \times t)^2} \times \dot{\theta}_1 \\ \gamma_E = \arccos \left(\frac{v_{Ea}^2 + l_{O_1O_2}^2 - v_{Ee}^2}{2 \times v_{Ea} \times l_{O_1O_2}} \right) \end{cases} \tag{7}$$

where:

$$\varphi_E = \arctan \left(\frac{l_{E_qE_0} + l_{O_1O_2} \times t}{r_1 + H_E} \right) \tag{8}$$

The mass of the bucket-handle assembly for a large cable shovel cannot be ignored as it will cause non-negligible inertia force. The principle for the speed analysis is shown in Figure 5:

$$\begin{cases} v_{gax} = l_{O_1O_2} \times \cos \theta_1 + l_{O_0G} \times \dot{\theta}_1 \times \cos \eta_G \\ v_{gay} = l_{O_1O_2} \times \sin \theta_1 + l_{O_0G} \times \dot{\theta}_1 \times \sin \eta_G \end{cases} \tag{9}$$

where:

$$l_{O_0G} = \sqrt{(r_1 + H_G)^2 + (l_{G_qG_0} + l_{O_1O_2} \times t)^2} \tag{10}$$

Figure 6 explains the composition principle of acceleration:

$$a_{gax} = -a_{gen} \cdot \cos \eta_G + a_{get} \cdot \sin \eta_G + a_{gr} \cdot \cos \left(\frac{\pi}{2} - \varphi_G + \eta_G \right) \pm a_{gc} \cdot \cos(\varphi_G + \eta_G) \tag{11}$$

$$a_{gay} = a_{gen} \cdot \sin \eta_G + a_{get} \cdot \cos \eta_G - a_{gr} \cdot \sin \left(\frac{\pi}{2} - \varphi_G + \eta_G \right) \pm a_{gc} \cdot \sin(\varphi_G + \eta_G) \tag{12}$$

where:

$$a_{gen} = l_{O_0G} \cdot (\dot{\theta}_1)^2, a_{get} = l_{O_0G} \cdot \ddot{\theta}_1, a_{gr} = l_{O_1O_2} \cdot \ddot{\theta}_1, a_{gc} = 2 \cdot \dot{\theta}_1 \cdot l_{O_1O_2} \tag{13}$$

As can be seen in Equations (11) and (12), the Coriolis acceleration a_{gc} determines whether to take the positive sign or the negative sign for calculation.

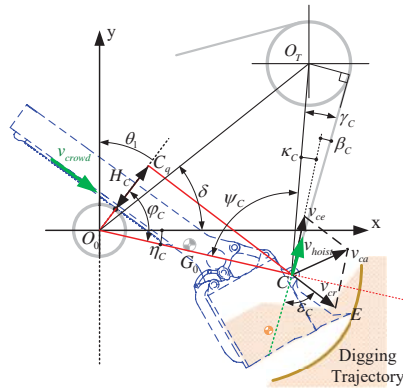


Figure 4. Hoist speed.

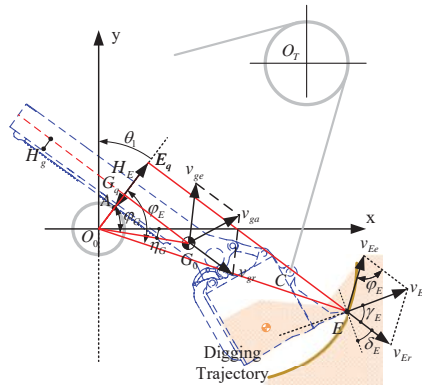


Figure 5. Speed of the bucket tip and handle.

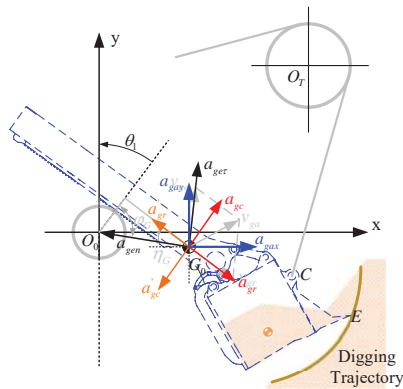


Figure 6. Acceleration of the bucket handle.

3.2. Power Consumption and Bucket Fullness

The forces applied to the bucket-handle assembly during the digging process are shown in Figure 7. The power consumption corresponding to the digging trajectory can be calculated based on the driven speed and applied forces. Figure 8 shows the principle of digging volume evaluation, which can be described as an integration process of the product between digging thickness and bucket width.

The digging forces acting on the tip of the bucket can be simplified as a tangential force and a normal force [18]. Generally, those two forces can be calculated as:

$$\begin{cases} F_{Et}(t) = K \cdot b \cdot c(t) \\ F_{En}(t) = \lambda \cdot F_{Et}(t) \end{cases} \quad (14)$$

Different kinds of material correspond to different digging performance even for the same digging trajectory. Theoretically, the digging resistant force can be simplified as one tangential force and one normal force acting on the bucket tip of the mining shovel when digging the material of sand, loam, gravel or clay. It should be noted that large number of boulders or oversized rocks would lead to significant fluctuation of digging force during the excavation, which makes it difficult to describe the digging process numerically. In Equation (14), the parameter K stands for the unit resistance to excavation whose value depends on the soil type [18], b for the width of the bucket, and $c(t)$ for the current cutting thickness of the soil. The multiplication of $b \cdot c(t)$ represents the area of the current digging cross-section. The parameter of λ in Equation (14) is the ratio between the tangential force and the normal force, whose value depends on the soil type and the service time of the bucket [18].

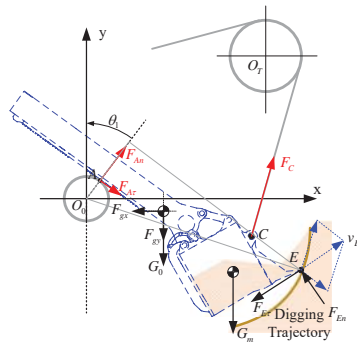


Figure 7. Digging forces' analysis.

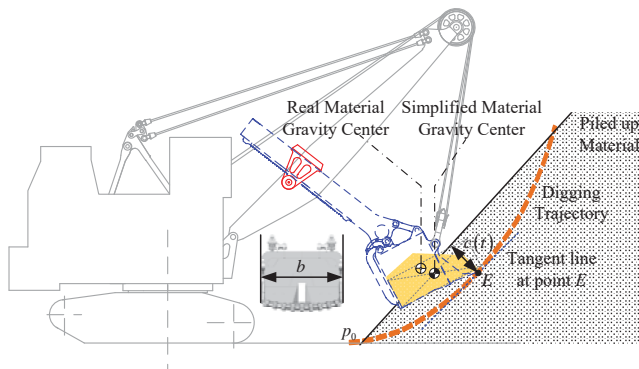


Figure 8. Digging material volume.

Taking advantage of D'Alembert's principle, the crowding force ($F_{crowd} = F_A$) and hoisting force ($F_{hoist} = F_C$) can be calculated based on the equilibrium condition shown in Figure 7. Accordingly, the following integral operations can be used for the calculation of energy consumption:

$$E_{hoist} = \int_{t_0}^{t_T} F_{hoist} \times v_{hoist} dt \quad (15)$$

$$E_{crowd} = \int_{t_0}^{t_T} F_{crowd} \times v_{crowd} dt \quad (16)$$

As shown in Figure 8, the excavated mass and the bucket fullness can be calculated as:

$$M_{dig} = \rho_{soil} \times b \times \int_{t_0}^{t_T} c(t) dt \quad (17)$$

$$Fullness_{bucket} = \frac{b \times \int_{t_0}^{t_T} c(t) dt}{V_{bucket}} \quad (18)$$

where the parameter ρ_{soil} stands for the bulk density of the excavated material.

Finally, the unit energy consumption per payload and unit digging time per payload can be calculated through the following equations:

$$E_M = \frac{E_{hoist} + E_{crowd}}{M_{dig}} \quad (19)$$

$$T_M = \frac{t_T - t_0}{M_{dig}} \quad (20)$$

4. Multi-Objective Optimization Procedure

For optimal digging trajectory planning for robotic excavation in each digging cycle, a kind of two-phase multi-objective optimization is applied for the maximum digging efficiency and minimum unit energy consumption. The first phase of optimization can be described as searching the optimal theoretical digging trajectory with a constant soil cutting angle. The second phase, however, is a process making the trajectory practical by optimizing the speed curves of driving systems.

More specifically, for each unique digging condition, the parameters describing the theoretical digging trajectory such as initial polar diameter ρ_0 , cutting angle δ_d , and digging time t_d are taken as variables in the first phase of optimization. Accordingly, the working performance and geometrical limitations are taken as constraints. The genetic algorithm is applied for the first phase of multi-objective optimization. Based on the optimized theoretical digging trajectory, four speed control moments are set up: t_1, t_2, t_3, t_4 . The time period $0 - t_1$ is an acceleration period, and the speed of both the hoisting and crowding system increase from zero with the value of acceleration rising from zero simultaneously. The time period $t_1 - t_2$ is also an acceleration period with the speed continuously increasing while the value of acceleration diminishes. Either the value of speed or acceleration matches the theoretical trajectory at the moment of t_2 . During the time period $t_2 - t_3$, both the speed and acceleration match with that of the theoretical trajectory. The time period $t_3 - t_4$ is a deceleration period, and both the hoist and crowd speed start decreasing with the value of deceleration rising from zero. The last time period $t_4 - t_d$ is also a deceleration period, and either the speed or the deceleration diminishes to zero at the moment t_d . Therefore, the second phase of optimization takes the four speed control moments as variables to make the theoretical digging trajectory practical and further decrease the unit energy consumption. The procedure of the two-phase digging trajectory optimization can be summarized as the flowchart shown in Figure 9.

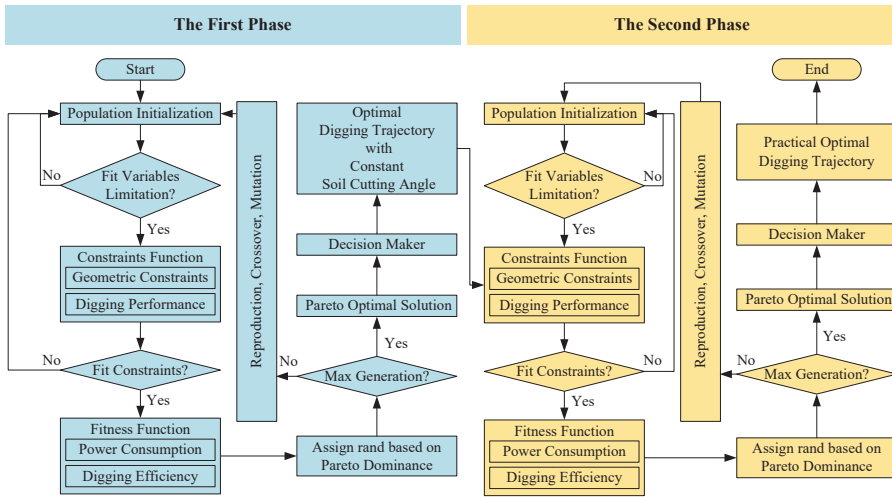


Figure 9. The two-phase multi-objective optimization of the digging trajectory based on the genetic algorithm.

4.1. First Phase Optimization

4.1.1. Variables and the Boundary Constraints

The variables in the first phase optimization are initial polar diameter ρ_0 , cutting angle δ_d , and digging time t_d . Generally, the boundary values of the variables are determined by structural and operational limits:

$$X_1 = [\rho_0, \delta_d, t_d] \tag{21}$$

$$\begin{cases} Lower_{X_1} = [\rho_{min}, \delta_{dmin}, t_{digmin}] \\ Lower_{X_1} = [\rho_{max}, \delta_{dmax}, t_{digmax}] \end{cases} \tag{22}$$

4.1.2. Fitness Function for Multi-Objective Optimization

In order to make the working performance of unit energy consumption and unit digging time fitness functions applied in the multi-objective genetic algorithm, the parameters of rated hoisting power P_h , rated crowding power P_c , standard digging time t_{ST} , and rated digging mass M_{SAE} are applied for the normalization process:

$$\begin{cases} Fitness_1(X_1) = \max \left[\frac{(P_h + P_c) \times t_{ST} / M_{SAE}}{E_M(X_1)} \right] \\ Fitness_2(X_1) = \max \left[\frac{t_{ST} / M_{SAE}}{T_M(X_1)} \right] \end{cases} \tag{23}$$

4.1.3. Constraints

The constraints applied in the first phase of optimization can be summarized as two main kinds: geometrical and performance constraints.

The geometrical constraints can be listed as:

- The position of the bucket should be above the material pile when the digging process finishes:

$$\begin{cases} g_1(X_1) = y_{slope_{tip}}(X_1) - y_{bucket_{tip}}(X_1) < 0 \\ g_2(X_1) = y_{slope_{bot}}(X_1) - y_{bucket_{bot}}(X_1) < 0 \end{cases} \quad (24)$$

In Equation (24), the parameter $y_{slope_{tip}}$ stands for the height of the material piled-up slope corresponding to the bucket tip, while the parameter of $y_{slope_{bot}}$ indicates the slope height corresponding to the bucket bottom. Similarly, the parameter of $y_{bucket_{tip}}$ means the height of the bucket tip itself, while the parameter of $y_{bucket_{bot}}$ stands for the height of the bucket bottom.

- The length of the polar diameter should be within the limitation when the digging process finishes:

$$g_3(X_1) = \rho_{stop}(X_1) - \rho_{lim} < 0 \quad (25)$$

In Equation (25), the parameter ρ_{stop} stands for the length of the polar diameter when the digging process finishes, while the parameter ρ_{lim} means the maximum length of the polar diameter.

The performance constraints can be listed as:

- The highest hoist speed during the digging process $v_{hoist_{max}}$ should be smaller than the rated value $v_{hoist_{lim}}$. Similarly, the highest crowd speed $v_{crowd_{max}}$ should not exceed the boundary value of $v_{crowd_{lim}}$ as well.

$$\begin{cases} g_4(X_1) = v_{hoist_{max}}(X_1) - v_{hoist_{lim}} < 0 \\ g_5(X_1) = v_{crowd_{max}}(X_1) - v_{crowd_{lim}} < 0 \end{cases} \quad (26)$$

- The highest hoist force during the digging process $F_{hoist_{max}}$ should be smaller than the rated value $F_{hoist_{lim}}$. Similarly, the highest crowd force $F_{crowd_{max}}$ should not exceed the boundary value of $F_{crowd_{lim}}$ as well.

$$\begin{cases} g_6(X_1) = F_{hoist_{max}}(X_1) - F_{hoist_{lim}} < 0 \\ g_7(X_1) = F_{crowd_{max}}(X_1) - F_{crowd_{lim}} < 0 \end{cases} \quad (27)$$

- The highest hoist power during the digging process $P_{hoist_{max}}$ should be smaller than the rated value $P_{hoist_{lim}}$. Similarly, the highest crowd power $P_{crowd_{max}}$ should not exceed the boundary value of $P_{crowd_{lim}}$ as well.

$$\begin{cases} g_8(X_1) = P_{hoist_{max}}(X_1) - P_{hoist_{lim}} < 0 \\ g_9(X_1) = P_{crowd_{max}}(X_1) - P_{crowd_{lim}} < 0 \end{cases} \quad (28)$$

- An extreme large value of bucket fullness would result in the overload of the power system. In other words, the maximum value of the bucket fullness has already been limited by the constraints of digging power. Hence, the bucket fullness should meet the minimum requirement when the digging process finishes:

$$g_{10}(X_1) = Fullness_{bucket_{lim}} - Fullness_{bucket}(X_1) < 0 \quad (29)$$

4.2. Second Phase Optimization

4.2.1. Variables and the Boundary Constraints

In the second phase of optimization, the variables change into the four speed control moments:

$$X_2 = [t_1, t_2, t_3, t_4] \quad (30)$$

The boundary values of the variables can be described as:

$$\begin{cases} Lower_{X_2} = [t_{1min}, t_{2min}, t_{3min}, t_{4min}] \\ Lower_{X_2} = [t_{1max}, t_{2max}, t_{3min}, t_{4max}] \end{cases} \quad (31)$$

4.2.2. Fitness Function for Multi-Objective Optimization

The fitness functions for the second phase of optimization are similar to the first phase. However, it should be noted that the digging trajectory in the second phase of optimization is calculated through the hoist and crowd speed while directly through the variables in the first phase:

$$\begin{cases} Fitness_1 (X_2) = \max \left[\frac{(P_h + P_c) \times t_{ST} / M_{SAE}}{E_M (X_2)} \right] \\ Fitness_2 (X_2) = \max \left[\frac{t_{ST} / M_{SAE}}{T_M (X_2)} \right] \end{cases} \quad (32)$$

4.2.3. Constraints

The constraints applied in the second phase of optimization can be divided into two groups: the same constraints used in the first phase, which can be described as $g_1 (X_2) \sim g_{10} (X_2)$, and the unique constraints for the second phase. For geometrical constraints, the limitation for the initial digging point is added to avoid deep insertion into the material at the beginning of the digging process.

$$g_{1a} (X_2) = y_{0slope} (X_2) - y_{0bucket} (X_2) < 0 \quad (33)$$

In Equation (33), the parameter y_{0slope} stands for the height of the material slope corresponding to the bucket tip, while the parameter $y_{0bucket}$ indicates the height of the bucket tip itself.

For the performance constraints, the unique requirements for the speed curve and acceleration curve are taken into consideration.

- At the moment of t_d , both the speed and acceleration for the driving system equal zero:

$$\begin{cases} g_{2a} (X_2) = v_{hoist_{t_d}} (X_2) = 0 \\ g_{3a} (X_2) = v_{crowd_{t_d}} (X_2) = 0 \\ g_{4a} (X_2) = a_{hoist_{t_d}} (X_2) = 0 \\ g_{5a} (X_2) = a_{crowd_{t_d}} (X_2) = 0 \end{cases} \quad (34)$$

- At the moment of t_1 and t_4 , the speed and acceleration for the driving system are continuous:

$$\begin{cases} g_{6a} (X_2) = v_{hoist_{t_i-B}} (X_2) - v_{hoist_{t_i-A}} (X_2) = 0 \\ g_{7a} (X_2) = v_{crowd_{t_i-B}} (X_2) - v_{crowd_{t_i-A}} (X_2) = 0 \\ g_{8a} (X_2) = a_{hoist_{t_i-B}} (X_2) - a_{hoist_{t_i-A}} (X_2) = 0 \\ g_{9a} (X_2) = a_{crowd_{t_i-B}} (X_2) - a_{crowd_{t_i-A}} (X_2) = 0 \\ i = 1, 4 \end{cases} \quad (35)$$

In Equation (35), the subscript ' - B' represents the parameter value calculated from the time period t_{i-1} to t_i , while the subscript ' - A' for the time period t_i to t_{i+1} .

- At the moment of t_2 and t_3 , the speed and acceleration for the driving system are continuous, and the parameters of movements match the theoretical digging trajectory.

$$\begin{cases} g_{10a}(X_2) = v_{hoist_{t_j}}(X_2) - v_{hoist_{t_j-theory}}(X_2) = 0 \\ g_{11a}(X_2) = v_{crowd_{t_j}}(X_2) - v_{crowd_{t_j-theory}}(X_2) = 0 \\ g_{12a}(X_2) = a_{hoist_{t_j}}(X_2) - a_{hoist_{t_j-theory}}(X_2) = 0 \\ g_{13a}(X_2) = a_{crowd_{t_j}}(X_2) - a_{crowd_{t_j-theory}}(X_2) = 0 \\ g_{14a}(X_2) = \rho_{t_j}(X_2) - \rho_{t_j-theory}(X_2) = 0 \\ j = 2, 3 \end{cases} \quad (36)$$

- The maximum acceleration should be limited in a certain range according to the driving system.

$$\begin{cases} g_{15a}(X_2) = a_{hoist_{max}}(X_2) - a_{hoist_{lim}} < 0 \\ g_{16a}(X_2) = a_{crowd_{max}}(X_2) - a_{crowd_{lim}} < 0 \end{cases} \quad (37)$$

4.3. Optimization Method

The multi-objective genetic algorithm (MOGA) was applied in either of the two periods of optimization. The MOGA toolbox provided with the MATLAB (R2019a, MathWorks, Natick, MA, USA) software was used for the calculation. After getting the Pareto solution set, the digging time was taken as an indicator for choosing the optimal result. Based on the optimization results, the digging trajectory was generated with the digging performance numerically evaluated. The optimization method should be taken in various situations to validate the efficiency.

5. Case Study

In order to validate the efficiency of the two-phase optimization method, the cable shovel with the nominal dipper capacity of about 55 m³ (Type WK-55) was used in this research for optimal digging trajectory planning. It was important to determine the constraint's boundaries before the optimization. Therefore, field tests were performed to get the limitations of the working performance.

5.1. Digging Performance Field Test

Considering the digging efficiency, the experienced operators of cable shovels could make the digging operation faster with a higher value of the bucket fullness, which makes the shovel power fully loaded or overloaded during the digging process. Field tests were performed at the Anjialing open-pit coal mining site (Shanxi Province, China), as shown in Figure 10a. The digging performance corresponding to the digging trajectory was recorded through the DAQ system (data acquisition system).

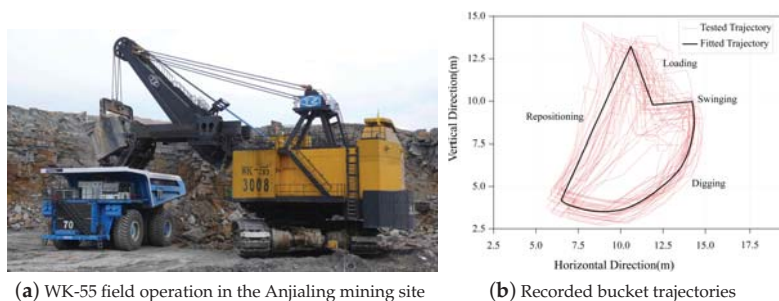


Figure 10. WK-55-type cable shovel field tests.

As can be seen from Figure 10b, the digging trajectories were discrete when the equipment was operated by the operators. The corresponding performance boundaries are listed in Table 2.

Table 2. The tested digging performance boundaries.

No.	Tested Parameters	Unit	Hoist System	Crowd System
1	Maximum torque of a single driven motor	N·m	33,695	9356
2	Maximum force of a single driven motor	kN	1987	1002
3	Maximum speed of a single driven motor	rpm	930	772
4	Maximum power of a single driven motor	kW	1735	754
5	Average time of a digging cycle	s	20	20
6	Minimum time of a digging cycle	s	15	15
7	Maximum mechanism acceleration	m/s ²	0.8	0.5
8	Maximum mechanism velocity	m/s	1.76	0.76

The performance constraints applied for optimization could be established based on the data shown in Table 2 with the value of the overload ratio taken into consideration. Similarly, it was necessary to numerically describe the digging condition to set up the geometrical constraints for the optimization.

5.2. Digging Conditions

The digging pattern for cable shovels could be described as two main steps: Firstly, the equipment stayed at a fixed place for several digging cycles until digging conditions could not meet the operation requirements. Secondly, the cable shovel moved to the next fixed place and repeated the digging process as described in the first step. Hence, the parameters describing the digging condition should be defined in the same coordinate attached to the cable shovel. As shown in Figure 11a, under the circumstances that the profile of the piled-up material was simplified as a straight line, different digging conditions could be described as different combinations of slope angle δ_m and digging distance d_m . Generally, the value of the slope angle ranges from 37° to 42° for blasted rock. However, for the digging distance, the minimum value should keep the tip of the bucket from not contacting the material slope. The structural parameters of the WK-55-type cable shovel are explained in Figure 11b and listed in Table 3.

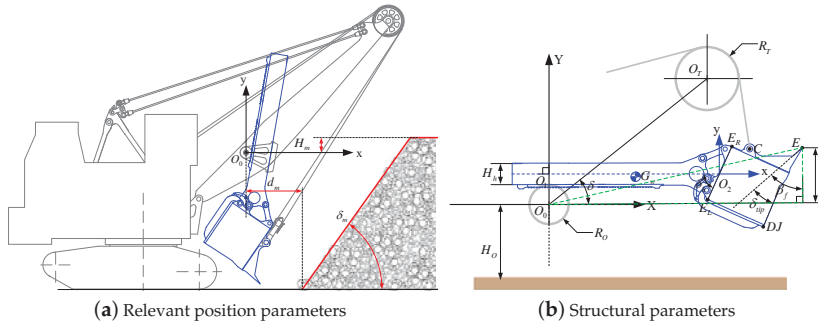


Figure 11. Digging conditions.

Table 3. Structural parameters of the WK-55 cable shovel working device.

H_h (m)	H_o (m)	R_o (m)	R_T (m)	h (m)	β_f (degree)	δ (degree)	δ_h (degree)	δ_{tip} (degree)
1.37	10.14	0.368	1.11	2.35	51.7	44.4	60.9	6.8

Additionally, the material parameters should be chosen carefully to evaluate the digging force and other digging performance rationally. On the basis of the tested data gained from the Anjialing mining site, the parameters indicating digging force are determined with the combination of the measured trajectories to make the optimization process stay in line with the real digging condition. The parameters of the excavated material in the Anjialing mining site, as well as the parameters of the WK-55 shovel bucket are listed in Table 4.

Table 4. Material property and WK-55 bucket parameters.

ρ_{soil} (kg/m ³)	K (kpa)	λ	b (m)	V_{bucket} (m ³)	M_{handle} (kg)	M_{bucket} (kg)
1700	225	0.45	4.86	58	42,514	84,421

5.3. First Phase Optimization

In the first phase optimization, the digging conditions were divided into two main categories according to the different profiles of the piled-up material: the flat surface, which could be described using a slope angle, and the curved surface defined by groups of coordinate values.

5.3.1. Material Piled up with a Flat Surface

As listed in Table 5, five different digging conditions were set up for the first phase digging trajectory optimization.

Table 5. Parameters describing digging conditions.

Digging Condition Number	δ_m (degree)	d_m (m)
Condition I	40	2.5
Condition II	40	3.5
Condition III	40	4.5
Condition IV	37	2.5
Condition V	43	2.5

Optimizations were accomplished though using MATLAB. Taking the digging condition I (digging distance set to 2.5 m and the slope angle set to 40°) as an example, the Pareto results are shown in Figure 12a, and the corresponding distribution of the variables is shown in Figure 12b.

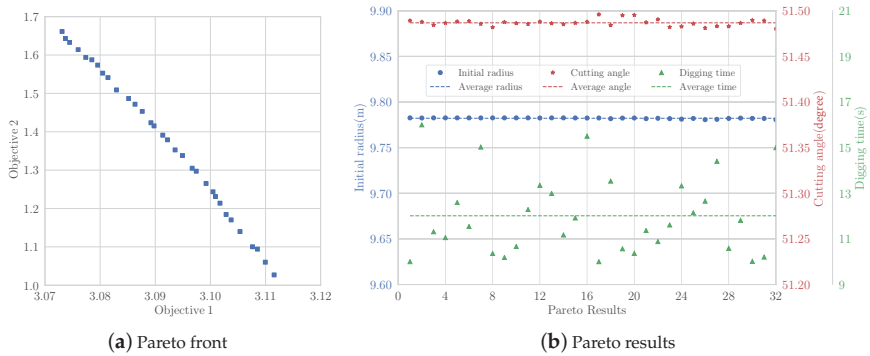


Figure 12. First phase optimization results for Condition I.

As shown in Figure 12b, the design variables of the initial polar diameter and soil cutting angle converged to a concentrated interval with the individual values slightly fluctuating around the average value. However, the design variable of digging time was distributed around the average value discretely. Hence, the digging time was taken as the indicator for deciding the optimal combination of the design variables based on the Pareto results. Similarly, the first phase optimizations were applied to the other four digging conditions with the optimal results listed in Table 6.

Table 6. First phase optimization results for all five digging conditions.

Digging Condition	ρ_0 (m)	δ_d (degree)	t_{dig} (s)	$F_{hoist,max}$ (kN)	$F_{crowd,max}$ (kN)	$P_{hoist,max}$ (kW)	$P_{crowd,max}$ (kW)	Fullness	E/M (J/kg)
I	9.78	51.5	10.02	3487.42	860.08	3218.10	265.08	0.9598	271.2458
II	9.96	48.5	10.04	3497.75	882.96	3524.60	351.20	0.9603	284.1154
III	10.02	45.1	10.11	3489.99	915.91	3683.09	452.16	0.9481	296.8358
IV	9.95	49.8	10.07	3492.24	913.31	3311.64	327.52	1.0126	268.8554
V	9.52	51.1	10.04	3498.95	749.14	3180.14	237.15	0.8995	274.8638

Comparing the data listed in Tables 2 and 6, the digging parameters applied in the first phase optimization were set the same as the real tested area in the Anjialing mining site, and after the first phase optimization, the digging time of all five digging conditions decreased dramatically from the minimum of 15 s to an average of about 10 s. Besides, different digging conditions slightly affected the optimization result of bucket fullness, which stably stayed above 0.9. The data listed in Table 6 indicated that the different digging conditions had a different influence on the optimization results. With the same digging distance, when the value of the slope angle increased, the optimal initial polar diameter became shorter, while the soil cutting angle almost remained the same. However, the optimal cutting angle kept decreasing while the initial polar diameter barely changed when the digging distance increased with a constant value of the slope angle. Additionally, the unit energy consumption per payload increased with the digging distance, as well as the slope angle. Hence, in general, under the condition that the materials had similar properties and a regular particle size distribution, the digging distance influenced the digging operation more significantly than the slope angle.

5.3.2. Material Piled up with a Curved Surface

Even in the ideal digging conditions, it was difficult to guarantee that every piled-up material profile could be simplified as a flat surface using a value of the slope angle for the description. In order to keep in line with the same diggability of the material in the Anjialing mining site, the same values of the digging parameters were applied. Hence, based on a slope angle of 40°, four curved profiles were established

representing four typical concave-convex conditions. For each curved profile, three digging distance were applied for digging trajectory optimization, as shown in Figure 13.

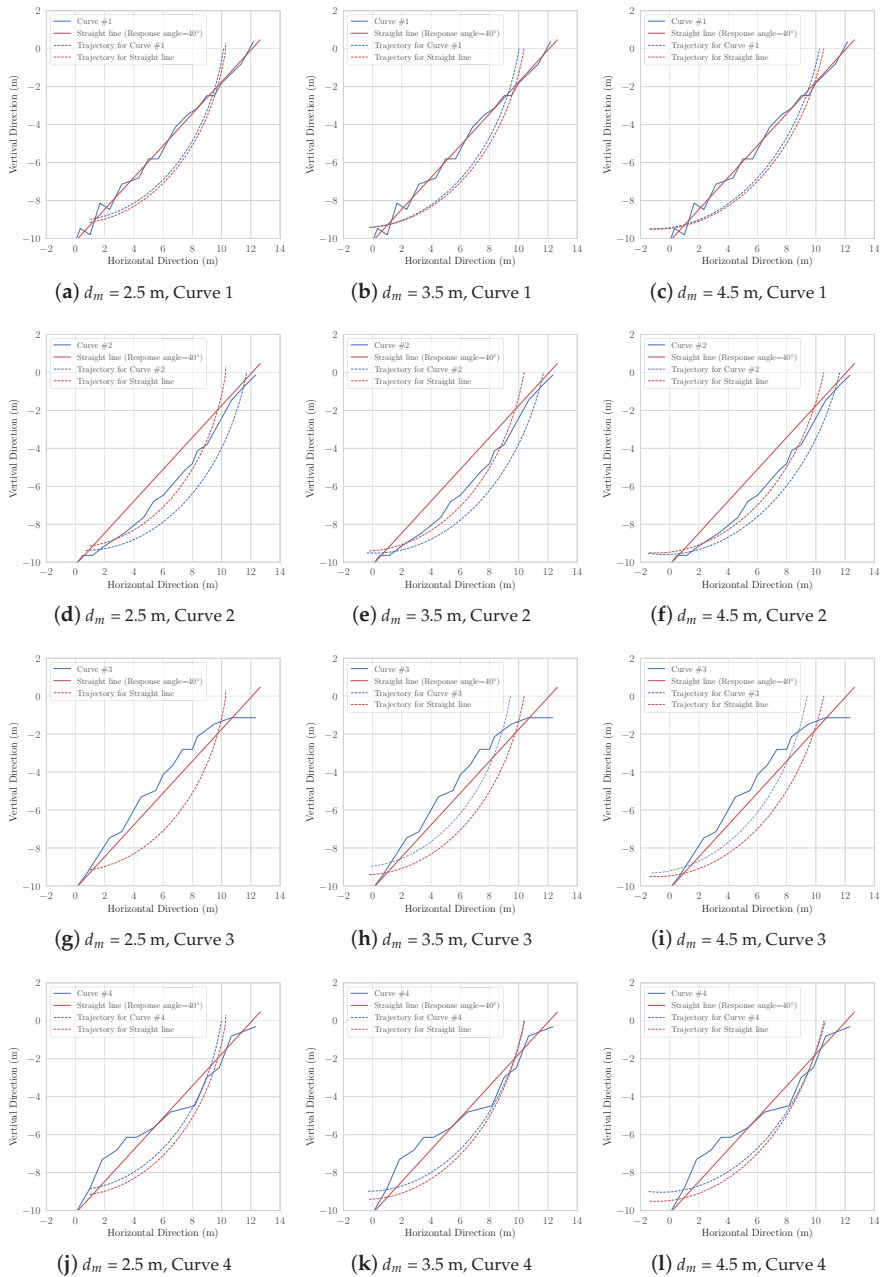


Figure 13. Digging trajectories for Curves 1–4: first phase optimization.

It can be seen from Figure 13 that the profile of piled-up material dramatically influenced the optimization results. In other words, the optimization method established in this research could adapt to various digging conditions. The digging performance comparisons between the optimal digging trajectories for different piled-up material profiles are listed in Table 7.

Table 7. Digging performance comparison between digging trajectories: first phase optimization.

Digging Distance $d_m = 2.5$ m							
Material Pile	ρ_0 (m)	δ_d (degree)	t_{dig} (s)	$P_{hoist_{max}}$ (kW)	$P_{crowd_{max}}$ (kW)	Fullness	E/M (J/kg)
Curve 1	9.64	51.5	10.00	3146.10	235.08	0.8427	277.0546
Curve 2	9.91	47.5	10.01	3434.60	338.74	0.9442	293.3497
Curve 3	–	–	–	–	–	–	–
Curve 4	9.50	51.5	10.00	2426.30	367.74	0.8047	266.2236
Straight Line	9.78	51.5	10.02	3218.10	265.08	0.9598	271.2458
Digging Distance $d_m = 3.5$ m							
Material Pile	ρ_0 (m)	δ_d (degree)	t_{dig} (s)	$P_{hoist_{max}}$ (kW)	$P_{crowd_{max}}$ (kW)	Fullness	E/M (J/kg)
Curve 1	10.02	49.8	10.02	3419.90	287.18	0.8461	292.0918
Curve 2	9.98	44.6	10.00	3922.00	390.78	0.8598	312.9045
Curve 3	9.58	50.2	10.00	3480.90	340.32	0.8514	286.4528
Curve 4	9.53	46.8	10.01	2813.40	528.62	0.8630	278.2105
Straight Line	9.96	48.5	10.04	3524.60	351.20	0.9603	284.1154
Digging Distance $d_m = 4.5$ m							
Material Pile	ρ_0 (m)	δ_d (degree)	t_{dig} (s)	$P_{hoist_{max}}$ (kW)	$P_{crowd_{max}}$ (kW)	Fullness	E/M (J/kg)
Curve 1	10.00	45.9	10.03	3695.70	398.55	0.8298	308.2182
Curve 2	10.04	42.0	10.00	3674.60	426.56	0.7150	348.2000
Curve 3	9.87	48.1	10.10	3756.90	426.98	0.8459	302.7920
Curve 4	9.50	42.9	10.04	3007.60	673.70	0.8524	291.8544
Straight Line	10.02	45.1	10.11	3683.09	452.16	0.9481	296.8358

Combining the data listed in Table 7 and the information shown in Figure 13, the relationship between the piled-up material profile and the optimal digging trajectory could be summarized into the following aspects: For Curve 2 and Curve 3, the curved profile entirely stayed above or beneath the 40° slope line, and the corresponding digging trajectories moved forward and backward accordingly. It should be noted that, for Curve 3, there did not exist an optimal digging trajectory for the case with the digging distance of 2.5 m, which indicated that there was no optimal result fitting the constraints if the cable shovel stayed too close to the material pile. Similarly, the digging trajectories corresponding to Curve 1 appeared close to those optimized for the 40° slope line because the curve itself just fluctuated slightly around the line. For Curve 4, however, the optimization made the digging trajectory fill the bucket during the early period of excavation, which matched with the character of this curve and reduced the energy consumption per payload.

The results indicated that the first phase optimization could adapt to different digging conditions. Although the digging conditions set in this research for digging trajectory optimization could not cover all kinds of operational demands, the optimal results could prove the validity of the optimization to some extent.

5.4. Second Phase Optimization

Based on the results of the first phase optimization, the second phase optimization was carried out to enhance the executability of the excavation process while improving the digging performance.

Taking the digging for Condition I as an example, the comparison between the results of the first and second phase optimization are shown in Figure 14.

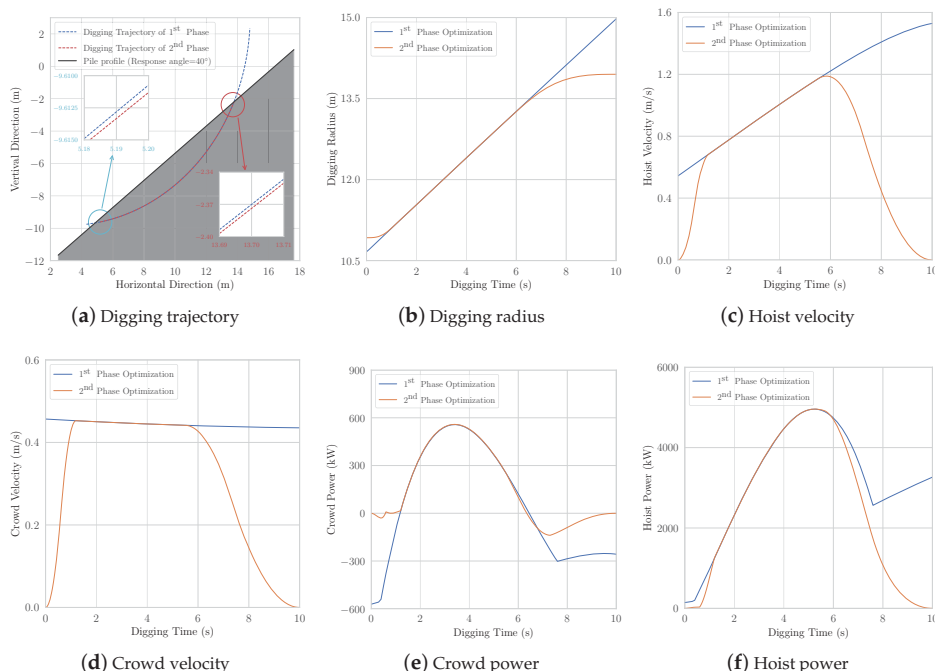


Figure 14. Digging performance comparison between two phases of optimization: an example.

As can be seen from Figure 14a, the total length of the digging trajectory reduced significantly after the second phase optimization, while the shape of the trajectory mostly retained the result of the first phase optimization with a slight difference that appeared at both ends of the trajectory. It is also clearly shown in Figure 14a that after the second phase of optimization, the digging process stopped right after the shovel bucket totally moved above the material slope. As the cable shovels are usually switched to swing cycle after the digging cycle, it might help prevent the shovel bucket from hitting the bench face for the operators to hoist the bucket much higher than the material pile, but that is not necessary for robotic excavations. Hence, the trajectory from the second phase optimization was more reasonable than the result of the first phase optimization. Besides, the constraints applied in the second phase of optimization ensured the smooth change of kinematic and performance parameters, which made the digging process more practical by reducing the impact force during the digging process. As shown in Figure 14b–f, either the speed or the power consumption of the driving system started and ended with the value of zero. The results of all digging conditions are listed in Table 8.

Table 8. The results of the second phase optimization.

Digging Condition	t_1 (s)	t_2 (s)	t_3 (s)	t_4 (s)	$F_{hoist,max}$ (kN)	$F_{crowd,max}$ (kN)	$P_{hoist,max}$ (kW)	$P_{crowd,max}$ (kW)	Fullness	E/M (J/kg)
I	0.4	1.2	6.5	9.6	3486.20	863.51	3217.63	266.09	0.9579	237.0699
II	1.0	2.4	6.9	9.6	3499.11	885.83	3527.50	352.32	0.9603	244.5252
III	2.1	3.7	8.1	9.5	3492.75	919.28	3642.87	453.80	0.9481	252.7828
IV	0.4	1.2	5.7	9.6	3489.84	918.27	3315.66	329.30	1.0126	226.4975
V	0.4	2.3	8.1	9.5	3499.98	751.05	3182.23	237.74	0.8995	250.0330

Combining the data listed in Tables 6 and 8, the comparison between the digging performance of the first and second phase optimization results is shown in Figure 15.

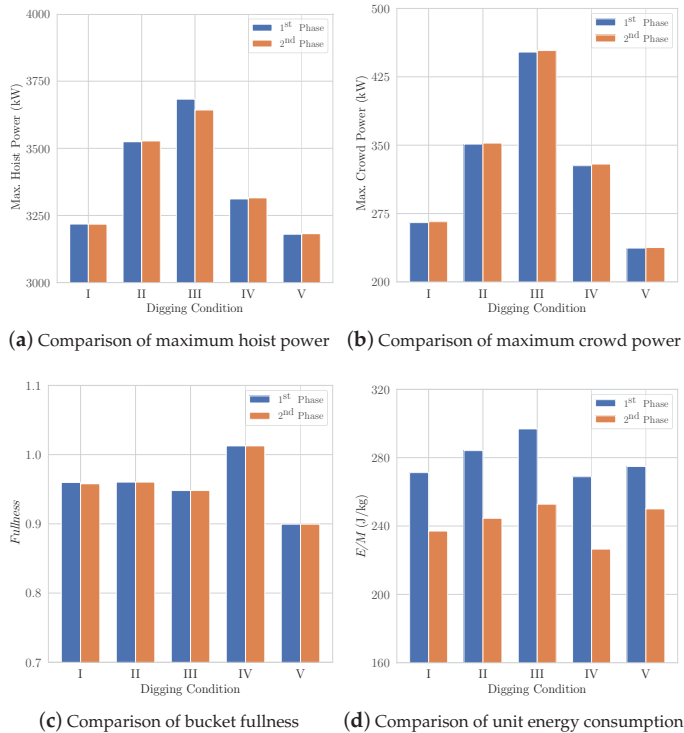


Figure 15. Digging performance comparison between two phases of optimization.

As shown in Figure 15, the unit energy consumption per payload was the only parameter of digging performance that significantly changed after the second phase of optimization. To be more specific, the reduction of all five digging conditions was on average 13.28%. In other words, the second phase optimization mainly retained the advantage of the results of the first phase optimization with the energy consumption further decreased while making the digging trajectory more practical.

6. Conclusions

A kind of multi-objective two-phase optimization method was established for robotic excavation of cable shovels in this research. The cable shovel with a nominal dipper capacity of about 55 m³ (WK-55) was applied for the validation of the optimization method under various digging conditions with different forms of pile-up material and digging distance. Field tests were applied in the Anjialing mining site for the measurement of the digging performance of the cable shovel and the rational selection of the digging parameters. It could be concluded from the optimization process that different digging conditions corresponded to different optimal digging trajectories. However, if the shovel stayed too close to the material slope, there might not exist an optimal result for the digging trajectory. Therefore, the shovels should stay at a reasonable distance toward the material slope for an optimal digging process. The two-phase optimization took theoretical advantage of the digging trajectory with a constant value of soil cutting angle and overcame its weakness in executability. Under the same material condition of the Anjialing mining site, the optimization results indicated

that the average digging time decreased from 20 s driven by operators to 10 s after the first phase optimization. The unit energy consumption reduced by 13.28% after the second phase optimization. The optimization experiments under different digging conditions and the corresponding results proved that the two-phase optimization method established in this research was an adaptive and effective method for optimal digging trajectory planning.

Author Contributions: Conceptualization, Q.B.; methodology, Q.B. and Z.Y.; software, Q.B. and Z.Y.; validation, Y.W.; formal analysis, Q.B.; resources, G.W., Z.Y. and R.H.; data curation, Y.W.; writing—original draft preparation, Q.B.; writing—review and editing, R.H.; supervision, G.W. and R.H.; project administration, G.W.; funding acquisition, G.W. and Z.Y. All authors have read and agreed to the published version of the manuscript.

Funding: This research was funded by the National Natural Science Foundation of China (Grant Numbers 51775225 and 51875232) and the Shanxi Science and Technology Major Project (Grant Number 20191101014).

Acknowledgments: Thanks to Key Laboratory of CNC Equipment Reliability, Ministry of Education, China, provided the high performance computer on which we ran the optimization programs.

Conflicts of Interest: The authors declare no conflict of interest. The funders had no role in the design of the study; in the collection, analyses, or interpretation of data; in the writing of the manuscript, or in the decision to publish the results.

References

1. Darling, P. *SME Mining Engineering Handbook*, 3rd ed.; Society for Mining, Metallurgy, and Exploration: Englewood, CO, USA, 2011.
2. BabaeiKhorzoughi, M.; Hall, R. A study of digging productivity of an electric rope shovel for different operators. *Minerals* **2016**, *6*, 2.
3. Blackwell, G.H. Remote and Semi-Automated Operation of an Electric Cable Shovel Author. 2013. Available online: <http://www.iaarc.org/publications/fulltext/isarc2013Paper419.pdf> (accessed on 15 June 2020).
4. Awuah-Offei, K.; Frimpong, S. Cable shovel digging optimization for energy efficiency. *Mech. Mach. Theory* **2007**, *42*, 995–1006. [CrossRef]
5. Dunbabin, M.; Corke, P. Autonomous excavation using a rope shovel. *J. Field Robot.* **2006**, *23*, 379–394. [CrossRef]
6. Wei, B.; Gao, F. Digging trajectory optimization for a new excavating mechanism of electric mining shovel. In Proceedings of the ASME 2012 International Design Engineering Technical Conferences and Computers and Information in Engineering Conference, Chicago, IL, USA, 12–15 August 2012.
7. Wang, X.; Sun, W.; Li, E.; Song, X. Energy-minimum optimization of the intelligent excavating process for large cable shovel through trajectory planning. *Struct. Multidiscip. Optim.* **2018**, *58*, 2219–2237. [CrossRef]
8. Xu, G.; Ding, H.; Feng, Z. Optimal Design of Hydraulic Excavator Shovel Attachment Based on Multiobjective Evolutionary Algorithm. *IEEE Trans. Mechatronics* **2019**, *24*, 808–819. [CrossRef]
9. Jang, G.; Cho, S.-B. Optimal Trajectory Path Generation for Jointed Structure of Excavator using Genetic Algorithm. In Proceedings of the 2019 IEEE Congress on Evolutionary Computation (CEC), Wellington, New Zealand, 10–13 June 2019.
10. Yu, X.; Pang, X.; Zou, Z.; Zhang, G.; Hu, Y.; Dong, J.; Song, H. Lightweight and High-Strength Design of an Excavator Bucket under Uncertain Loading. *Math. Probl. Eng.* **2019**. [CrossRef]
11. Feng, H.; Yin, C.-B.; Weng, W.-W.; Ma, W.; Zhou, J.-J.; Jia, W.-H.; Zhang, Z.-L. Robotic excavator trajectory control using an improved GA based PID controller. *Mech. Syst. Signal Process.* **2018**, *105*, 153–168. [CrossRef]
12. Li, X.; Wang, G.; Miao, S.; Li, X. Optimal design of a hydraulic excavator working device based on parallel particle swarm optimization. *J. Braz. Soc. Mech. Sci. Eng.* **2017**, *39*, 3793–3805. [CrossRef]
13. Kim, J.-W.; Jung, S.; Kim, J.; Kim, J.; Seo, T. Optimal design of the front linkage of a hydraulic excavator for multi-objective function. *J. Mech. Sci. Technol.* **2014**, *28*, 3103–3111. [CrossRef]
14. Barakat, N.; Sharma, D. Evolutionary multi-objective optimization for bulldozer and its blade in soil cutting. *Int. J. Manag. Sci. Eng.* **2019**, *14*, 102–112. [CrossRef]
15. Masih-Tehrani, M.; Ebrahimi-Nejad, S. Hybrid Genetic Algorithm and Linear Programming for Bulldozer Emissions and Fuel-Consumption Management Using Continuously Variable Transmission. *J. Constr. Eng. Manag.* **2018**, *144*, 7. [CrossRef]

16. Zhang, Z.; He, B. Comprehensive optimum and adaptable design methodology for the working mechanism of a wheel loader. *Int. J. Adv. Manuf. Technol.* **2018**, *94*, 3085–3095. [[CrossRef](#)]
17. Cao, B.-W.; Liu, X.-H.; Chen, W.; Zhang, Y.; Li, A.-M. Depth Optimization Analysis of Articulated Steering Hinge Position Based on Genetic Algorithm. *Algorithms* **2019**, *12*, 3. [[CrossRef](#)]
18. Zelenin, A.; Balovnev, V.; Kerov, I. *Machines for Moving the Earth: Fundamentals of the Theory of Soil Loosening, Modeling of Working Processes and Forecasting Machine Parameters*; United States Department of Agriculture, and the National Science Foundation: Washington, DC, USA, 1985.



© 2020 by the authors. Licensee MDPI, Basel, Switzerland. This article is an open access article distributed under the terms and conditions of the Creative Commons Attribution (CC BY) license (<http://creativecommons.org/licenses/by/4.0/>).

Review

Electrification of Compact Off-Highway Vehicles—Overview of the Current State of the Art and Trends

Daniele Beltrami ¹, Paolo Iora ¹, Laura Tribioli ² and Stefano Uberti ^{1,*}

¹ Department of Mechanical and Industrial Engineering, Università di Brescia, 25123 Brescia, Italy; d.beltrami002@unibs.it (D.B.); paolo.iora@unibs.it (P.I.)

² Department of Industrial Engineering, Università di Roma Niccolò Cusano, 00166 Roma, Italy; laura.tribioli@unicusano.it

* Correspondence: stefano.uberti@unibs.it; Tel.: +39-030-3715517

Abstract: Electrified vehicles have undergone great evolution during the last decade because of the increasing attention paid on environmental sustainability, greenhouse gas emissions and air pollution. Emission regulations are becoming increasingly tight, and governments have been allocating multiple funds to facilitate the spreading of the so-called green mobility. In this context, steering towards electrified solutions not only for passenger vehicles, but also for compact off-highway vehicles extensively employed, for instance, on construction sites located in urban areas, warehouses, and greenhouses, is essential even if seldom considered. Moreover, the electrification of compact off-highway machinery may allow manufacturers to increase their expertise in and lower the costs of these alternative solutions, while gathering useful data to be applied in bigger and more remunerative off-highway vehicles. In fact, while electric automobiles are as of now real alternatives for buyers, off-highway vehicles, regardless of the application, are mostly in the research and experimental phase, with few of them already on the market. This delay, in comparison with the passenger automotive industry, is caused by different factors, mostly related to the different tasks of off-highway vehicles in terms of duty cycles, productivity performance parameters and user acceptability. The aim of this paper is to give an overview of the many aspects of the electrification of compact off-highway vehicles, to highlight the key differences between on-highway and off-highway vehicles and to summarize in a single source of information the multiple solutions investigated by researchers and manufacturers.

Citation: Beltrami, D.; Iora, P.; Tribioli, L.; Uberti, S. Electrification of Compact Off-Highway Vehicles—Overview of the Current State of the Art and Trends. *Energies* **2021**, *14*, 5565. <https://doi.org/10.3390/en14175565>

Academic Editors: Kwok Tong Chau and Rui Xiong

Received: 27 May 2021

Accepted: 27 August 2021

Published: 6 September 2021

Publisher's Note: MDPI stays neutral with regard to jurisdictional claims in published maps and institutional affiliations.



Copyright: © 2021 by the authors. Licensee MDPI, Basel, Switzerland. This article is an open access article distributed under the terms and conditions of the Creative Commons Attribution (CC BY) license (<https://creativecommons.org/licenses/by/4.0/>).

Keywords: electrification; green mobility; compact off-highway vehicles; battery electric

1. Introduction

The attention directed toward environmental sustainability has undergone a great increase in recent years, with the authorities pushing more and more towards a cleaner and more efficient usage of energy. In this context, the environmental impact of the transport and mobility sector is a very relevant topic all around the world: in Europe, for instance, the European Green Deal [1] aims for a 90% reduction in transport emissions by 2050. To reach the climate neutrality, new vehicle concepts, such as electric and hybrid vehicles, are believed to be essential [2] and the International Energy Agency (IEA) foresees a growth in the market share of electric vehicles (EVs) from 5 million in 2018 to 130–250 million by 2030 [3]. According to a European report on sustainable economy [4], 75% of European citizens live inside urban areas, meaning that the so-called “smart cities” are going to be the centers of innovation in mobility; as a consequence, compact electric vehicles are crucial, because they are more suited to urban environments. Additionally, compact machinery that work in very limited areas (construction sites, warehouses, greenhouses) can benefit significantly from full electric powertrain [5].

The automotive supply chain has been addressing the process of electrification for more than a decade, and now there are many feasible alternatives to the internal combustion engine (ICE) vehicles; at the same time, this growth is also pushing the off-highway vehicle

industry to accelerate its progress in the same process. In this regard, off-highway vehicles are an important source of emissions and fuel consumption [6], and, both in Europe and in the United States, authorities have been tightening the emission standards for non-road vehicles and machinery with the “TIER 1 . . . 4” [7] and the “STAGE I . . . V” classes [8]; because of these, it is predicted that, sooner or later, ICE-based vehicles could become more expensive than electric and hybrid ones [9].

While environmental concerns regarding air pollution and greenhouse gas emissions are the main drivers for the electrification process of the automotive industry, for the off-highway machinery industry, this process is strictly connected to other major drivers [10]: fuel economy, increased productivity and greater reliability.

Furthermore, while in a passenger vehicle, the power load is mainly related to traction [11], off-highway vehicles have a more complex load profile that is highly dependent on the mission of the vehicle and which is also related to different loads other than traction [12], such as hydraulic systems, ancillaries, etc. This implies important differences between automotive drive cycles and off-highway duty cycles, where the power requirements of hydraulic systems, ancillaries, implements and so on are major variables, highly fluctuating over a mission profile [13]. For this reason, the off-highway industry is investigating electrification to improve ancillaries and implements, too, in order to achieve lower operating costs, better control systems and new design possibilities [14].

To give a comprehensive overview of the state of the art, attention is firstly focused on the four main categories of the off-highway industry; then, the essential difference between automotive drive cycles and off-highway duty cycles is clarified. A brief overview on the main components of electric vehicles, i.e., batteries and motors, is provided before the in-depth analysis of the state of the art, where the major trends and requirements are investigated from a novel viewpoint focusing on the most developed off-highway category, namely the construction category. Before presenting the analysis of the possibilities for efficiency enhancements with respect to hydraulic and energy recovery systems, a list of some interesting compact electric vehicles is provided for each off-highway category. Lastly, a very brief outline of existing hybrid vehicles for these applications is presented, highlighting some of the differences between pure electric and hybrid solutions.

Therefore, this review aims to summarize the main topics surrounding the electrification of compact off-highway vehicles and machinery, highlighting which components or technologies are more suited for the compact segment of the industry, while also aiming to show how important compact machinery are and can be for the electrification of the whole industry; indeed, the authors believe that the compact segment is sometimes underestimated and, as far as the authors know, this is the first comprehensive review with a specific focus on the components that best suit these types of machinery. Furthermore, on the basis of a market analysis, we aim to show the actual trends in both the research and the industrial fields, providing the reader with a forecast about what to expect in the next few years.

2. Off-Highway Vehicles’ Categories

The key aspect in the off-highway vehicles industry is that every vehicle is designed in order to complete its specific duty, based on intensive application within its specific operating environment [15]. As a result, there are many vehicles of different weight, power, layout, etc., that are tailored for specific duties, and the evaluation of the electrification possibilities for such vehicles is challenging because of this extensive diversity.

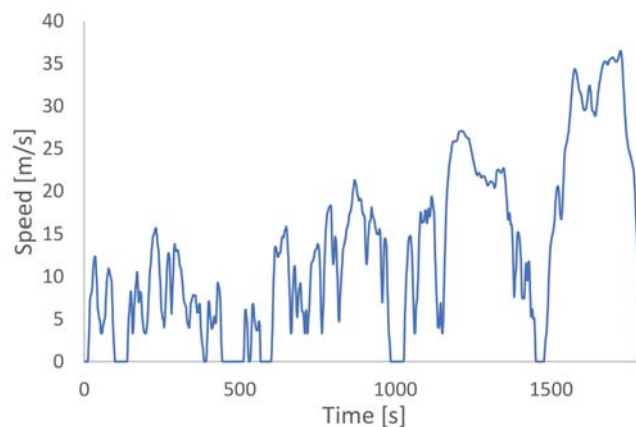
For the sake of simplicity, off-highway vehicles can be grouped into four main categories, as shown in the Table 1. Even if these different categories are universally recognized within the industry, there are instances of multipurpose vehicles that can be fitted with different accessories in order to fulfill duties across the board, e.g., small tractors that can be used during winter as snow removal machinery, or municipal and property maintenance vehicles with many different type of equipment.

Table 1. Off-highway vehicle categories.

Category	Vehicle
Tractors and agricultural.	Tractors, combine harvesters, field choppers, etc.
Municipal and property maintenance.	Turf cutters, street sweeping machines, etc.
Transportation of goods and material handling.	Forklift machines, material handlers, etc.
Construction, forestry and mining.	Excavators, frontend loaders, backhoes, etc.

3. Duty Cycles

Among the many different car-related drive cycles, the two most widely known ones are the New European Driving Cycle (NEDC) and the World harmonized Light-duty vehicles Test Procedure (WLTP) (Figure 1), which is the current standard for the evaluation of the fuel consumption and exhausts type approval tests.

**Figure 1.** WLTP Drive cycle for passenger vehicles.

As can be seen in Figure 1, where the WLTP cycle is shown, typical automotive drive-cycles are based mainly on the speed profile, since the main power request source in passenger cars is the traction power, which is assumed to always be satisfied by the engine. Furthermore, any automobile manufacturer must test any new vehicle under the WLTP drive cycle before putting it on the market, and consequently all manufacturer information on fuel consumption is based on it. There are also many other standard drive cycles, but they are used mainly for engineering purposes, meaning that they are used during the vehicle design and verification phase, and they are not aimed at any certification process.

On the other hand, duty cycles for the off-highway industry must take into account different additional aspects: first of all, regardless of the vehicle under analysis, the duty cycle is much more intense in terms of magnitude and frequency of power peaks, as visible in Figure 2, which shows an example of drive mission for an agricultural tractor [13]; secondly, as of now, these standard duty cycles are used only for internal engineering and testing purposes, and they are not assumed to be a common basis among manufacturers. In these circumstances, every Original Equipment Manufacturer (OEM) is accustomed to its internal duty cycles and researchers even tend to register specific duty cycles for each vehicle under analysis.

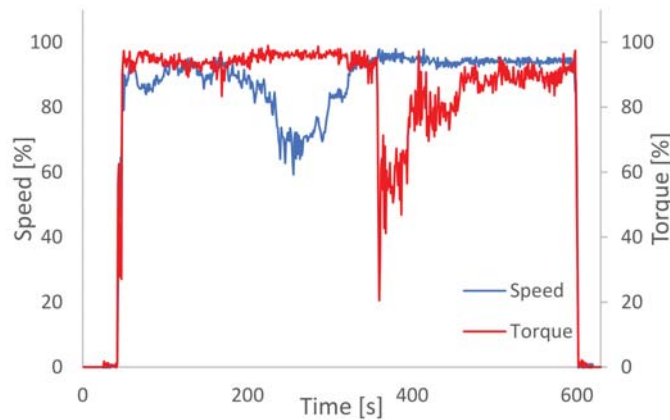


Figure 2. AG Tract Drive cycle for agricultural tractor.

As previously stated, the power flow in off-highway vehicles is not directed completely to traction, but rather is variably divided into different power outputs related to mechanical or hydraulic loads. Therefore, the definition of a typical duty cycle is also a huge challenge among vehicles that are similar.

To the best of authors' knowledge, the only known exception is the DLG Power Mix (Deutsche Landwirtschafts Gesellschaft-German Agricultural Society) [16], which states itself as the de facto standard for agriculture tractors, but it has no legal value for the homologation process, and it is mainly used to provide product information to potential buyers. In this regard, Refs. [17–19] investigated the electrification of agricultural tractors, but each one used different duty cycles, without mentioning anything about the DLG Power Mix or the AG Tract Drive cycle (Figure 2).

The same happens in the case of construction vehicles: in [20,21] the authors defined a specific duty cycle for the hybridization process of a skid loader, while in [22–26] different duty cycles were used for analyses on compact excavators. The need of a standard duty cycle for excavators has been emphasized in many articles, such as [27], and a good attempt at standardization was made by the Japanese Construction Mechanization Association with the test procedure explained in [28], but they are still not globally recognized.

As a matter of fact, duty cycles are key points for the electrification design process, since knowing the power and torque request profiles for each vehicle allows the correct selection and sizing of the on-board power sources, powertrain layout and energy storage systems. The final aim of the cycle analysis is the model-based simulation for energy consumption and working range estimation.

Operational runtime is another essential point for the electrification process, because many off-highway vehicles need to be continuously operative for eight or more hours, with very little or even no time for recharging during the day. Thus, the computation of working range and, eventually, elapsed charging time are essential parameters for boosting scheduling at building sites, warehouses, logistic and industrial plants, and so on.

4. Main Components and Architectures of Electric Vehicles

Similarly to what is reported in [29], electric off-highway vehicles can be divided on the basis of their architectures:

- tethered type: these need constant physical connection to an external electric source; this can be the power grid or an external electric generator.
- battery type: these work completely disconnected from any external power source, which is needed only to recharge the internal energy storage system when the vehicle is not in use.
- tethered-battery type: there is the possibility of using the vehicle even during charging.

All these architectures are useful for specific applications and have been investigated during the last decade. For instance, extremely large excavators can exploit the boost in efficiency given by electrification [30], but to supply enough power to their systems, they require a physical connection to the power grid. Similarly, articulated loaders for underground mining have been electrified for many years, and they are already widespread in the market because of the primary need to not pollute underground air, but the majority of them are constantly connected to the power grid due to their very high energy demand [31]. Tethered-battery vehicles can overcome their limited range by connecting them to a set of overhead lines, like trolleybuses do [32], or to an external diesel generator only when needed, but this second solution is not ideal because it does not eliminate local air pollution and noise. Therefore, especially for compact electric vehicles, the most interesting architecture is the battery-type, as their operation is not limited by any electric cables.

Because of the high complexity of the drivetrain, the need for optimizing the efficiency, and the inherent flexibility provided by electrification, architectures with multiple electric motors are an important subject of research. In fact, while thermal engines usually require mechanical devices and/or hydraulic systems to transfer power, electric motors can be distributed differently on the vehicle platform. For instance, the automotive industry is looking at the optimization of weight distribution, the possibility of exploiting the benefit of torque vectoring and the enhancement of efficiency by cleverly combining speed and torque from different motors [33]. The benefits for the off-highway industry are even more profound. Indeed, depending on the mission, it could be useful to enhance the traction by using multiple motors on each axle [12], to move implements and ancillaries independently from one to the other [34,35], or to better control the speed of hydraulic pumps [36].

Thus, it is important to briefly analyze two of the main components of any battery electric vehicle: the energy storage system and the electric motor.

4.1. Energy Storage Systems

The energy storage system is a key element for any electric vehicle. The main properties of any energy storage system are: specific power (W/kg), specific energy (Wh/kg), energy density (Wh/L), cycle life, and efficiency [11]. Thus, the choice of the energy storage is a combination of many aspects of the vehicle and its mission. In Table 2, a comparison between the most common energy storage systems [11,37] of the off-highway industry is provided.

Table 2. Comparison between the main energy storage systems [11,37].

	Flywheel	Supercapacitor	Hydraulic Accumulator	Lead-Acid Battery	Ni-MH Battery	Lithium Battery
Specific power (W/kg)	400–1500	500–5000	2000–19,000	75–300	150–200	250–340
Specific energy (Wh/kg)	10–30	2.5–5.5	2	30–50	60–120	75–200
Energy density (Wh/L)	20–80	35	5	50–80	150–180	200–250
Cycles	20,000	100,000	100,000	500–1500	2500	2000–10,000
Efficiency (%)	<96	<95	<90	<80	<90	<95

Among the different types of batteries, lithium batteries are recognized as the present state of the art, and also as the most interesting long-term solution, both from a technical and a cost-performance points of view; indeed, from 2010 to 2016, specific cost per energy unit (\$/kWh) decreased at a rate of almost 20% per year [38], while different combinations of cathode, anode and dielectric have entered the market. In this regard, while the automotive industry uses different chemistries such as LiFePO₄ (Lithium Iron Phosphate), NCA (Lithium Nickel Cobalt Aluminum Oxide) and NMC (Lithium Nickel Manganese

Cobalt Oxide) [39], in the off-highway industry, LiFePO₄ chemistry stands out as the de facto standard thanks to its inherent better safety and thermal stability [40].

Flywheels, supercapacitors and hydraulic accumulators have higher power density than batteries, but they are lacking in energy density, and this makes them more suitable for hybrid architectures, where the main energy source remains the ICE and the energy storage systems are used to follow the power peaks without excessively ramping up the ICE [41], and/or to accumulate energy from the recovery systems. Hydraulic accumulators in particular have extremely high specific power, but they also have the worst energy density, making them more difficult to implement in compact vehicles [42].

To improve the overall efficiency, researchers are focusing on the combination of more than one energy storage system [43–45]; consequently, it would be possible to take advantage of components with either high specific power or high specific energy.

4.2. Electric Motors

Electric motors are the other fundamental components of electric vehicles: they convert electrical energy into mechanical energy, and they can also act as generators during regenerative events. Furthermore, their efficiency is higher than that of ICEs and, for limited periods of time, they can reach much greater peaks of power [46] (in some cases even two or more times higher than their target continuous power). In addition, thanks to their inherent characteristics and the use of an inverter, electric motors can supply the maximum available power along almost the entire velocity range [37], following an ideal curve for traction purposes.

Any electric motor to be implemented into a vehicle needs the following characteristics: mechanical ruggedness, high torque density, high energy efficiency, wide speed range, low noise, low or null maintenance, simple control and low cost [47].

The main properties of the three most common electric motors used in both the automotive and the off-highway industries are shown in Table 3 [29,37,47–49]; even if reported as macro-categories, they have their inherent advantages and disadvantages.

Table 3. Comparison between the main electric motors' technologies [29,37,47–50].

	Induction Motor (IM)	Permanent Magnet Synchronous Motor (PMSM)	Switched Reluctance Motor (SRM)
Advantages	Very robust	High torque density	Good torque density
	Low cost	Very high efficiency	Very robust
	Easy to control	Good thermal	Low cost
Disadvantages	Low efficiency	High cost	Complex control
	Narrow speed range	Magnets decay	Loud noise
			Big torque ripples

Induction Motors (IMs) and Permanent Magnet Synchronous Motors (PMSMs) are nowadays the most common electric motors in the automotive market [50]; PMSMs stand out in terms of torque density, being the best choice for high performance vehicles and for purely tractive efforts, while IMs are very robust, easy to control and, because of the absence of expensive permanent magnets, their cost is much lower, although they are bulkier and heavier.

To combine the best of these two technologies, in the last decade, many studies have been carried out on Switched Reluctance Motors (SRMs) [51,52]; the low-cost rotor in place of the more expensive permanent magnets and the higher efficiency in comparison with the IMs are the great advantages of the SRM motor. However, because of the highly complex control mechanism, they have been implemented on working prototypes only recently. Nonetheless, due to the promising cost/performance ratio, SRMs have been pointed out as the biggest future improvement in electric motors for both the on-highway and off-highway industries [53].

5. State of the Arts and Trends

To find the common trends of the electrification process within the off-highway vehicle industry, the authors believe that a market analysis focusing on the most developed category of the industry may be regarded as representative. Therefore, this paper focuses the market analysis on the construction vehicle category, in particular, the case of excavators and front-end loaders, as they are the two most common types [42]. It should be noted that while the data were collected from OEM websites, scientific papers, and trade magazines, they remain indicative values; when they were incomplete, they were consciously derived by the authors.

Figure 3 shows the ratio between the operative weight and ICE power of excavators, along with their electric counterparts, where EM continuous power is considered in place of ICE power; the linear regressions between the two are also reported. As can be seen, the power-to-weight ratio is almost identical, meaning that almost all the electric vehicles are designed by simply substituting the ICE with an electric motor of equivalent power (continuous mode). Things are different when considering the peak power of the electric motors. Indeed, in this case, as can be seen in Figure 4, the power-to-weight ratio of the electric excavator is constantly higher than the ICE-powered one. It should be noted that, in the case of peak power, the plot is restricted to smaller excavators because of the highly scattered data of the bigger ones.

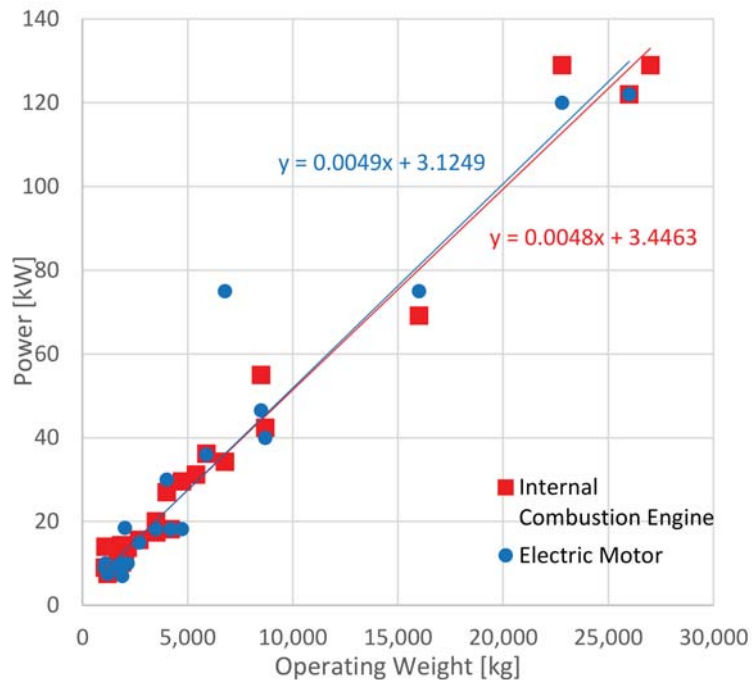


Figure 3. Power-to-weight ratio of ICE excavators and EM excavators (continuous power) with linear regressions.

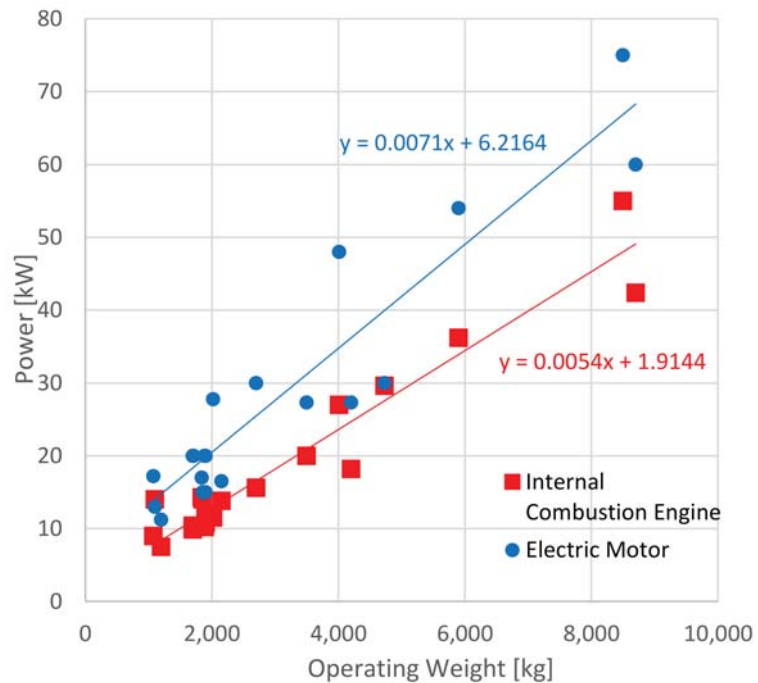


Figure 4. Power-to-weight ratio of ICE-powered excavators and EM-powered excavators (peak power) with linear regressions.

Another fundamental aspect visible in the plot is that the majority of the vehicles belong to the compact segment, characterized by a weight below 5000 kg and a maximum power of 30 kW. This is due to two key reasons: on the one hand, the electrification of compact vehicles is less expensive for manufacturers, providing the opportunity of having cost-efficient running vehicles, from which useful operating data can be collected for scaling up toward bigger and more remunerative vehicles [54]; on the other hand, the emission regulations and the increasing number of “zero-emission” city centers [55] makes electrification necessary for the compact class of excavators in the immediate future. In this regard, manufacturers like Volvo CE (Gothenburg, Sweden) and Wacker Neuson SE (Munich, Germany) are already conducting customer field tests on emission-free construction sites [56,57], while municipalities like Helsinki, Amsterdam, Brussels and others are exploring the possibility of limiting public construction tenders to free-emission vehicles and projects only [58].

In Figure 5, another interesting aspect of the electrification process is shown, which is the rather common choice of keeping the voltage below the high-voltage automotive limit of 60 V DC (Direct Current) [59], providing an advantage in terms of costs reduction. On the one hand, the low cost is made possible by the higher level of standardization of the components for systems below 60 V [60] (they have been used for decades on electric forklifts and they are currently used on most of the automotive hybrid systems, including start and stop systems), while on the other hand, above this limit, much more sophisticated, protective and reliable systems for preventing short-circuits are needed [61]. In this regard, the automotive industry is already moving towards high-voltage systems because of their inherent increased efficiency [62], while their higher costs are mitigated thanks to their suitability for mass production.

Regarding efficiency and energy consumption, it can be seen from Figure 6 that the operational runtimes of electric excavators are very scattered; the main reason for this is the

absence of a standard duty cycle commonly recognized by manufacturers. Therefore, many of the available data regarding running times are neither accurate nor validated. Even if there are scientific papers and published manufacturers' reports in which the operational runtimes are calculated by means of the published duty cycles, like the one by the Swiss manufacturer Suncar HK AG (Oberbüren, Switzerland) [24], these are barely comparable to the others.

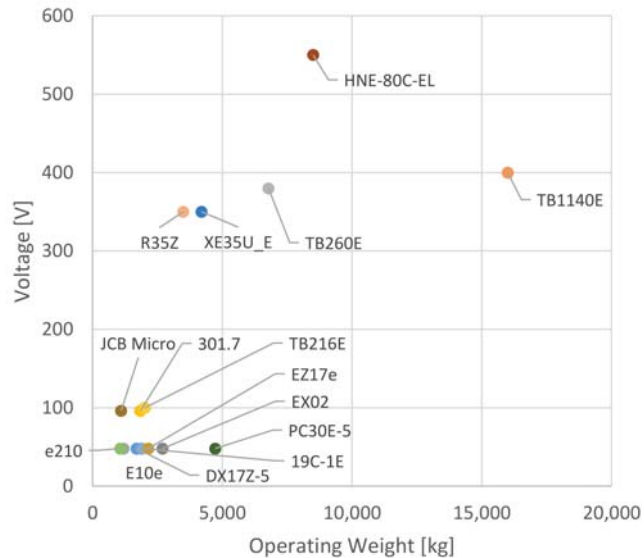


Figure 5. System voltage in relation to the operating weight. Labels refer to different excavator models according to manufacturers' datasheets.

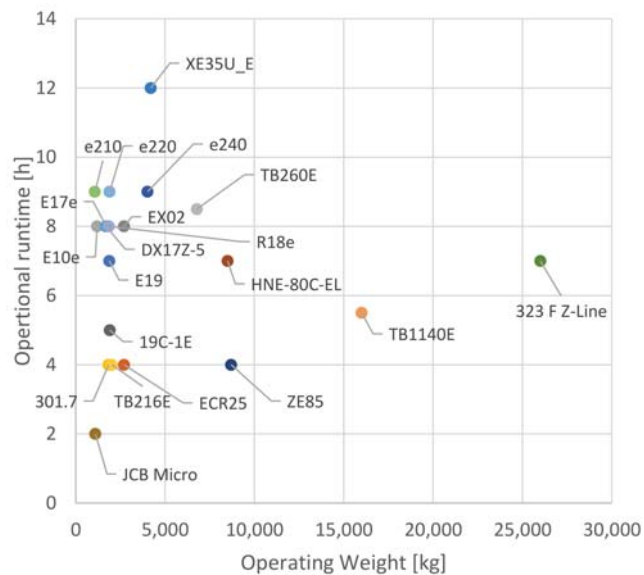


Figure 6. Operational runtime in relation to operating weight. Labels refer to different excavator models according to manufacturers' datasheets.

As a matter of fact, most of the electric excavators are retrofittings of existing ICE-powered vehicles, where the design efforts were limited to the integration of the electric motor, battery pack and charging system in place of the ICE and the fuel tank, with additional efforts devoted to the implementation of the control system for the new powertrain architectures.

The situation is similar for front-end loaders, as can be seen in Figure 7, even if there are some differences: first of all, the number of electric vehicles is much lower; secondly the data are much more scattered.

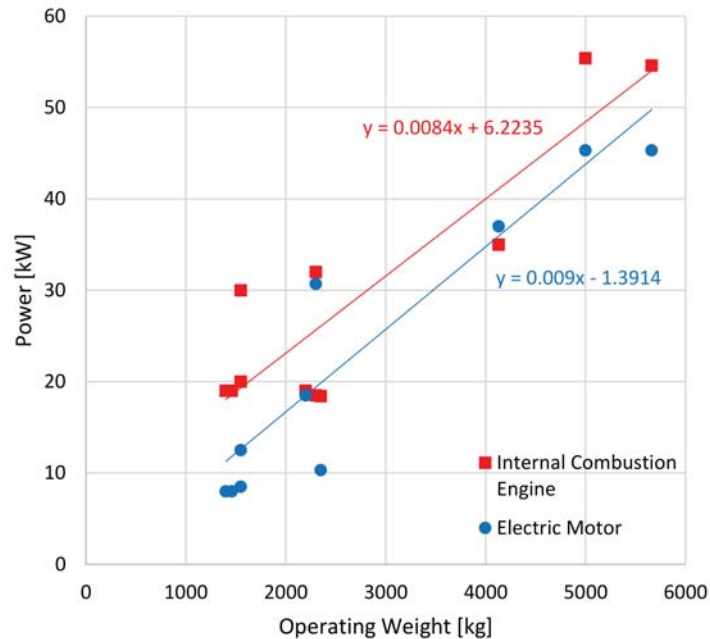


Figure 7. Power-to-weight ratio of ICE-powered loaders and EM-powered loaders (continuous power) with linear regressions.

Another relevant difference is related to the changes in the powertrain architectures adopted for the electric vehicles; for instance, in the majority of the front-end loaders, manufacturers prefer the adoption of two EMs instead of the single ICE (Figure 8), differentiating the power flow requested by traction from the power flow requested by hydraulic actuators and ancillaries. The typical mission of front-end loaders indeed requires great tractive effort, while excavators usually work at a fixed point, and consequently, the choice to double the motors allows a great improvement both in productivity and in efficiency. The results are visible in Figure 7, where it is clear that the continuous power of electric loaders is usually lower than the corresponding ICE-powered original versions.

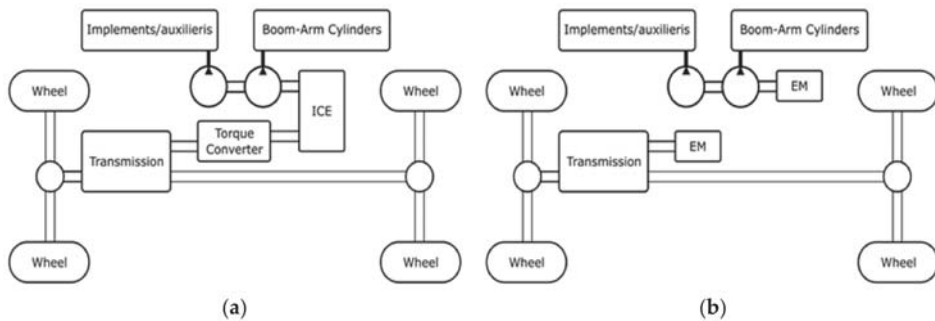


Figure 8. Simplified power scheme of a front-end loader. (a) ICE-powered loader. (b) EM-powered loader.

The lower number of electric front-end loaders can be justified by the higher cost of development, but, in the same way as for excavators, the greatest number of electric applications can be found within the compact segment, characterized, once again, by weight under 5000 kg and the power below 30 kW.

However, the common and most important aspect of the current electrification process is the attempt to maintain reasonable costs by limiting difficult innovations, developing retrofitted electric vehicles from existing ICE based ones and/or outsourcing much of the design process to more specialized and agile companies, such as Green Machine (Buffalo, NY, USA), who have played an extensive role in the electrification of many pieces of construction equipment from different manufacturers such as Case CE (Amsterdam, The Netherlands), Takeuchi Mfg (Sakaki, Japan) and Bobcat (West Fargo, ND, USA) [54].

In this scenario, predictions from Frost and Sullivan [63] foresee an increase of the battery electric compact excavator market share from the current 1% to 4% in 2030, as well as an increase in compact battery electric front-end loaders to 6% before 2030.

Regarding the other categories of off-highway vehicles and machineries, the number of electric products is much more limited; consequently, it is impossible to statistically verify the identified trends identified above. Nevertheless, picking some vehicles for any category, case-by-case they generally confirm these trends. For instance, the electric telehandler 525-60E by JCB [64], which is considered to be within both the construction and agricultural categories, has two electric motors (17 kW and 22 kW), and it follows the trend of the front-end loaders, since, due to a relatively better efficiency, its power-to-weight ratio is slightly lower than the ICE-based one. Still, with respect to agricultural machinery, in [65], the retrofiting of a 9.6-kW diesel tractor is presented, whereby the engine is replaced with a 10-kW electric motor, with a slightly higher operating weight. Lastly, in the mining category, the biggest battery electric vehicle is the Swiss e-dumper, retrofitted from a Komatsu HD-605 [66]; while the original version has a diesel engine of 578 kW, the electric one has a 673-kW motor, but, at the same time, the operating weight of the electric version is higher and the power-to-weight ratio remains similar.

In conclusion, it is worth mentioning that the trends cited above are in agreement with the electrification roadmap of some of the major Tier 1 companies, such as ZF Friedrichshafen AG (Friedrichshafen, Germany) [67], Bosch Rexroth AG (Rolf am Main, Germany) [68] and Deutz AG (Cologne, Germany) [69].

6. Relevant Off-Highway Electric Vehicles

In this paragraph, some compact off-highway vehicles are presented in order to give practical instances of existing electric and hybrid vehicles; while some of them are purely research projects or experimental prototypes, other are already available on the market.

It should be noted that, even if the focus is on compact machines, some very interesting non-compact vehicles are included to give a more complete overview.

6.1. Tractor and Agricultural Machinery

Within the category of tractors and agricultural machinery, electrification has been pointed out as the next important milestone [70], since the technology has almost reached its optimization limit, but the need for agricultural equipment is increasing due to global population growth. Market research reported in [9] states that the current electric solutions are sufficient only for a small niche of greenhouses and orchards.

Regarding the farm tractor market, the most interesting partition is determined on the basis of power output, which divides the tractors in three main categories: below 49 HP, between 50 HP and 79 HP, and above 80 HP [71]. For the purposes of this article, the most interesting projects are those below 79 HP, which can be defined as compact.

One of the most interesting compact electric project is the Fendt e100 Vario (Figure 9a) which is equipped with a 50-kW electric motor and a 100-kWh lithium battery at 400 V, with a stated working autonomy of 5 h and the possibility of restoring the battery state of charge (SOC) up to 80% in 40 min. Implements can be attached via traditional power take-offs (PTOs) or hydraulic, but there is also a 150-kW electric plug [72].



Figure 9. Electric tractor. (a) Fendt e100 Vario. (b) Rigitrac SKE 40. (c) Monarch MK4. [72–74].

Two other interesting electric projects are the Rigitrac SK-50 and SK-40 (Figure 9b). These are actually market products, and they are characterized by the use of five electric motors: two traction motors, one motor for each of the two power take-offs, and one motor for the hydraulic system. The operational runtime is stated to be about 5 h, with the possibility of rapid charging the battery to 80% SOC in 2 h [73].

Another very interesting project is the Monarch MK4 (Figure 9c), which is not only the first orchard and vineyard tractor of the Californian start-up company, but is also the first automated tractor available on the market. It has two 30-kW electric motors, one for traction and one for the PTO, and the company claims an operational runtime longer than 4 h, with the possibility of swapping the entire battery pack to rapidly come back to work instead of waiting for the complete charge, which takes more than 4 h at 220/240 V [74].

Lastly, the Farmtrac 25G is a 15-kW electric tractor [75]. It is commercially available, and, thanks to its 22-kWh NMC lithium battery, the operational runtime is stated to be about 8 h, with the charging time estimated to be close 5 h with a common domestic socket.

Among the electric agricultural vehicles that cannot be considered as compact, the concept machinery and working prototypes of John Deere (Moline, IL, USA) are surely worth mentioning; indeed, the John Deere SESAM (Sustainable Energy Supply for Agricultural Machinery) and the John Deere GridCON are testament to the interest of the company in researching novel approaches to face similar problems. The SESAM tractor is equipped with a 150-kWh battery pack for 1 h of intense work before recharging [76], while the GridCON is a tethered, fully autonomous and unmanned tractor equipped with a 100-kW electric motor for traction, and 200-kW electric motor directly connected to the PTO in order to transfer mechanical power to implements [77].

The last highly interesting agricultural vehicle is the E-OX 175 [78], which is the most recent development of the innovative Multi Tool Tractor, and it probably represents one of the most groundbreaking examples of how much electrification can transform the common architectures. Indeed, not only the traction is guaranteed by four wheel-drive electric motors, but it can also change its wheelbase and turning radius in order to optimize its use on fields without damaging the crop.

6.2. Municipal and Property Maintenance

The most important municipal and property maintenance vehicles are municipal vehicles and street sweepers, which are also among the most interesting vehicles for the electrification process due to their urban use, their highly fluctuating duty cycle, and the use of many different types of equipment for sweeping, cleaning and vacuuming. Furthermore, these vehicles usually work during the night, meaning that a reduction of the noise level is a very attractive feature, and finally, these are very interesting applications for the automation process.

In [79], a feasibility study is performed for an electric street sweeper, including the definition of a representative duty cycle, modeling of the vehicle, and the selection of suitable components for the powertrain and driveline. The simulated duty cycle results in an operational runtime below 5 h, where the cleaning equipment requires more than half of the gross power of the electric motor.

Dulevo International S.p.A. (Fontanellato, Italy), one of the leading companies in street sweeping vehicles and equipment, already offers an electric vehicle called Dulevo D.Zero² (Figure 10a), equipped with a lithium battery pack and capable of working for an entire work shift [80]; another instance is the Swiss Boschung Holding AG (Payerne, Switzerland), which has an electric street sweeper called the Urban-Sweeper S2 (Figure 10b), equipped with a 54.4-kWh battery capable of providing up to 10 h of autonomy with the possibility to fully charging the battery in 100 min thanks to the rapid charger [81].

In [82], an electric municipal vehicle by Esagono Energia S.r.l. (Pozzuolo Martesana, Italy) (Figure 10c) was used to validate a mathematical model able to predict with sufficient accuracy the working range of a L-7 vehicle, also taking into consideration the effect of slopes; the tested vehicle was equipped with a 15-kW induction motor, a LiFePO₄ battery of 15.3 kWh and it is available with many different types of equipment. Because of the aim of the paper and the equipment of the vehicle under testing, the duty cycle is a simple drive cycle, and it is registered via an experimental campaign; the working autonomy results were adequate for a complete work shift, but further investigations would be useful to predict the impact of different equipment on the same base model.

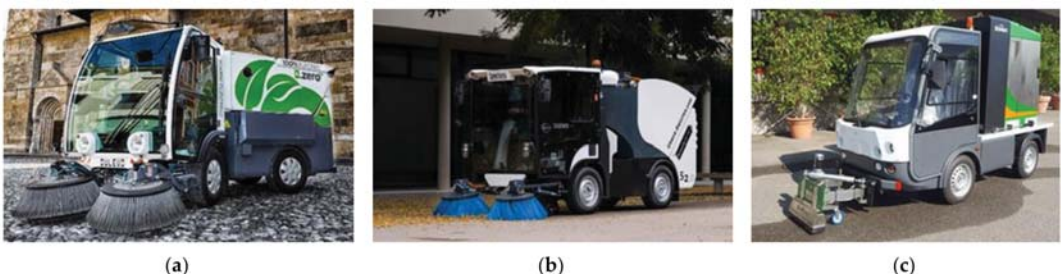


Figure 10. Electric maintain property vehicle. (a) Dulevo D.Zero2. (b) Boschung Urban-Sweeper S2. (c) Esagono Energia Gastone. [80,81,83].

Examples of non-compact vehicles are the electric refuse trucks that are entering the customer testing phase, like the ones used in Nottingham, where the City Council has declared that they are outperforming the ICE-powered counterparts, with lower fuel consumption and greater speed in completing the shift route [84].

6.3. Transportation of Goods and Material Handling

There are specific applications in which electric vehicles and machinery already represent a suitable and highly appreciated solution, such as in the case of forklifts, which are also the most widely known compact goods transportation vehicles. Indeed, electric forklifts were the first off-highway vehicles to be converted into electric ones and, as a consequence, they are currently very popular for the use inside warehouses, where the absence of exhaust gas emission and lower noise levels are considerable advantages and where the charging infrastructure is easily available. The technology is mature and competitive to such an extent that, according to Toyota Material Handling (Kariya, Japan) [85], even electric forklifts up to 9000 kg are gaining acceptance among consumers, and their upfront cost is only 10–15% higher than ICE-based counterparts. Consequently, all the major forklift manufacturers, such as Toyota Material Handling (Kariya, Japan), Hyster-Yale Materials Handling Inc. (Cleveland, OH, USA), KION Group AG (Frankfurt, Germany) and Jungheinrich AG (Hamburg, Germany) have a very large portfolio of electric forklifts with lead acid or lithium batteries (Figure 11a). Furthermore, it is worth mentioning that much of the current 48-V technology for the electrification of compact vehicles descends directly from the research on forklifts. Currently, forklifts remain among the most interesting vehicles for research and testing purposes, since their duty cycles can be easily monitored, and the available movements of their actuators are limited. For instance, in [86], the researchers investigated the application of two hydraulic motors to recover energy, while in [87,88], a powertrain based on fuel cells was analyzed.



Figure 11. Goods transportation and material handling vehicles. (a) Hyster-Yale forklift. (b) Simai towing tractor. (c) Sennebogen material handler. [89–91].

Other important compact material handling vehicles are the towing tractors, for which there is already a great number of electric vehicles due to their use in warehouses, production plants, ports and airports (Figure 11b). In all these cases, the routes are well defined, as well as the time-tables, and consequently, their use can be carefully planned in order to optimize their energy consumption and recharge times. Furthermore, electric powertrains are perfectly suited for these types of vehicles due to their typical high torque and low speed demands, with multiple speed variations that can be exploited to recover energy.

The last interesting vehicles in this category are the material handlers (Figure 11c). In this regard, tethered electric machines are used for very intensive use applications, while more compact battery electric ones are slowly entering the market; they are already suitable for less demanding applications and for use in cases where the cable connection could excessively limit the range of the machinery. However, one of the most advanced material handler is the prototype built by Dolomitech S.r.l. (Castel Ivano, Italy) and Moog Inc. (Elma, NY, USA) [92]: even if it cannot be considered as compact, being a 50-ton machinery, it is a battery electric vehicle with direct-driven hydraulics capable of optimizing energy consumption while guaranteeing the performance of an equivalent ICE-based counterpart. It currently represents the state of the art of electric material handlers, and its innovative hydraulic system is very interesting also for other off-highway vehicles.

6.4. Construction and Mining

The construction equipment industry is the biggest category of off-highway vehicles and, as already mentioned in Section 5, is promising for the electrification process, especially in the case of compact machinery that can be used in urban construction sites or indoor environments. Indeed, both the market and the scientific literature have been experiencing a remarkable increase in retrofitted electric vehicles in recent years, particularly with respect to compact excavators.

For instance, JCB Ltd. (Rocester, England, UK) was one of the first manufacturers to enter the market with an electric construction vehicle, and now it has many electric products for zero-emission construction sites under the JCB E-Tech brand, such as the compact excavator 19C-1E (Figure 12a), which is equipped with 19.8-kWh lithium battery and a 7-kW continuous power PMSM motor. This solution can exceed 4 h of continuous use, and also includes a proprietary rapid charge system able to reach 100% SOC in 2 h [93].

As already mentioned in Section 5, the second most common construction vehicle types are front-end loaders; a typical example of an electric compact loader is the Tobroco-Giant G2200E (Figure 12b), that is a four-wheel drive machinery with two different motors: a 6.5-kW (continuous power) motor for traction and a 12-kW motor for hydraulics. It is possible to choose between two lithium battery sizes, and the biggest one can store 24.9 kWh for an operational runtime up to 8 h [94].

Undoubtedly, one of the leading companies in the electrification process is Volvo (Gothenburg, Sweden) and within its very large portfolio of off-highway vehicles is the Volvo EX02 (Figure 12c), which is a full electric excavator equipped with electromechanical linear actuators and a 38-kWh lithium battery pack [95]. Being a testing prototype and a proof of concept, many technical details are unpublished, but Volvo claims a 10-fold fuel reduction with respect to its ICE-powered counterpart and a considerable decrease in total cost of ownership.

There are many other examples in the literature. For instance, in [23], a 2-ton electric excavator was modeled by means of Matlab/Simulink. The aim of the research was to create a model able to predict the operational runtime of the machine, and consequently much attention was given to the modeling the overall system, including hydraulics. The second purpose of the article was to develop a validated model to safely simulate new control strategies. Thanks to a 9.6-kW (continuous power) electric motor and a 15-kWh LiFePO₄ battery pack, the electric excavator retrofitted from a Bobcat E19 is able to reach up to 7 h of real working performance, and the power consumption is differentiated between excavation, relocation and travel. Another case that is worth mentioning is the compact excavator studied in [26], which has been used for multiple studies focused on electrification and hydraulics [96,97].



Figure 12. Electric construction vehicles. (a) JCB 19C-1E. (b) Tobroco-Giant E2200. (c) Volvo EX02. [98–100].

Regarding the mining sector, there are already many electric loaders that are very useful for reducing the air pollution issue at underground sites, but these are usually tethered machines, and they cannot be considered as compact. It is worth mentioning that,

more generally, compact vehicles are not suited for the mining industry. However, one innovative project is HX-02 load carrier studied by Volvo (Gothenburg, Sweden) and tested in the Swedish mining site Skanska: it is a battery electric, completely autonomous vehicle with a continuous power of 200 kW. Thanks to its implementation in more digitalized and automated mining sites, Volvo and Skanska state a reduction in total cost of operation of about 25%, with a CO₂ emission reduction of 95% [101].

7. Efficiency Enhancements

The focus on efficiency gains, power flows and, more generally, energy control strategies is a crucial point for the electric vehicles. Indeed, every waste of energy directly impacts the operational runtime and, accordingly, the battery pack, which is currently the most expensive component. While in ICE-powered vehicles the inefficiencies of the entire system are somehow negligible with respect to the even lower efficiency of the ICE, in electric vehicles, every waste of energy is much more relevant. In this regard, the two main possibilities for increasing the overall efficiency are the improvement and/or replacement of hydraulic systems, and the possibility of recovering energy. In the following, the different technologies are shown in a more comprehensive way, while in Tables 4 and 5, they are simply listed for the clarity of presentation.

7.1. Hydraulics Systems and Actuators

As previously stated in Section 5, many of the existing electric vehicles derive from existing ICE-based ones with only limited modification to the powertrain. Consequently, in most cases, the hydraulic systems remain almost unchanged. On the one hand, this choice allows operators to work as they are accustomed, with very little time required for adaptation to the different dynamic response of actuators imposed by the electric motor, while, on the other hand, it evidences the low efficiency of the current hydraulic systems.

As can be seen in Figure 13, in a conventional hydraulic system, the pump is mechanically coupled to the ICE, so the hydraulic power is strictly correlated with the ICE speed and torque; the higher the power requested by the load, the higher the corresponding speed of the ICE. Because of the combined lack of efficiency of both the ICE and hydraulic system, the net mechanical energy available is of about 25% at best, and even using an EM instead of an ICE, the maximum overall efficiency of the machinery increases to only 56% [102]. In [103] the energy flow of an excavator was analyzed in detail and it was shown that the actual energy to the final load was only the 26.6% of the hydraulic energy converted in the pump, confirming the rather low efficiency of the hydraulic system. Furthermore, in order to harness the benefits of electrification with respect to torque control, better dynamics, more accurate movements, and so on, standard hydraulic systems require the control of flow, pressure and direction, mainly by means of pressure drops, which can be regarded as intentional losses of energy [104]. Nonetheless, hydraulics is still considered essential in most off-highway vehicles and machinery due to its great power density; thus, its complete replacement is currently limited to niche products. In this scenario, research has been focused on two main strategies: reducing idle losses and lowering hydraulic ones [105].

Reducing idle losses, thanks to the inherent characteristics of electric motors, is the easiest and more cost-effective approach to save energy; the main idea is to lower the power output of the pump as soon as possible by limiting the swash displacement and/or controlling the pump speed. Even if the former is already very common across the industry, the control on the pump speed is something very difficult to achieve with ICEs, although it is easier to implement with electric motors. For instance, in [26], the researchers investigated the energy consumption of a micro-excavator retrofitted with an electric motor, in which the original fixed displacement pump was replaced with a variable displacement pump; the results showed great room for improvement and the main power losses were identified as occurring in the main directional valve group. In [106], a 6-ton electric excavator was simulated and tested in order to define the best strategy between the pure swash variable displacement strategy and the variable displacement and speed one; while the

former guarantees a maximum efficiency boost of about 10%, the second strategy allows an additional improvement of 28.5%. Still regarding idle losses, while all the ancillaries (cooling fans, heating ventilation and air conditioning system, etc.) are mechanically linked to the engine shaft in ICE-powered vehicles, with electric vehicles and machinery it is possible to use decentralized and much smaller electric drives, making them independent of one another and optimizing the speed range of each of them, with those that are not needed even being turned off. However, while the speed and displacement strategies are already of great interest for compact vehicles, since they do not require additional room, the application of decentralized drives requires a slightly new design of the vehicle architecture.

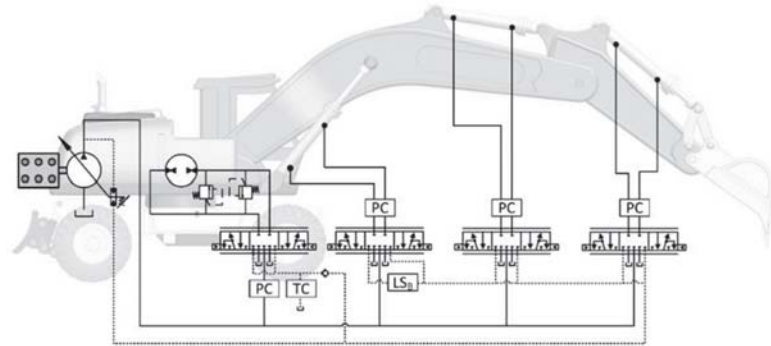


Figure 13. Hydraulic scheme of an ICE powered excavator. [105].

The other strategy, namely the reduction of hydraulic losses, requires many more changes in terms of hydraulics, as it requires the replacement of one or more components. In fact, the major loss is located in the main directional valve group, and consequently many researchers have investigated the of replacing this very common, reliable and easy-to-control component with Individual Metering Control systems (IMC). In [107], the researchers conducted a comparative simulation study on an ICE-equipped excavator, comparing the traditional valve group and an IMC system; the results revealed a foreseen energy-saving up to 44% due to a decrease in the power consumption of the pump. This type of hydraulics has already demonstrated its potential in ICE-powered vehicles, and it can greatly benefit from the more accurate control of EM over the pump rotor speed. Another possible and already under-study method for eliminating the main directional valve group is the replacement of the main pump with the so-called direct-driven-hydraulics (also known as electro-hydrostatic actuator technology), meaning that every actuator is moved by an independent pump and electric motor; consequently, this solution is suitable only for electric (or hybrid) machinery due to the need to distribute the power to the dislocated pumps. In [96,97] a compact electric excavator was used as a proof of concept for the testing of three independent direct-driven-actuators replacing the original hydraulic system, achieving an overall efficiency up to 73% (Figure 14). As already stated, these solutions for the reduction of hydraulic losses often require redesigning many parts of the vehicles, and therefore, they are not ideal for retrofitted ones, irrespective of the size of the vehicle. However, because of the room available on bigger machinery, considering their extensive use of hydraulic systems, the mentioned solutions are more suitable for mid to large off-highway vehicles.

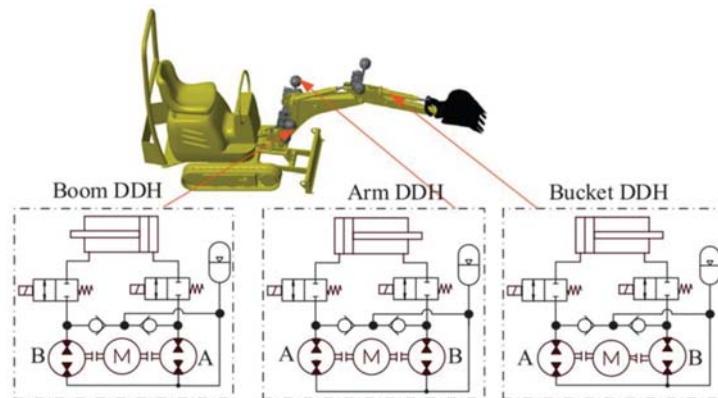


Figure 14. Direct-driven hydraulic scheme for a compact excavator. [97].

To increase the efficiency of the hydraulic system, there are also patented solutions that are undergoing testing by manufacturers (Table 4): one example is the Digital Displacement[®] Pump by Danfoss (Nordborg, Denmark) [108], which makes it possible to operate multiple actuators simultaneously by setting independent pressures and flows for each of them, allowing for a stated fuel reduction of more than 30%. A second interesting example, funded by European funds Horizon 2020 [109], is the multi-chamber actuators technology from Norrhydro (Rovaniemi, Finland), known as NorrDigiTM, which claims an efficiency increase up to 50% [110].

The more drastic approach to increase the efficiency is the replacement of as many hydraulic actuators as possible with electro-mechanical actuators (EMAs), following the trend already taking place in the aviation industry [111]. Even if it is currently restricted for niche products, this strategy could be considered as the final goal of the electrification process. Indeed, power-by-wire actuators would guarantee optimal efficiency, easier and more precise control, easier maintenance, better diagnostic and, above all, the possibility of designing vehicles and machinery with a comprehensive modular approach, due to the ease of electric cable design layout. High performance EMAs are formed by a ball screw drive coupled to an electric motor; the result is a compact, rigid, high-force capable and extremely accurate position control actuator, with fewer vibration problems. Some manufacturers predict an efficiency increase of about 50% [112], and in the literature there are instances of transmission efficiency gains up to 83%, such as in [113], where the hydraulic lifting system of an electric forklift is replaced by an electromechanical actuator.

Table 4. Hydraulic system enhancement.

Strategy	Comment	Vehicle	References
Reducing idle losses			
Variable displacement pump	Main valve causes 60% of losses	Excavator	[26]
Variable displacement and variable speed pump	Efficiency gain up to 28.5%	Excavator	[106]
Decentralized drive	Independent drive of ancillaries	Excavator	[105]
Reducing hydraulic losses			
Individual Metering Control	Energy saving up to 44%	Excavator	[107]
Direct-driven hydraulics	Overall efficiency up to 73%	Excavator	[96,97]
Digital hydraulics	Fuel reduction up to 30%	Excavator	[108]
Multi-chamber actuators	Fuel efficiency gain up to 50%	Excavator	[110]
Replacement of the whole hydraulics			
Electro-mechanical actuators	Efficiency gain up to 83%	Forklift	[113]

7.2. Energy Recovery Systems

Energy recovery systems have been recognized as the main advantages of electrification since the adoption of the first hybridization systems in the automotive industry. Due to the fact that the off-highway industry is characterized by the absence of a one-size-fits-all solution, based on the type of vehicle and especially its mission, the strategies for recovering energy can be very different, as well as the type of technology. However, generally speaking, the two most common forms of recovery are the kinetic energy regeneration and the potential energy regeneration [114].

The most known strategy for recovering kinetic energy is regenerative braking, which is already a must-have for hybrid and electric cars; thanks to the use of efficient transmission systems, brake-by-wire systems and effective control strategies, it guarantees the recovery of a high amount of energy. The basic principle is to recover the kinetic energy of the wheels during deceleration instead of dissipating it by means of traditional friction brakes, which remain mandatory due to their high braking power. In off-highway vehicles, this strategy is very promising for vehicles that experience significant variations in speed, like front-end loaders, or machinery with high-energy braking demands during descent from hills; for instance, in [115], a 31% fuel reduction was achieved on a 20-ton hybrid front-end loader, while in [82], the regenerative braking model constituted an essential part of the model of a 15-kW electric municipal vehicle. These two vehicles had mechanical transmissions between the wheels and the motor/generator; accordingly, they adopt supercapacitors and batteries, respectively, to store the recovered energy, similarly to passenger vehicles. However, in the off-highway industry, there are many vehicles that drive the wheels by means of the hydraulic system, and consequently, while on the one hand this enhances the possibility of storing the energy in hydraulic accumulators, on the other hand, it adds a degree of complexity to the system. For instance, the Wirtgen Group (Tirschenreuth, Germany) has a diesel hybrid tandem roller capable of recovering the braking energy into hydraulic accumulators (Figure 15a); thanks to this architecture, the recovered energy can be used to achieve the same performance as that of the pure diesel version while reducing the ICE size from 85 kW to 55.6 kW [116]. In [117], a simulation of a battery-powered hydrostatic vehicle was presented, with an in-depth comparison between the storage of recovered energy in hydraulic accumulators, in a battery, and both; the results showed that the highest energy efficiency was obtained when the energy was totally stored into the battery pack, while pure hydraulic storage presented the worst efficiency gain. Even if the deceleration of the moving vehicles is the main source of kinetic energy, there are vehicles that usually work at fixed point, like excavators or material handlers; in such cases, the aim is to recover the kinetic energy from the swing of the upper structure. In [118], where a swing system with a hydraulic accumulator was designed and tested on a test bench, the results showed a regeneration efficiency of up to 70%. Another example is the 20-ton hybrid excavator by Hitachi Ltd. (Chidoya, Japan) [119,120] (Figure 15b); on this machine, the swing hydraulic motor is directly connected to an electric motor/generator, and the recovered energy is stored into a capacitor unit.

Table 5. Energy recovery systems.

Strategy	Comment	Energy accumulator	Vehicle	References
Potential energy				
Third boom actuator	Energy saving ratio up to 25.5%	Hydraulic accumulator	Excavator	[121]
Multi-chamber actuator	Reduction power consumption up to 50%	Hydraulic accumulator	Excavator	[122]
IMC	Energy saving up to 44%	Hydraulic accumulator	Excavator	[107]
Direct-driven hydraulics	Overall efficiency up to 73%	Battery	Excavator	[96,97]
Kinetic energy				
Regenerative braking	31% fuel reduction	Super capacitor	Wheel loader	[115]
	ICE downsizing from 85 kW to 55.6 kW	Hydraulic accumulator	Tandem roller	[116]
Swing system	Regenerative efficiency up to 70%	Battery, capacitor	Excavator	[118]

The second form of recoverable energy is the potential energy; its principle is the recovery of the gravitational potential energy of falling objects, like the boom of an excavator or of a front-end loader, and the load moved by a crane, a forklift or a reach stacker (Figure 15c). In [121], as shown in Table 5, an additional hydraulic cylinder and a hydraulic accumulator were added to a 76-ton mining excavator, achieving a tested energy-saving ratio of about 25%. In this regard, the use of novel hydraulic solutions can add the possibility of storing energy in hydraulic form, like the innovative three chamber cylinders presented in [122], where the simulation showed a reduction in power consumption of up to 50%; indeed, thanks to their complex geometry, it is possible to use the single actuator as a small hydraulic accumulator. A similar concept has been implemented in IMC systems, where a descending actuator can be identified as a hydraulic motor for other actuators, allowing the pump to stay idle for longer periods, and thus lowering the power consumption (Figure 16). The excellent fuel efficiency performance obtained with the compact excavator studied in [96,97] was achieved thanks to the enhanced possibility of electro-hydrostatic actuators driving their own pumps while lowering, thus generating electric power that can be stored in batteries or capacitors. Lastly, in [123], a combined recovery system (electric and hydraulic) was modeled in order to estimate the maximum amount of energy that can be recovered by exploiting the peculiar characteristics of both the energy storage systems, the energy density of batteries and the power density of hydraulic accumulators.



Figure 15. Off-highway vehicles with energy recovery systems. (a) Wirtgen-Group tandem roller. (b) Hitachi excavator. (c) Konecranes reach stacker. [116,124,125].

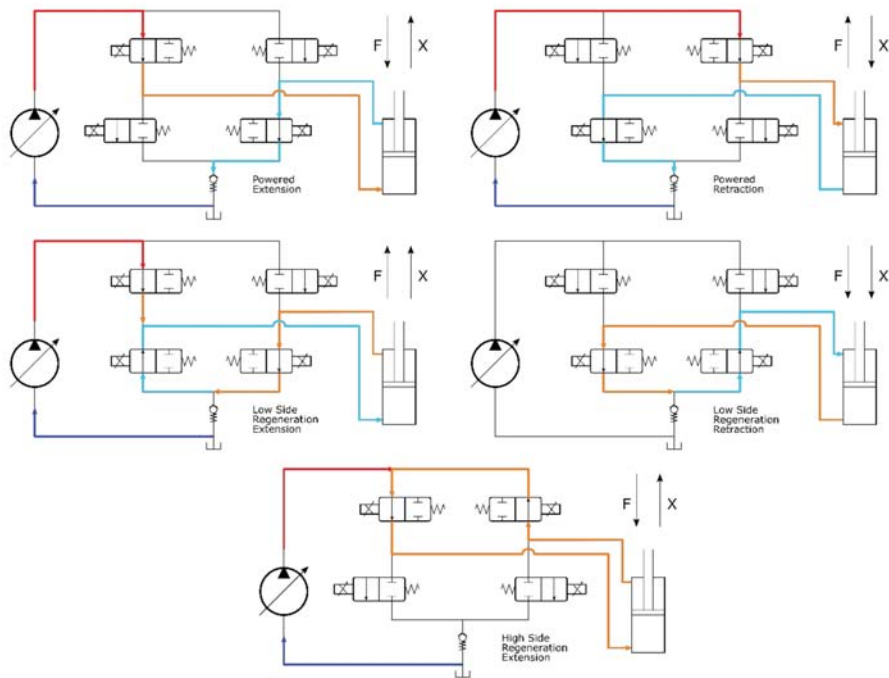


Figure 16. Scheme of an Individual Metering Control system (IMC) and working modes. (Adapted from [107]).

8. Hybrid Vehicles and Architectures

Like electric vehicles, hybrid architectures are considered to be among the most promising solutions for reducing energy consumption and local emissions, as well as improving performance in terms of controllability and productivity [126]; indeed, the focal point remains the optimization of the power flows in order to increase efficiency. The key difference with electric machinery is the presence of the ICE, which remains the main power source.

As mentioned in connection with duty cycles in Section 3, off-highway vehicles and machinery are characterized by highly fluctuating power flows, where the average power demand is much lower than the peaks. Consequently, hybridization can enable the downsizing of the ICEs, using the energy storage systems and the electric drives to respond to peak power demands.

The interaction between ICE, EMs, energy storage systems and loads (traction and/or hydraulic and/or implements) define three main hybrid architectures: series, parallel and series-parallel [127]; these are very similar to the automotive hybrid architectures, but with the essential difference that off-highway vehicles have to supply energy to both the traction system and the actuators and implements. In this regard, in contrast to the automotive industry, in [128], a novel definition of the hybridization factor was provided. In fact, while in the on-highway industry the hybridization factor considers only the tractive effort (propulsion hybridization factor), for off-highway vehicles and machinery is essential to consider the power demand of hydraulics and/or implements (loading hybridization factor).

Based on the weight and power classes of off-highway vehicles, the drivers for hybridization are slightly different. On the one hand, for medium size vehicles, which are regarded as the most interesting in the near future [129], the main drivers are reductions in the total cost of ownership and the enhancement of productivity; examples of machinery that follows these trends include the off-highway vehicles shown in Table 6, where, if stated

in the references, there are also reported their energy saving percentages in relation to the ICE versions. Even if some of these vehicles have been on the market for several years, their use has been limited thus far, mainly due to the much higher upfront costs; for instance, in the on-highway industry, the same thing happened with hybrid buses, which never really took off [5], even though they were able to achieve a fuel consumption reduction of up to 20% with respect to conventional buses [130].

Table 6. List of hybrid mid-size off-highway vehicles.

Manufacturer	Vehicle	Hybrid Architecture	Energy Accumulator	Energy Saving	References
Komatsu	20-ton excavator	Parallel hybrid	Super capacitor	25–41%	[131]
Hitachi	20-ton excavator	Parallel hybrid	Super capacitor	25%	[120]
Kobelco	20-ton excavator	Parallel hybrid	Lithium battery	16%	[132]
Hitachi	18-ton wheel loader	Series hybrid	Super capacitor	31%	[115]
Rigitrac	91 kW tractor	Series hybrid	\	Unknown	[133]
John Deere	140 kW tractor	Series hybrid	\	Unknown	[134]
Huddig	116 kW backhoe loader	Series hybrid	\	Unknown	[135]

On the other hand, regarding more compact machinery, manufacturers are analyzing the hybridization of vehicles just above 56 kW mainly with the aim of avoiding advanced exhaust gas treatment systems; indeed, above this power limit, the European Stage V emission regulation [8] mandates the presence of an exhaust gas treatment system, which is not only an expensive component, it also requires a large amount of space, which is already very limited on compact vehicles.

Examples of this trend include the various projects on the hybridization of compact agricultural tractors [18,19,136,137], where the main objectives are the possibility of downsizing the ICE and addition a pure electric mode, which could be useful for less demanding tasks or for use inside greenhouses. However, even if there are some cases of hybrid compact vehicles below 56 kW, like the hybrid skid loader studied in [20,21], their higher efficiency does not justify their higher upfront cost.

A different but fascinating approach to the hybridization of compact tractors has been shown by Landini (Fabbrico, Italy) with its REX4 Electra [138]: instead of reducing the ICE, the main aim of the project was the improvement of productivity. Indeed, the electric motors are only mounted on the front axle, and they allow for two essential benefits: the first is the four-wheel drive mode with accurate slip control, the second is the use of the torque vectoring to enhance steering capability.

Finally, it is worth mentioning that machinery equipped with hydrogen ICEs or fuel cells are considered hybrid vehicles. Indeed, in both cases, the hydrogen is consumed to satisfy the average power demand, while energy storage systems are used to achieve peak loads and to recover energy.

Examples of hydrogen hybrid off-highway projects are the forklifts studied in [87,88], the excavators studied in [22,139] and the reach stacker and terminal tractor used in the experimental project explained in [140].

9. Conclusions

This paper gathers together all the main topics surrounding the electrification of off-highway vehicles, with a clear focus on compact vehicles and the technologies that best fit such machinery.

After a first, necessary classification of the off-highway vehicles, the main differences regarding drive cycles and duty cycles were highlighted, evidencing, with respect to the latter, the absence of standard and globally recognized cycles, mainly due to their high complexity and the extreme variability of their operating conditions and tasks. The types of electric vehicle architectures were presented along with the most important technologies related to energy storage systems and motors/generators. It was shown that lithium batteries are currently recognized as being the state of the art for the storage systems,

while the choice of the electric motor is highly dependent on the application, even if much attention has recently been given to switched reluctance motors. Then, the state of the art of electric vehicles and machinery was described, focusing on the construction category, and some common trends were found that can also be extended to other types of off-highway vehicles. After the overview regarding some of the more interesting electric solutions among the different off-highway categories, the current and future technologies related to hydraulics, actuators and energy recovery systems were investigated.

The different topics and the current state of the art were analyzed, giving rise to the following comments:

- In the off-highway machinery industry, the reduction of emission is not the only major driver for electrification. Indeed, the decrease of fuel consumption, the enhancement of productivity and, more generally, the clear convenience in terms of total cost of ownership are key points to successfully breaking into the market. Nonetheless, the political and technical choices of the authorities with respect to the environment and sustainability will be essential, with the presence of economic incentives and/or taxes being important variables to consider.
- The technical concept of mission and duty cycles has always been fundamental aspect of the off-highway industry, and these factors will be even more important for bringing effective, efficient and economically sustainable machinery to the market. Indeed, there are already work environments where battery or tethered electric vehicles represent the best technical and economical compromise, such as underground mining or indoor logistics. The continuous developments and the constant reduction in costs contributes to the introduction of new electric vehicles, even in highly complex work environments, like construction and agriculture.
- There are technical limits to a more widespread electrification within the off-highway machinery industry, and these mainly depend on power demands and minimum operational runtime. Less energy-demanding duty cycles in urban or indoor environments or high profitable businesses like vineyards facilitate the use of electric vehicles, especially in case of the compact ones. Conversely, bigger machinery with more intense duty cycles in more harsh environments is less suitable for battery electrification in the near future, mainly because the operational runtime achievable with the current technology cannot guarantee the minimum number of working hours, and the charging infrastructures are usually very difficult to implement in such contexts.
- Among the common trends, the most evident is the retrofitting of existing vehicles, where the electric motors and the battery pack replace the ICE and the fuel tank, with the rest of the machinery remaining almost unchanged (hydraulics, actuators, overall design, etc.). This strategy allows manufacturers to put functional vehicles on the market in the nearest future, but there is usually some distance to go before they are fully optimized. Indeed, there is generally great room for improvement, especially with respect to hydraulics.
- The application of new technologies regarding hydraulics, actuators and energy recovery systems can greatly boost the efficiency of off-highway vehicles, both electric and ICE-powered ones. On the other hand, the introduction of innovative technologies can greatly increase the upfront costs, frequently exceeding the acceptable cost-benefit ratio, as has already occurred in case of hybrid excavators.

In conclusion, compact vehicles can be an excellent application for boosting the electrification process, mainly because they are usually more suited for zero-emission tasks, while development costs can be more easily minimized. It is certain that, in the immediate future, the demand for zero-emission compact vehicles will increase due to the increasing focus on environmental sustainability; however, in order to design extremely efficient and effective products, manufacturers and researchers still need to devote a great deal of effort towards research and development, especially regarding the implementation of novel, better-connected hydraulics and with respect to the in-depth study of the energy flows during duty cycles. Furthermore, a more widespread development of the electrification

of compact vehicles could be useful for speeding up the development of highly tailored solutions, promptly responding to customers' demands. Indeed, the application of many different types of electric implements and accessories will be easier and faster compared to actual hydraulic systems, with the final goal of achieving modular and highly alterable machinery, capable of completing many types of duty cycles based on their equipment. Eventually, the widespread electrification of compact vehicles would allow for a more comprehensive understanding of the available technologies, reducing their costs and allowing their use on bigger and more energy-demanding machinery, with resulting benefits both in terms of productivity and environmental sustainability.

Author Contributions: Investigation, D.B. and S.U.; writing—original draft preparation D.B. and S.U.; data curation D.B.; supervision, S.U.; writing—review and editing P.I. and L.T. All authors have read and agreed to the published version of the manuscript.

Funding: This research received no external funding.

Institutional Review Board Statement: Not applicable.

Informed Consent Statement: Not applicable.

Data Availability Statement: The data presented in this study are available on request from the corresponding author. The data are not publicly available due to University of Brescia privacy policy.

Conflicts of Interest: The authors declare no conflict of interest.

Abbreviations

DC	Direct Current
EM	Electric Motor
EMA	Electro-Mechanical Actuator
ICE	Internal Combustion Engine
IM	Induction Motor
IMC	Individual Metering Control
NCA	Lithium Nickel Cobalt Aluminum Oxide
NEDC	New European Driving Cycle
NMC	Lithium Nickel Manganese Cobalt Oxide
OEM	Original Equipment Manufacturer
PMSM	Permanent Magnet Synchronous Motor
PTO	Power Take-Off
SOC	State of Charge
SRM	Switched Reluctance Motor
WLTP	World harmonized Light-duty vehicles Test Procedure

References

1. The European Commission. *The European Green Deal*; The European Commission: Brussels, Belgium, 2019; Volume 1.
2. Zawieska, J.; Pieriegud, J. Smart City as a Tool for Sustainable Mobility and Transport Decarbonisation. *Transp. Policy* **2018**, *63*, 39–50. [CrossRef]
3. IEA Global EV Outlook 2019. Available online: <https://www.iea.org/reports/global-ev-outlook-2019> (accessed on 21 January 2021).
4. The European Commission. *Comunicazione Della Commissione Al Parlamento Europeo, Al Consiglio Europeo, Al Consiglio, Al Comitato Economico e Sociale Europeo, Al Comitato Della Regioni e Alla Banca Europea per Gli Investimenti*; European Commission: Brussels, Belgium, 2018.
5. Lajunen, A.; Sainio, P.; Laurila, L.; Pippuri-Mäkeläinen, J.; Tammi, K. Overview of Powertrain Electrification and Future Scenarios for Non-Road Mobile Machinery. *Energies* **2018**, *11*, 1184. [CrossRef]
6. Dallman, T.; Menon, A. *Technology Pathways for Diesel Engines Used in Non-Road Vehicles and Equipment*; International Council on Clean Transportation (ICCT): Washington, DC, USA, 2016.
7. United States Environmental Protection Agency. Regulations for Emissions from Heavy Equipment with Compression-Ignition (Diesel) Engines, Regulations for Emissions from Vehicles and Engines. Available online: <https://www.epa.gov/regulations-emissions-vehicles-and-engines/regulations-emissions-heavy-equipment-compression#e-cfr> (accessed on 21 January 2021).
8. Emission Standards. Europe: Nonroad Engines. Available online: <https://dieselnet.com/standards/eu/nonroad.php> (accessed on 21 January 2021).

9. Caban, J.; Vrabel, J.; Šarkan, B.; Zarajczyk, J.; Marczuk, A. Analysis of the Market of Electric Tractors in Agricultural Production. *MATEC Web Conf.* **2018**, *244*, 1–10. [CrossRef]
10. Monnay, C. *Potential and Trends in Off-Highway Vehicle' Electrification*; Semcon: Gothenburg, Sweden, 2017.
11. Iora, P.G. *Tecnologie per La Mobilità Sostenibile: Veicoli Elettrici, Ibridi e a Fuel Cell*; Società Editrice Esculapio: Bologna, Italy, 2016; ISBN 978-88-7488-994-5.
12. Hegazy, O.; Barrero, R.; Van den Bossche, P.; El Baghdadi, M.; Smekens, J.; Van Mierlo, J.; Vriens, W.; Bogaerts, B. Modeling, Analysis and Feasibility Study of New Drivetrain Architectures for off-Highway Vehicles. *Energy* **2016**, *109*, 1056–1074. [CrossRef]
13. EPA. EPA Nonregulatory Nonroad Duty Cycles, MOVES and Other Mobile Source Emissions Models. Available online: <https://www.epa.gov/moves/epa-nonregulatory-nonroad-duty-cycles#individual> (accessed on 22 January 2021).
14. Meeting, A.; Report, K.N. *Experiences and Visions of an Implement Manufacturer*; Club of Bologna: Bologna, Italy, 2010.
15. Malavatu, J.; Kandke, S.R.; Gupta, S.; Agrawal, B. Design Challenges in Electrification of Off-Highway Applications. In Proceedings of the 2019 IEEE Transportation Electrification Conference (ITEC-India), Bengaluru, India, 17–19 December 2019. [CrossRef]
16. Mastrogiovanni, S. DLG-PowerMix. Available online: https://www.enama.it/userfiles/PaginaSezione/files/S._Mastrogiovanni_DLG.pdf (accessed on 3 March 2021).
17. Brenna, M.; Foiadelli, F.; Leone, C.; Longo, M.; Zaninelli, D. Feasibility Proposal for Heavy Duty Farm Tractor. In Proceedings of the 2018 International Conference of Electrical and Electronic Technologies for Automotive, Milan, Italy, 9–11 July 2018. [CrossRef]
18. Dalboni, M.; Santarelli, P.; Patroncini, P.; Soldati, A.; Concarì, C.; Lusignani, D. Electrification of a Compact Agricultural Tractor: A Successful Case Study. In Proceedings of the 2019 IEEE Transportation Electrification Conference and Expo (ITEC), Detroit, MI, USA, 19–21 June 2019. [CrossRef]
19. Troncon, D.; Alberti, L.; Mattetti, M. A Feasibility Study for Agriculture Tractors Electrification: Duty Cycles Simulation and Consumption Comparison. In Proceedings of the 2019 IEEE Transportation Electrification Conference and Expo (ITEC), Novi, MI, USA, 1 June 2019; IEEE: New York, NY, USA, 2019; pp. 1–6.
20. Bertini, A.; Ceraolo, M.; Lutzemberger, G. Systematic Approach in the Hybridization of a Hydraulic Skid Loader. *Autom. Constr.* **2015**, *58*, 144–154. [CrossRef]
21. Bertini, A.; Ceraolo, M.; Lutzemberger, G. Development of a Hybrid Skid Loader through Modelling. In Proceedings of the 2012 IEEE International Energy Conference and Exhibition (ENERGYCON), Florence, Italy, 9–12 September 2012; pp. 1022–1027. [CrossRef]
22. Alan, C.; Ali, S.; Alaa, H.; Eric, B. Optimal Sizing of an Energy Storage System for a Hybrid Vehicle Applied to an Off-Road Application. In Proceedings of the 2014 IEEE/ASME International Conference on Advanced Intelligent Mechatronics, Besancon, France, 8–11 July 2014; IEEE: New York, NY, USA; pp. 775–780.
23. Nevrlý, J.; Fichta, M.; Jurik, M.; Nemeč, Z.; Koutný, D.; Vorel, P.; Procházka, P. Battery Electric Drive of Excavator Designed with Support of Computer Modeling and Simulation. *Proceedings* **2020**, *58*, 25. [CrossRef]
24. Schneider, S.; Vincenz, D. *SUNCAR Elektrobagger*. Available online: <https://www.aramis.admin.ch/Default?DocumentID=46789&Load=true> (accessed on 3 September 2021).
25. Vauhkonen, N.; Liljeström, J.; Maharjan, D.; Mahat, C.; Sainio, P.; Kiviluoma, P.; Kuosmanen, P. Electrification of Excavator. In Proceedings of the 9th International DAAAM Baltic Conference “INDUSTRIAL ENGINEERING”, Tallinn, Estonia, 24–26 April 2014; pp. 305–310.
26. Salomaa, V.; Minav, T.; Mattila, J.; Pietola, M. Efficiency Study of an Electro-Hydraulic Excavator. Master's Thesis, Tampere University of Technology, Tampere, Finland, 2017.
27. Casoli, P.; Riccò, L.; Campanini, F.; Bedotti, A. Hydraulic Hybrid Excavator-Mathematical Model Validation and Energy Analysis. *Energies* **2016**, *9*, 1002. [CrossRef]
28. Construction Mechanization Association. *Earth-Moving Machinery—Test Methods for Energy Consumption—Hydraulic Excavators*; JCMAS: Tokyo, Japan, 2010.
29. Lin, T.; Lin, Y.; Ren, H.; Chen, H.; Chen, Q.; Li, Z. Development and Key Technologies of Pure Electric Construction Machinery. *Renew. Sustain. Energy Rev.* **2020**, *132*, 110080. [CrossRef]
30. Liebherr Liebherr Mining Goes Electric—Liebherr. Available online: <https://www.liebherr.com/en/ita/latest-news/news-press-releases/detail/liebherr-mining-goes-electric.html> (accessed on 5 March 2021).
31. Paraszczak, J.; Svedlund, E.; Fytas, K.; Laflamme, M. Electrification of Loaders and Trucks – A Step towards More Sustainable Underground Mining. *Renew. Energy Power Qual. J.* **2014**, *1*, 81–86. [CrossRef]
32. Połom, M. Trends in the Development of Trolleybus Transport in Poland at the End of the Second Decade of the 21st Century. *Pr. Kom. Geogr. Komun. PTG* **2018**, *21*, 44–59. [CrossRef]
33. Tribioli, L.; Chiappini, D.; Vukotić, M.; Miljavec, D. *Performance Evaluation of an Electric Vehicle with Multiple Electric Machines for Increased Overall Drive Train Efficiency*; SAE Technical Paper; SAE International: Warrendale, PA, USA, 2019. [CrossRef]
34. Sobotzik, J. *Electric Drives Potentials on Tractors and Implements*; John Deere: Moline, IL, USA, 2011.
35. Nishanth, F.N.U.; Khamitov, A.; Severson, E.L. Comparison of Linear and Rotary Electric Machine Topologies for a Hybrid Hydraulic Electric Architecture of Off-Highway Vehicles. In Proceedings of the 2020 IEEE Transportation Electrification Conference & Expo (ITEC), Chicago, IL, USA, 23–26 June 2020; pp. 1063–1068. [CrossRef]

36. Jo, D.Y.; Kwak, S.; Kim, N. Development of Fuel-Efficient Construction Equipment. In *“Green World with Power Electronics”, Proceedings of the 8th International Conference on Power Electronics—ECCE Asia, Jeju, Korea, 30 May–3 June 2011*; IEEE: New York, NY, USA, 2011; pp. 31–37.
37. Emadi, A. *Advanced Electric Drive Vehicles*, 1st ed.; CRC Press: Boca Raton, FL, USA, 2014.
38. Nykvist, B.; Nilsson, M. Rapidly Falling Costs of Battery Packs for Electric Vehicles. *Nat. Clim. Chang.* **2015**, *5*, 329–332. [[CrossRef](#)]
39. Ding, Y.; Cano, Z.P.; Yu, A.; Lu, J.; Zhongwei, C. Automotive Li-Ion Batteries: Current Status and Future Perspectives. *Electrochem. Energy Rev.* **2019**, *2*, 1–28. [[CrossRef](#)]
40. Yang, X.G.; Liu, T.; Wang, C.Y. Thermally Modulated Lithium Iron Phosphate Batteries for Mass-Market Electric Vehicles. *Nat. Energy* **2021**, *6*, 176–185. [[CrossRef](#)]
41. Wang, H.; Wang, Q.; Hu, B. A Review of Developments in Energy Storage Systems for Hybrid Excavators. *Autom. Constr.* **2017**, *80*, 1–10. [[CrossRef](#)]
42. Wang, J.; Yang, Z.; Liu, S.; Zhang, Q.; Han, Y. A Comprehensive Overview of Hybrid Construction Machinery. *Adv. Mech. Eng.* **2016**, *8*, 1–15. [[CrossRef](#)]
43. Hui, S.; Lifu, Y.; Junqing, J. Hydraulic/Electric Synergy System (HESS) Design for Heavy Hybrid Vehicles. *Energy* **2010**, *35*, 5328–5335. [[CrossRef](#)]
44. Casoli, D.-I.P.; Riccò, I.L.; Campanini, I.F.; Lettini, I.A.; Dolcin, I.C. Hydraulic Hybrid Excavator: Layout Definition, Experimental Activity, Mathematical Model Validation and Fuel Consumption Evaluation. In Proceedings of the 10th International Conference on Fluid Power (IFK), Dresden, Germany, 8–10 March 2016.
45. Lin, T.; Wang, L.; Huang, W.; Ren, H.; Fu, S.; Chen, Q. Performance Analysis of an Automatic Idle Speed Control System with a Hydraulic Accumulator for Pure Electric Construction Machinery. *Autom. Constr.* **2017**, *84*, 184–194. [[CrossRef](#)]
46. Rizzoni, G. *Fundamentals of Electrical Engineering by Giorgio Rizzoni*, 1st ed.; McGraw-Hill: New York, NY, USA, 2009; ISBN 978-0-07-338037-7.
47. Rajashekara, K. Present Status and Future Trends in Electric Vehicle Propulsion Technologies. *IEEE J. Emerg. Sel. Top. Power Electron.* **2013**, *1*, 3–10. [[CrossRef](#)]
48. Moreda, G.P.; Muñoz-García, M.A.; Barreiro, P. High Voltage Electrification of Tractor and Agricultural Machinery—A Review. *Energy Convers. Manag.* **2016**, *115*, 117–131. [[CrossRef](#)]
49. Mapelli, F.L. The Role of Motor Controllers in the Electrification Process. In Proceedings of the Industrial Vehicle Technology Virtual Expo, London, UK, 9–10 February 2021.
50. Un-Noor, F.; Padmanaban, S.; Mihet-Popa, L.; Nurunnabi Mollah, M.; Hossain, E.; Saponara, S. A Comprehensive Study of Key Electric Vehicle (EV) Components, Technologies, Challenges, Impacts, and Future Direction of Development. *Energies* **2017**, *10*, 1217. [[CrossRef](#)]
51. Yang, Z.; Shang, F.; Brown, I.P.; Krishnamurthy, M. Comparative Study of Interior Permanent Magnet, Induction, and Switched Reluctance Motor Drives for EV and HEV Applications. *IEEE Trans. Transp. Electrif.* **2015**, *1*, 245–254. [[CrossRef](#)]
52. Boldea, I.; Tutelea, L.N.; Parsa, L.; Dorrell, D. Automotive Electric Propulsion Systems with Reduced or No Permanent Magnets: An Overview. *IEEE Trans. Ind. Electron.* **2014**, *61*, 5696–5711. [[CrossRef](#)]
53. Riba, J.R.; López-Torres, C.; Romeral, L.; García, A. Rare-Earth-Free Propulsion Motors for Electric Vehicles: A Technology Review. *Renew. Sustain. Energy Rev.* **2016**, *57*, 367–379. [[CrossRef](#)]
54. Grayson, W. Bobcat’s Electric Excavator Retrofit a First Step Toward an All-Electric Future, Equipment World. Available online: <https://www.equipmentworld.com/alternative-power/battery-electric/video/14972534/bobcats-electric-excavator-retrofit-a-first-step-toward-an-allelectric-future> (accessed on 11 March 2021).
55. *Clean Air Action Plan*; Municipality of Amsterdam: Amsterdam, The Netherlands, 2019; pp. 1–93.
56. Volvo. Volvo CE and Volvo Trucks Customer Deliveries of All-Electric Products. Available online: <https://www.volvoce.com/global/en/news-and-events/press-releases/2020/volvo-ce-and-volvo-trucks-customer-deliveries-of-all-electric-products/> (accessed on 12 March 2021).
57. Wordsworth, S. Wacker Neuson and the Emissions-Free Worksite. Available online: <https://www.ivtinternational.com/videos/video-wacker-neuson-and-the-emissions-free-worksite.html> (accessed on 12 March 2021).
58. Big Buyers Zero-Emission Construction Sites. Available online: <https://bigbuyers.eu/working-groups/past/zero-emission-construction-sites> (accessed on 21 April 2021).
59. ISO. ISO—ISO 6469-3:2018—Electrically Propelled Road Vehicles—Safety Specifications—Part 3: Electrical Safety. Available online: <https://www.iso.org/standard/68667.html> (accessed on 12 March 2021).
60. Bilò, J.; Burghoff, H.-G.; dos Santos, H.; Engbring, J. *48 Volt Electrical Systems—A Key Technology Paving the Road to Electric Mobility*; Zwei: Frankfurt, Germany, 2016.
61. Fischer, H.-M.; Dorn, L. *Voltage Classes for Electric Mobility*; ZWEI: Frankfurt, Germany, 2013.
62. Jenkins, J. High-Voltage EV Battery Packs: Benefits and Challenges. More Voltage, More Better?—Charged EVs. Available online: <https://chargedevs.com/features/high-voltage-ev-battery-packs-benefits-and-challenges-more-voltage-more-better/> (accessed on 12 March 2021).
63. *Global Off-Highway Vehicle Electrification Trends, Forecast to 2030*; Frost and Sullivan: Santa Clara, CA, USA, 2019.
64. JCB. JCB 525-60E, Electric Telehandler. Available online: <https://www.jcb.com/en-gb/products/telescopic-handlers/525-60e-hiviz> (accessed on 16 April 2021).

65. Ueka, Y.; Yamashita, J.; Sato, K.; Doi, Y. Study on the Development of the Electric Tractor—Specifications and Traveling and Tilling Performance of a Prototype Electric Tractor. *Eng. Agric. Environ. Food* **2013**, *6*, 160–164. [CrossRef]
66. E-mining AG Products, E-Mining AG. Available online: <https://www.emining.ch/en/products> (accessed on 16 April 2021).
67. Friedrichschafen, Z.F. ZF ETRAC Driveline System for Electric Vehicles. Available online: <https://www.oemoffhighway.com/drivetrains/product/21126638/zf-friedrichshafen-ag-zf-etrac-driveline-system-for-electric-vehicles> (accessed on 11 March 2021).
68. *Electrification of Mobile Applications*; Boasch Rexroth AG: Lohr am Main, Germany, 2018.
69. *Market Positioning*; Deutz AG E-DEUTZ: Cologne, Germany, 2018.
70. Buning, E.A. Electric Drives in Agricultural Machinery—Approach from the Tractor Side. *J. Agric. Eng.* **2010**, *47*, 30.
71. CEMA. *European Agricultural Machinery Industry: CEMA Priorities and Key Figures*; CEMA: Brussels, Belgium, 2019; pp. 1–15.
72. Fendt. Fendt E100 Vario, Fendt FutureFarm—Fendt. Available online: <https://www.fendt.com/it/e100-vario> (accessed on 1 April 2021).
73. Rigitrac. Rigitrac SKE 40 Electric—Rigitracs Webseite! Available online: <https://www.rigitrac.ch/produkte-1/rigitrac-ske-40-electric/> (accessed on 1 April 2021).
74. Tractor, M. Monarch Tractor Electric Tractor. Available online: <https://www.monarchtractor.com/> (accessed on 1 April 2021).
75. Farmtrac Farmtrac—Trattori. Available online: <https://www.farmtracitalia.it/trattori> (accessed on 20 April 2021).
76. Van Leeuwen, L.B. Hydrogen or Battery Tractors: What Potential for Sustainable Grape Growing? *IVES Tech. Rev. Vine Wine* **2020**. [CrossRef]
77. Allen, J.; Deere, J. Develops Fully Electric, Autonomous Tractor, Industrial Vehicle Technology International. Available online: <https://www.ivtinternational.com/news/agriculture/john-deere-develops-fully-electric-autonomous-tractor.html> (accessed on 18 May 2021).
78. E-OX EOX—175. Available online: <https://www.e-ox.nl/eox-175> (accessed on 20 April 2021).
79. Pialorsi, R. Stato Dell’arte Dei Veicoli Elettrici e Studio Dell’elettrificazione Di Un Veicolo Industriale Con Trasmissione Meccanica. Master’s Thesis, Università degli Studi di Brescia, Brescia, Italy, 2019.
80. DULEVO Scopri La Nuova Spazzatrice Stradale Elettrica DZero2. Available online: <https://dzero2.dulevo.com/it/index.xhtml> (accessed on 2 April 2021).
81. Boschung Urban-Sweeper S2.0—Electric Street Sweeper Releasing 0 (Zero) Emissions. Available online: <https://www.boschung.com/product/urban-sweeper-s2-0/> (accessed on 2 April 2021).
82. Uberti, S.; Azzini, G.; Beltrami, D.; Tribioli, L.; Iora, P. *Modelling of a 15-KW Electric Utility Vehicle and Range Assessment through Driving Cycle Analysis Based on GPS Experimental Data*; SAE Technical Paper; SAE International: Warrendale, PA, USA, 2020. [CrossRef]
83. Esagono Energia Home—Esagono Energia, S.r.l.—Veicoli Elettrici. Available online: <https://www.esagonoenergia.com/> (accessed on 26 April 2021).
84. Morris, C. Charged EVs, Dennis Eagle’s New Electric Refuse Trucks Hit the Streets, Earn Rave Reviews—Charged EVs. Available online: <https://chargedevs.com/newswire/dennis-eagles-new-electric-refuse-trucks-hit-the-streets-earn-rave-reviews/> (accessed on 21 April 2021).
85. Sullivan, J. Gas Versus Electric Forklifts—Which Is Better? Available online: <https://www.tmhnc.com/blog/gas-versus-electric-forklifts-which-is-better> (accessed on 6 April 2021).
86. Fu, S.; Chen, H.; Ren, H.; Lin, T.; Miao, C.; Chen, Q. Potential Energy Recovery System for Electric Heavy Forklift Based on Double Hydraulic Motor-Generators. *Appl. Sci.* **2020**, *10*, 3996. [CrossRef]
87. Keränen, T.M.; Karimäki, H.; Viitakangas, J.; Vallet, J.; Ihonon, J.; Hyöttylä, P.; Uusalo, H.; Tingelöf, T. Development of Integrated Fuel Cell Hybrid Power Source for Electric Forklift. *J. Power Sources* **2011**, *196*, 9058–9068. [CrossRef]
88. Hosseinzadeh, E.; Rokni, M.; Advani, S.G.; Prasad, A.K. Performance Simulation and Analysis of a Fuel Cell/Battery Hybrid Forklift Truck. *Int. J. Hydrogen Energy* **2013**, *38*, 4241–4249. [CrossRef]
89. Yale, H. CLS Cls-Hyster.It—CLS S.p.A.—CGT Logistica Sistemi. Available online: <https://cls-hyster.it/> (accessed on 26 April 2021).
90. Simai Simai—Europe’s Widest Range of Electric Tow Tractors and Platform Trucks. Available online: <https://www.simai.it/en/home-2/> (accessed on 26 April 2021).
91. Sennebogen. SENNEBOGEN 817 E: Compact Material Handler for the Waste Industry—SENNEBOGEN Maschinenfabrik GmbH. Available online: <https://www.sennebogen.com/en/news/news-press/sennebogen-817-e-compact-material-handler-for-the-waste-industry> (accessed on 26 April 2021).
92. Electric Motor Engineering Partnership for the Industrial Full Electric Loader—Electric Motor Engineering. Available online: <https://www.electrictorengineering.com/partnership-for-the-industrial-full-electric-loader/> (accessed on 20 April 2021).
93. JCB 19C-1. JCB E-TECH, JCB.Com. Available online: <https://www.jcb.com/it-it/products/mini-escavatori/19c-1e> (accessed on 6 April 2021).
94. Tobroco Giant Electric Loaders from Tobroco—Giant Can Be Used All Year Long. Available online: <https://www.tobroco-giant.com/en/products/wheel-loaders/giant-g2200e-x-tra/> (accessed on 6 April 2021).
95. Volvo Prototype Electric Excavator. Available online: <https://www.volvoce.com/global/en/this-is-volvo-ce/what-we-believe-in/innovation/prototype-electric-excavator/> (accessed on 6 April 2021).
96. Zhang, S.; Minav, T.; Pietola, M. Decentralized Hydraulics for Micro Excavator. In Proceedings of the 15th Scandinavian International Conference on Fluid Power, SICFP, Linköping, Sweden, 7–9 June 2017; pp. 17187–17195. [CrossRef]

97. Zhang, S.; Minav, T.; Pietola, M.; Kauranne, H.; Kajaste, J. The Effects of Control Methods on Energy Efficiency and Position Tracking of an Electro-Hydraulic Excavator Equipped with Zonal Hydraulics. *Autom. Constr.* **2019**, *100*, 129–144. [CrossRef]
98. Arnulfo, S. JCB Dà Il Benvenuto Al 1° Escavatore 100% Elettrico: JCB 19C-1 E-TEC. Available online: <http://www.veicolidalavoro.it/jcb-escavatore-100-elettrico-jcb-19c-1-tec/> (accessed on 26 April 2021).
99. Tobroco Giant G2200E Series, Giant Loaders. Available online: <https://giantloaders.com/products/g2200e-series/> (accessed on 26 April 2021).
100. Volvo Construction Equipment. Volvo CE Unveils 100 Percent Electric Compact Excavator Prototype: Volvo Construction Equipment. Available online: <https://www.volvoce.com/global/en/news-and-events/press-releases/2017/volvo-ce-unveils-100-percent-electric-compact-excavator-prototype/> (accessed on 26 April 2021).
101. Volvo. Volvo CE Unveils the next Generation of Its Electric Load Carrier Concept: Volvo Construction Equipment. Available online: <https://www.volvoce.com/global/en/news-and-events/press-releases/2017/conexpo-vegas-2017/volvo-ce-unveils-the-next-generation-of-its-electric-load-carrier-concept/> (accessed on 21 April 2021).
102. Vukovic, M.; Leifeld, R.; Murrenhoff, H. Reducing Fuel Consumption in Hydraulic Excavators—A Comprehensive Analysis. *Energies* **2017**, *10*, 687. [CrossRef]
103. Minav, T.A.; Heikkinen, J.E.; Pietola, M. Direct Driven Hydraulic Drive for New Powertrain Topologies for Non-Road Mobile Machinery. *Electr. Power Syst. Res.* **2017**, *152*, 390–400. [CrossRef]
104. An, K.; Kang, H.; An, Y.; Park, J.; Lee, J. Methodology of Excavator System Energy Flow-Down. *Energies* **2020**, *13*, 951. [CrossRef]
105. Jensen, S. A Shifting Fluid Power Industry, OEM Off-Highway. Available online: <https://www.oemoffhighway.com/fluid-power/article/21244542/a-shifting-fluid-power-industry> (accessed on 17 February 2021).
106. Ge, L.; Quan, L.; Zhang, X.; Zhao, B.; Yang, J. Efficiency Improvement and Evaluation of Electric Hydraulic Excavator with Speed and Displacement Variable Pump. *Energy Convers. Manag.* **2017**, *150*, 62–71. [CrossRef]
107. Choi, K.; Seo, J.; Nam, Y.; Kim, K.U. Energy-Saving in Excavators with Application of Independent Metering Valve. *J. Mech. Sci. Technol.* **2015**, *29*, 387–395. [CrossRef]
108. Pellegri, M.; Green, M.; Macpherson, J.; McKay, C.; Caldwell, N. Applying a Multi-Service Digital Displacement[®] Pump to an Excavator to Reduce Valve Losses. In *Fluid Power Future Technology, Proceedings of the 12th International Fluid Power Conference, Dresden, Germany, 12–14 October 2020*; Technische Universität Dresden: Dresden, Germany, 2020; pp. 59–68. [CrossRef]
109. The European Commission. NorrDigi Revolutionary Energy Saver, Norrdigi Project, H2020, CORDIS, European Commission. Available online: <https://cordis.europa.eu/project/id/830085/it> (accessed on 25 March 2021).
110. Gehm, R. Volvo CE and Norrhydro Digital Hydraulics. Available online: <https://www.sae.org/news/2020/12/volvo-ce-and-norrhydro-digital-hydraulics> (accessed on 25 March 2021).
111. Qiao, G.; Liu, G.; Shi, Z.; Wang, Y.; Ma, S.; Lim, T.C. A Review of Electromechanical Actuators for More/All Electric Aircraft Systems. *J. Mech. Eng. Sci.* **2018**, *232*, 4128–4151. [CrossRef]
112. Lotz, T. Best Practices for Electrification of Mobile Machines. Available online: <https://www.oemoffhighway.com/trends/electrification/article/21342313/best-practices-for-electrification-of-mobile-machines> (accessed on 1 April 2021).
113. Wang, L.; Zhao, D.; Li, Y.; Du, M.; Chen, H. Energy Management Strategy Development of a Forklift with Electric Lifting Device. *Energy* **2017**, *128*, 435–446. [CrossRef]
114. He, X.; Xiao, G.; Hu, B.; Tan, L.; Tang, H.; He, S.; He, Z. The Applications of Energy Regeneration and Conversion Technologies Based on Hydraulic Transmission Systems: A Review. *Energy Convers. Manag.* **2020**, *205*, 112413. [CrossRef]
115. Ishida, K.; Higurashi, M. Hybrid Wheel Loaders Incorporating Power Electronics. *Hitachi Rev.* **2015**, *64*, 398–402.
116. Wirtgen Group. HD + 90i PH VO, Rulli Tandem, HAMM. Available online: <https://www.wirtgen-group.com/ocs/it-it/hamm/hd-90i-ph-vo-1878-p/> (accessed on 18 April 2021).
117. He, X.; Liu, H.; He, S.; Hu, B.; Xiao, G. Research on the Energy Efficiency of Energy Regeneration Systems for a Battery-Powered Hydrostatic Vehicle. *Energy* **2019**, *178*, 400–418. [CrossRef]
118. Yu, Y.-X.; Ahn, K.K. *Energy Saving and Control of a Hybrid Hydraulic Excavator Swing System*; IEEE: New York, NY, USA, 2020. [CrossRef]
119. Hitachi Construction Machinery ZH210-5 Hybrid—Hitachi Construction Machinery. Available online: <https://www.hitachim.com/it/prodotti/escavatori/escavatori-medi/zh210-5-hybrid/> (accessed on 18 April 2021).
120. Edamura, M.; Ishida, S.; Imura, S.; Izumi, S. Adoption of Electrification and Hybrid Drive for More Energy-Efficient Construction Machinery. *Hitachi Rev.* **2013**, *62*, 118–122.
121. Ge, L.; Dong, Z.; Quan, L.; Li, Y. Potential Energy Regeneration Method and Its Engineering Applications in Large-Scale Excavators. *Energy Convers. Manag.* **2019**, *195*, 1309–1318. [CrossRef]
122. Zhao, P.-Y.; Chen, Y.-L.; Zhou, H. Simulation Analysis of Potential Energy Recovery System of Hydraulic Hybrid Excavator. *Int. J. Precis. Eng. Manuf.* **2017**, *18*, 1575–1589. [CrossRef]
123. Lin, T.; Wang, Q.; Hu, B.; Gong, W. Research on the Energy Regeneration Systems for Hybrid Hydraulic Excavators. *Autom. Constr.* **2010**, *19*, 1016–1026. [CrossRef]
124. MMT Italia Hitachi ZH 210-5 Hybrid. Available online: https://www.mmtitalia.it/macchine_edili/marchi/hitachi/modelli/escavatori_cingolati/hitachi_zh_210-5_hybrid (accessed on 26 April 2021).
125. Konecranes Reach Stackers, Konecranes. Available online: <https://www.konecranes.com/equipment/lift-trucks/reach-stackers> (accessed on 26 April 2021).

126. Lajunen, A.; Suomela, J.; Pippuri, J.; Tammi, K.; Lehmuspelto, T.; Sainio, P. Electric and Hybrid Electric Non-Road Mobile Machinery—Present Situation and Future Trends. *World Electr. Veh. J.* **2016**, *8*, 172–183. [CrossRef]
127. He, X.; Jiang, Y. Review of Hybrid Electric Systems for Construction Machinery. *Autom. Constr.* **2018**, *92*, 286–296. [CrossRef]
128. Soma, A.; Bruzzese, F.; Mocera, F.; Viglietti, E. Hybridization Factor and Performance of Hybrid Electric Telehandler Vehicle. *IEEE Trans. Ind. Appl.* **2016**, *52*, 5130–5138. [CrossRef]
129. Truong, D.Q.; Marco, J.; Greenwood, D.; Harper, L.; Corrochano, D.G.; Yoon, J.I. Challenges of Micro/Mild Hybridisation for Construction Machinery and Applicability in UK. *Renew. Sustain. Energy Rev.* **2018**, *91*, 301–320. [CrossRef]
130. Huria, T.; Lutzemberger, G.; Sanna, G.; Pede, G. Systematic Development of Series-Hybrid Bus through Modelling. In Proceedings of the 2010 IEEE Vehicle Power and Propulsion Conference, Lille, France, 1–3 September 2010. [CrossRef]
131. Inoue, H. Introduction of PC200-8 Hybrid Hydraulic Excavators. *Komatsu Tech. Rep.* **2008**, *54*, 1–6.
132. Kobelco Europe. HYBRID—Kobelco Construction Machinery Europe B.V. Available online: <https://www.kobelco-europe.com/innovation/hybrid/> (accessed on 8 April 2021).
133. TU Dresden Rigitrac EWD 120. Available online: https://tu-dresden.de/ing/maschinenwesen/int/ast/ressourcen/dateien/forschung/files/flyer_rigitrac.pdf?lang=en (accessed on 8 April 2021).
134. Stoss, K.J.; Sobotzik, J.; Shi, B.; Kreis, E.R. Tractor Power for Implement Operation—Mechanical, Hydraulic, and Electrical: An Overview. *Agric. Equip. Technol. Conf.* **2013**, 1–25.
135. Huddig Tigon Huddig World’s Best Backhoe Loaders Made in Sweden. Available online: <https://www.huddig.com/products/machines/tigon/> (accessed on 8 April 2021).
136. Troncon, D.; Alberti, L.; Bolognani, S.; Bettella, F.; Gatto, A. Electrification of Agricultural Machinery: A Feasibility Evaluation. In Proceedings of the 2019 Fourteenth International Conference on Ecological Vehicles and Renewable Energies (EVER), Monte Carlo, Monaco, 8–10 May 2019; IEEE: New York, NY, USA; pp. 1–7.
137. Troncon, D.; Alberti, L. Case of Study of the Electrification of a Tractor: Electric Motor Performance Requirements and Design. *Energies* **2020**, *13*, 2197. [CrossRef]
138. Landini Landini REX4 Electra—Evolving Hybrid—Landini. Available online: <https://www.landini.it/en/landini-rex4-electra-evolving-hybrid/> (accessed on 20 April 2021).
139. Li, T.; Huang, L.; Liu, H. Energy Management and Economic Analysis for a Fuel Cell Supercapacitor Excavator. *Energy* **2019**, *172*, 840–851. [CrossRef]
140. H2ports First Application of Hydrogen Technologies in Port Handling Equipment in Europe. Available online: <https://h2ports.eu/wp-content/uploads/2020/03/H2PORTS-Brochure.pdf> (accessed on 26 August 2021).

MDPI
St. Alban-Anlage 66
4052 Basel
Switzerland
Tel. +41 61 683 77 34
Fax +41 61 302 89 18
www.mdpi.com

Energies Editorial Office
E-mail: energies@mdpi.com
www.mdpi.com/journal/energies



MDPI
St. Alban-Anlage 66
4052 Basel
Switzerland

Tel: +41 61 683 77 34
Fax: +41 61 302 89 18

www.mdpi.com



ISBN 978-3-0365-4126-6